

Fabrication and Pre-irradiation Characterization of a Minor Actinide and Rare Earth Containing Fast Reactor Fuel Experiment for Irradiation in the Advanced Test Reactor

Timothy A. Hyde

June 2012



The INL is a U.S. Department of Energy National Laboratory
operated by Battelle Energy Alliance

Fabrication and Pre-irradiation Characterization of a Minor Actinide and Rare Earth Containing Fast Reactor Fuel Experiment for Irradiation in the Advanced Test Reactor

Timothy A. Hyde

June 2012

**Idaho National Laboratory
Idaho Falls, Idaho 83415**

<http://www.inl.gov>

**Prepared for the
U.S. Department of Energy
Office of Nuclear Energy
Under DOE Idaho Operations Office
Contract DE-AC07-05ID14517**

Fabrication and Pre-irradiation Characterization of a Minor Actinide and Rare Earth Containing Fast Reactor Fuel Experiment for Irradiation in the Advanced Test Reactor

A Thesis

Presented in partial fulfillment of the requirements for the

degree of Master of Science

with a

major in Mechanical Engineering

in the

College of Graduate Studies

University of Idaho

by

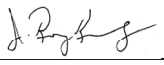
Timothy A. Hyde

June 2012

Major Professor: John Crepeau, Ph.D.

AUTHORIZATION TO SUBMIT THESIS

This thesis of Timothy A. Hyde, submitted for the degree of Master of Science with a major in Mechanical Engineering and titled “Fabrication and Pre-irradiation Characterization of a Minor Actinide and Rare Earth Containing Fast Reactor Fuel Experiment for Irradiation in the Advanced Test Reactor,” has been reviewed in final form. Permission, as indicated by the signatures and dates given below, is now granted to submit final copies to the College of Graduate Studies for approval.

Major Professor	_____	Date _____
	John Crepeau	
Committee Member	_____	Date _____
	 J. Rory Kennedy	
Committee Member	_____	Date _____
	Steven L. Hayes	
Mechanical Engineering Department Chair	_____	Date _____
	John Crepeau	
Dean of the College of Engineering	_____	Date _____
	Larry Stauffer	

Final Approval and Acceptance by the College of Graduate Studies

_____	Date _____
Jie Chen	

ABSTRACT

The United States Department of Energy seeks to develop and demonstrate the technologies needed to transmute the long-lived transuranic actinide isotopes contained in spent nuclear fuel into shorter-lived fission products, thereby decreasing the volume of material requiring disposal and reducing the long-term radiotoxicity and heat load of high-level waste sent to a geologic repository. This transmutation of the long-lived actinides plutonium, neptunium, americium and curium can be accomplished by first separating them from spent Light Water Reactor fuel using a pyrometallurgical process, then reprocessing them into new fuel with fresh uranium additions, and then transmuted to short-lived nuclides in a liquid metal-cooled fast reactor. An important component of the technology is developing actinide-bearing fuel forms containing plutonium, neptunium, americium and curium isotopes and rare earth process residual that meet the stringent requirements of reactor fuels and materials.

The fabrication rigor and documentation for such experiments is an important aspect of irradiation testing. As such, this thesis has significant focus on the fabrication rigor and initial characterization of the experiment(s) AFC-2A and AFC-2B. This is also a strong emphasis of this thesis because I was directly responsible for overseeing all aspects of the fabrication process. The thesis goes on to document the phase transitions and thermo physical properties of the specific multi element fuel alloys used in the experiment. In conclusion, the data suggest that the complex alloys investigated behave very much like the base 3 component U-Pu-Zr system, despite having up to 6 additional elements. It is also concluded that a new casting process needs to be developed to improve repeatability and potentially reduce mold interaction. Experience obtained during the actual irradiation of the AFC-2A experiment indicates that redesign of some components is needed to improve fabricability and reduce the risk of not meeting the desired experimental conditions.

ACKNOWLEDGEMENTS

I would specifically like to acknowledge the technical contributions of the following people:
Paul Hansen, Randall Fielding, Bryan Forsmann, Cynthia Papesch, Doug Burkes, Rory Kennedy,
Dawn Janney, and Andrew Maddison.

TABLE OF CONTENTS

AUTHORIZATION TO SUBMIT THESIS.....	ii
ABSTRACT.....	iii
ACKNOWLEDGEMENTS.....	iv
TABLE OF CONTENTS.....	v
FIGURES.....	vi
TABLES	xi
1. INTRODUCTION	1
2. FABRICATION AND EXPERIMENTAL RESULTS	9
2.1 Fuel Slug Fabrication	9
2.2 Cladding Fabrication.....	31
2.3 Rodlet Loading and Sealing	32
2.4 Capsule Fabrication.....	37
2.5 Capsule Assembly	39
3. TMA EXPERIMENTAL RESULTS	45
4. DISCUSSION.....	53
4.1 Scanning Electron Microscopy	53
4.2 Differential Scanning Calorimetry	81
4.3 Phase Discussion.....	83
4.4 Thermal Conductivity Discussion.....	89
4.4.1 Laser Flash Diffusivity	89
4.4.2 Specific Heat Capacity	92
4.4.3 Density.....	92
4.4.4 Thermal Conductivity Calculation.....	93
5. CONCLUSION	95
5.1 Casting Improvements	96
5.2 Experiment Design Improvements.....	100
6. REFERENCES	101

FIGURES

Figure 1. AFC-2 series irradiation test assembly for ATR east flux trap positions.	5
Figure 2. Radial dimensions of capsule and fuel rodlet assemblies for the AFC-2 metallic fuel tests.	6
Figure 3. Rodlet assembly axial dimensions for the AFC-2 metallic fuel tests.	7
Figure 4. AFC-2 fuel, rodlet, and capsule fabrication.	10
Figure 5. Fuel feedstock pieces in weighing pan.	11
Figure 6. Alloy button on copper hearth.	11
Figure 7. Arc melting furnace ready for suction casting.	12
Figure 8. Suction cast fuel after cooling.	13
Figure 9. Resistance-heated furnace elements.	14
Figure 10. New drop-casting hearth(s).	15
Figure 11. Drop casting hearth after several castings.	16
Figure 12. Inverted hearth(s) showing fuel inside quartz mold.	16
Figure 13. Drop-cast fuel slug.	17
Figure 14. Sectioning samples using the Buehler Saw.	18
Figure 15. 60U-20Pu-3Am-2Np-15Zr (A1) fuel slugs and characterization samples.	19
Figure 16. 59U-20Pu-3Am-2Np-15Zr (A2) fuel slugs and characterization samples.	20
Figure 17. 58.5U-20Pu-3Am-2Np-1.5RE-15Zr (A3) fuel slugs and characterization samples.	21
Figure 18. 40.5U-30Pu-5Am-3Np-1.5RE-20Zr (A4) fuel slugs.	22
Figure 19. 41U-30Pu-5Am-3Np-1RE-20Zr (A5) fuel slugs and samples.	23
Figure 20. 42U-30Pu-5Am-3Np-20Zr (A6) fuel slugs and characterization samples.	24
Figure 21. Uranium composition of cast fuel compared to target compositions.	26
Figure 22. Plutonium composition of cast fuel compared to target compositions.	26
Figure 23. Zirconium composition of cast fuel compared to target compositions.	27
Figure 24. Americium composition of cast fuel compared to target compositions.	27
Figure 25. Neptunium composition of cast fuel compared to target compositions.	28
Figure 26. Cerium composition of cast fuel compared to target compositions.	28
Figure 27. Lanthanum composition of cast fuel compared to target compositions.	29
Figure 28. Neodymium composition of cast fuel compared to target compositions.	29
Figure 29. Praseodymium composition of cast fuel compared to target compositions.	30
Figure 30. AFC-2 rodlet weld micrograph.	31
Figure 31. Rodlet components.	32

Figure 32. Rodlet closure weld radiograph.....	33
Figure 33. Loading rodlets into the settling and bonding furnace for heating.	34
Figure 34. Settling and bonding furnace with four rodlets in place.....	35
Figure 35. Copper chill block for cooling rodlets.....	36
Figure 36. Rodlet radiograph showing fuel and sodium levels.....	37
Figure 37. Capsule end plug radiograph.....	38
Figure 38. Etched capsules with spacer and end caps.....	40
Figure 39. Verifying rodlet serial numbers and loading order.....	41
Figure 40. Rodlets and spacers laid out for loading into capsule. (The rod to the far left is a push rod for loading rodlets.).....	42
Figure 41. Inserting rodlet into capsule.	43
Figure 42. Orbital welding system for capsule closure inside a He glove bag with a test tube shown in place.	43
Figure 43. Inserting a loaded capsule into the orbital welding enclosure.....	44
Figure 44. Capsule radiograph verifying rodlet position.	44
Figure 45. Pt Standard heating and cooling curves.....	45
Figure 46. Open TMA showing sample.....	46
Figure 47. Tim Hyde working with the TMA in the glovebox.....	47
Figure 48. 60U-20Pu-3Am-2Np-15Zr (A1) TMA heating and cooling curves.....	48
Figure 49. 59U-20Pu-3Am-2Np-1RE-15Zr (A2) TMA heating and cooling curves.	48
Figure 50. 58.5U-20Pu-3Am-2Np-1.5RE-15Zr (A3) TMA heating and cooling curves.	49
Figure 51. 40.5U-30Pu-5Am-3Np-1.5RE-20Zr (A4) TMA heating and cooling curves.	50
Figure 52. 41U-30Pu-5Am-3Np-1RE-20Zr (A5) TMA heating and cooling curves.	51
Figure 53. 42U-30Pu-5Am-3Np-20Zr (A6) TMA heating and cooling curves.....	52
Figure 54. “A” series thermal expansion.	53
Figure 55. Low-magnification images of the 60U-20Pu-3Am-2Np-15Zr (A1) casting samples, AFC2-A1-79-SEM1 (top) and AFC2-A1-80-2-SEM1 (bottom).	54
Figure 56. Secondary electron image of the 60U-20Pu-3Am-2Np-15Zr (A1) sample AFC2-A1-79-SEM1. Large dark areas in center and at left are internal porosity. Smaller dark areas are inclusions.	55
Figure 57. Higher magnification BSE image of the 60U-20Pu-3Am-2Np-15Zr (A1) sample AFC2-A1-79-SEM1.	55
Figure 58. Secondary electron (SE) images of the 60U-20Pu-3Am-2Np-15Zr (A1) samples, AFC2-A1-79-SEM1 (top) and AFC2-A1-80-2-SEM1 (bottom).	56
Figure 59. X-ray maps of the 60U-20Pu-3Am-2Np-15Zr (A1) sample, AFC2-60U-20Pu- 3Am-2Np-15Zr (A1)-80-2-SEM1.	57

Figure 60. Low-magnification image showing the entire 59U-20Pu-3Am-2Np-1RE-15Zr (A2) sample. Al indicates aluminum tape.	58
Figure 61. BSE and SE compiled images show microstructure of 59U-20Pu-3Am-2Np-1RE-15Zr (A2) sample from center to edge. Scale bars are 200 μ m.	59
Figure 62. SE, BSE and WDX x-ray maps from the interior of the 59U-20Pu-3Am-2Np-1RE-15Zr (A2) sample.	61
Figure 63. Higher-magnification images of internal area of the 59U-20Pu-3Am-2Np-1RE-15Zr (A2) fuel sample: on left, larger SE image; on right, WDX x-ray maps using the Zr L α , Nd L α , and Am M β x-rays.	62
Figure 64. X-ray maps from the rim region. EDX maps used the Zr K α , La L α , U L α , Np L α , Pu L α , and Am L α x-rays. WDX maps used Nd L α and Am M β x-rays.	63
Figure 65. Micrograph images of the rim region: (a) SE image (b) high-contrast BSE image (c) low-contrast BSE image (d) SE image (e) high-contrast BSE image (f) low-contrast BSE image.	64
Figure 66. Low magnification images of the 58.5U-20Pu-3Am-2Np-1.5RE-15Zr (A3) casting sample AFC2-A3-83-1-SEM1.	65
Figure 67. Secondary electron (SE) image of the 58.5U-20Pu-3Am-2Np-1.5RE-15Zr (A3) sample, AFC2-A3-83-1-SEM1.	66
Figure 68. Backscattered electron image (BSE) of the 58.5U-20Pu-3Am-2Np-1.5RE-15Zr (A3) sample, (AFC2-A3-83-1-SEM1).	66
Figure 69. Secondary electron image of the 58.5U-20Pu-3Am-2Np-1.5RE-15Zr (A3) sample, (AFC2-A3-83-1-SEM1).	67
Figure 70. X-ray maps of the center of the 58.5U-20Pu-3Am-2Np-1.5RE-15Zr (A3) casting sample, AFC2-A3-83-1-SEM1.	68
Figure 71. X-ray maps of the edge region of the 58.5U-20Pu-3Am-2Np-1.5RE-15Zr (A3) sample, (AFC2-A3-83-1-SEM1).	69
Figure 72. Scanned thermal prints showing low-magnification: (a) SE and (b) BSE images of an 40.5U-30Pu-5Am-3Np-1.5RE-20Zr (A4) sample. Scale bars: 1 mm.	70
Figure 73. Overlapping SE (top row) and BSE images (bottom row) traversing 40.5U-30Pu-5Am-3Np-1.5RE-20Zr (A4) sample.	71
Figure 74. WDX x-ray maps (collected at 20 kV). Scale bar: 20 microns.	72
Figure 75. Images from an area about 1/3 of the way from the edge of the 40.5U-30Pu-5Am-3Np-1.5RE-20Zr (A4) sample to the center: (a) SE. (b) BSE, low contrast. (c) BSE image, higher contrast. Scale bars: 20 microns.	72
Figure 76. WDX x-ray maps (collected at 20 kV) from the area shown in Figure 75. Scale bar: 20 microns.	73
Figure 77. SE image (left) and BSE image (right) of the edge or rim area of the fuel sample. Scale bars: 20 microns.	74
Figure 78. WDX x-ray maps (collected at 20 kV) from the area shown in Figure 77. Scale bar: 20 microns.	74

Figure 79. Scanned thermal print showing low-magnification SE image of the 41U-30Pu-5Am-3Np-1RE-20Zr (A5) sample. Scale bar: 1 mm.....	76
Figure 80. Sample 41U-30Pu-5Am-3Np-1RE-20Zr (A5) images. (a) SE image (b) higher magnification SE images of the central area of 'a.' Scale bar: 20 microns. (c) higher magnification SE image overlapping the left center of 'a.' Scale bar: 20 microns. (d – f) low contrast BSE images corresponding to 'a – c.'	76
Figure 81. WDX x-ray maps (collected at 20 kV) from approximately the area shown in Figure 80f. Scale bar: 20 microns.....	77
Figure 82. Low-magnification view of the 42U-30Pu-5Am-3Np-20Zr (A6) sample (AFC2-A6-82-5-SEM1).	78
Figure 83. Secondary electron (SE) image of the 42U-30Pu-5Am-3Np-20Zr (A6) sample (AFC2-A6-82-5-SEM1). Large dark areas in center and at left are internal porosity. Smaller dark areas are inclusions.	79
Figure 84. Backscattered electron (BSE) image of the 42U-30Pu-5Am-3Np-20Zr (A6) sample (AFC2-A6-82-5-SEM1).	80
Figure 85. X-ray maps of sample 42U-30Pu-5Am-3Np-20Zr (A6) showing unusual silicon carbide inclusion and more typical zirconium-rich, actinide-poor inclusions.	81
Figure 86. Heating and cooling traces obtained from the DSC/DTA measurements on the as-cast alloy 60U-20Pu-3Am-2Np-15Zr (A1).	82
Figure 87. Experimental phase diagram of the U-Pu-Zr system (O'Boyle and Dwight 1970) at 500°C with the positions of the 60U-20Pu-3Am-2Np-15Zr (A1) and 42U-30Pu-5Am-3Np-20Zr (A6) compositions marked.	84
Figure 88. Ternary U-Pu-Zr phase diagrams taken at isothermal sections with reduced composition (in terms of U-Pu-Zr), for alloys 60U-20Pu-3Am-2Np-15Zr (A1) and 42U-30Pu-5Am-3Np-20Zr (A6).	86
Figure 89. A room temperature U-Pu-Zr ternary phase diagram estimated from isothermal sections and the three binary phase diagrams of the elements involved (Kennedy et al. August 2003).	87
Figure 90. Thermal diffusivity plot for 60U-20Pu-3Am-2Np-15Zr (A1) alloy with correlated fits from Equations 1 and 2.....	91
Figure 91. Thermal diffusivity plot for all alloys.....	91
Figure 92. Specific heat capacity plot for all alloys.....	92
Figure 93. Thermal conductivity curves for all alloys.	95
Figure 94. Centrifugal caster.....	96
Figure 95. Single large diameter casting in quartz mold.	97
Figure 96. Multiple AFC-2 representative diameter casting of titanium.	97
Figure 97. Stand-alone vacuum casting system.	98
Figure 98. Section view of the two-chamber casting concept.	99

TABLES

Table 1. Overview of the AFC-2A and AFC-2B experiments.....	2
Table 2. Nominal fuel rodlet compositions and letter codes.....	3
Table 3. Design data for capsule assembly.....	6
Table 4. Fuel rodlet design data.....	7
Table 5. AFC-2A and AFC-2B experiment specifications.....	8
Table 6. General characterization samples needed.....	18
Table 7. AFC-2 fuel physical properties.....	25
Table 8. Capsule AFC-2A.....	39
Table 9. Capsule AFC-2B.....	40
Table 10. Transition temperature peaks for the all alloys.....	83
Table 11. Onset of experimental phase transitions determined upon cooling the samples and predicted phase transitions based on the U-Pu-Zr ternary diagrams (O'Boyle and Dwight 1970) for each metal alloy.....	88
Table 12. Thermal diffusivity values at temperature determined for the 60U-20Pu-3Am- 2Np-15Zr (A1) alloy.....	90
Table 13. Density as a function of temperature for all alloys.....	93
Table 14. 60U-20Pu-3Am-2Np-15Zr (A1) alloy properties as a function of temperature.....	93
Table 15. 59U-20Pu-3Am-2Np-1RE-15Zr (A2) alloy properties as a function of temperature.....	94
Table 16. 58.5U-20Pu-3Am-2Np-1.5RE-15Zr (A3) alloy properties as a function of temperature.....	94
Table 17. 40.5U-30Pu-5Am-3Np-1.5RE-20Zr (A4) alloy properties as a function of temperature.....	94
Table 18. 41U-30Pu-5Am-3Np-1RE-20Zr (A5) alloy properties as a function of temperature.....	94
Table 19. 42U-30Pu-5Am-3Np-20Zr (A6) alloy properties as a function of temperature.....	95

1. INTRODUCTION

An extensive literature review was performed to find all similar work. The open literature discusses the microstructure or properties of similar complex alloys. No publications discussed how fueled experiments are fabricated and inspected. Some literature discusses U-Pu-Zr alloy properties, which is helpful because it is the base alloy for this experiment and study and these references were used throughout the text. There are numerous publications on how metallic fuels and metallic fuels with minor actinides can potentially be used as fast reactor fuel and how these fuels in the fast reactors can close the fuel cycle. These articles are best referenced here because they do not greatly influence the evaluation of observed AFC-2 data, but show the driving force behind trying to increase the knowledge associated with these complex fuels (Hecker and Stan 2007; Keiser and Pertri 1996; Ogawa 2002; Walters 1999; Harbur, Anderson, and Maraman 1970; Pahl et al. 1992; Lahm et al. 1994; Broeders, Kiefhaber, and Wiese 2000). Some literature discusses how U-Pu-Zr alloys redistribute under thermal gradients and under irradiation. The relevant references are documented at the end of this document and throughout the text, where appropriate.

The United States Department of Energy (DOE) seeks to develop and demonstrate technologies needed to transmute the long-lived transuranic actinide isotopes contained in spent nuclear fuel into shorter lived fission products, thereby decreasing the volume of material requiring disposal and reducing the long-term radiotoxicity and heat load of high-level waste that goes to a geologic repository (Advanced Fuel Cycle Initiative, Report to Congress 2003). Transmutation of the long-lived actinides plutonium (Pu), neptunium (Np), americium (Am) and curium (Cm) can be accomplished by first separating them from spent Light Water Reactor (LWR) fuel using a pyrometallurgical process (Inoue 2002). The actinides are reprocessed into new fuel with fresh uranium additions, and then transmuted to short-lived nuclides in a liquid metal-cooled fast reactor (Inoue 2002; Ogawa 2002; Walters 1999; Hofman, Walters, and Bauer 1997). An important component of the technology is developing actinide-bearing fuel forms containing plutonium, neptunium, americium and curium isotopes that meet the stringent requirements of reactor fuels and materials (Kim et al. 2004; Kim et al. 2006; Kim et al. 2004). These fuels will also possibly contain rare earth elements, which are the metallic fuels expected fission product carry-over elements from subsequent pyrometallurgical reprocessing of LWR fuels.

The AFC-2A and AFC-2B irradiation experiments continue the metallic fuel test series in progress in the Advanced Test Reactor (ATR). Initial scoping level irradiation tests of such metallic fuels have already been performed in the ATR (AFC-1B, D, F, and H). Nonfertile (the fuel contains only a small amount of isotopes that can absorb a neutron, and then become fissile) and low-fertile (the fuel contains no isotopes that can absorb a neutron, and then become fissile) metallic fuels in the tests have already been discharged from the reactor at 8% burnup and are nearing the completion of postirradiation examination; performance of all the fuel alloys included in these tests was good (Hilton, Porter, and Hayes 2005). Similar fuel alloys continue to be irradiated and are currently over 20% burnup. The AFC-2A and 2B experiments were irradiated in two of the east flux trap positions of the ATR using the same hardware previously used (Hayes 2003; Hilton 2003; Hilton 2003).

The AFC-2A and 2B irradiation experiments are expected to provide important irradiation performance data on metallic transmutation fuel forms including: irradiation growth and swelling, helium production, helium and fission gas release fractions, fission product and fuel constituent migration, fuel phase equilibria, and fuel-cladding chemical interaction. Of particular interest in these tests will be the effect that small additions of rare earth elements have on irradiation performance parameters.

Experiments AFC-2A and 2B have design and test conditions analogous to previous metallic fuel tests. Table 1 shows test matrix in AFC-2A and 2B were identical; only the target discharge burnups will differ for the two tests. Table 1 shows an overview of these two experiments. The simultaneous insertion of these two irradiation test assemblies started in August, 2007 (ATR Cycle 140A).

Table 1. Overview of the AFC-2A and AFC-2B experiments.

ATR Experiment Designation	Fuel Form	ATR Insertion	Target Discharge Burnup*
AFC-2A	Metallic	Aug 2007	$\geq 10\%$
AFC-2B	Metallic	Aug 2007	$\geq 25\%$

*Burnup in percent of initial (Pu-239 + U-235).

U-Pu-Zr-based metallic fuel is one of two primary candidates being investigated by the DOE as possible transmutation fast reactor fuel (the other is oxide). Within the research community, there is considerable experience with both how to manufacture this fuel and how it performs in

fast reactors. Most of this experience in the US exists as a result of DOE work performed by Argonne National Laboratory, primarily in Idaho at a facility now known as the Materials and Fuels Complex (MFC) and operated under the Idaho National Laboratory (INL). Though researchers have considerable experience with the base U-Pu-Zr system, the addition of the minor actinides (MA) Np, Am, and Cm and the complication of rare earths create a good research opportunity. Information available on the effects of these additions on the microstructure and physical properties of the resulting alloys or mixtures is limited. The radiological nature of Cm dictates that it be handled only in remote-handling hot cell facilities, so little to no research has been undertaken on its effects. It was ruled out for the alloys considered here. The Japanese did research on the effects of all additions except Cm in the early to mid 90's (Kurata, Inoue, Sari 1994). Plenty remains to be learned on the effects of these alloy additions.

Compared to the fuel compositions in the previous tests, the AFC-2A, B uranium contents have been increased and the zirconium contents have been decreased as the DOE program objectives have evolved to where a somewhat higher conversion ratio is deemed as acceptable in future sodium-cooled fast reactors used for actinide transmutation. The lower Zr content results in a denser fuel, though still considerably less dense than the U-20Pu-10Zr fuels irradiated routinely in EBR-II.

Table 2 shows the target compositions for the fuel. Fuel chemical and isotopic compositions vary over a wide range in this experiment. Factors that inform chemical and isotopic composition are the in-reactor fission heat generation rate, the fuel solidus temperature, and the gas production by Am-241. As such, the U-235 enrichments have been determined for each alloy.

Table 2. Nominal fuel rodlet compositions and letter codes.

Designator	Metallic Fuel Alloy†	Uranium-235 Enrichments
AFC2-A1	60U-20Pu-3Am-2Np-15Zr	93% U-235
AFC2-A2	59U-20Pu-3Am-2Np-1.0RE*-15Zr	55% U-235
AFC2-A3	58.5U-20Pu-3Am-2Np-1.5RE*-15Zr	45% U-235
AFC2-A4	40.5U-30Pu-5Am-3Np-1.5RE*-20Zr	55% U-235
AFC2-A5	41U-30Pu-5Am-3Np-1.0RE*-20Zr	65% U-235
AFC2-A6	42U-30Pu-5Am-3Np-20Zr	93% U-235

†Alloy composition expressed in weight percent.

*RE = rare earth alloy (6% La, 16% Pr, 25% Ce, 53% Nd).

The primary component for each experiment, which contains the fuel specimen, is termed a “rodlet.” Rodlets are miniature fuel rods six in. long. Externally, each of the rodlets in both experiments was identical. The “Irradiation of Metallic Fuels with Rare Earth Additions for Actinide Transmutation in the ATR; Experiment Description for AFC-2A and AFC-2B,” INL/EXT-06-11707, Rev. 2, (Hayes 2006) provides further details on experiment configuration and performance. Reactor insertion experiments have strictly defined and controlled requirements and specifications. These specifications are laid out in a document signed by both representatives of the reactor and from the experimental program. The document for the AFC-2 experiment is “AFC-2A and 2B Fuel Specification” (Hyde 2007). This document provides details on fuel isotopic limits and details of the metallic fuel rodlet construction. The full experiment is also described in “Project Description, Advanced Fuel Cycle Initiative, AFC-2A and AFC-2B Experiments,” INL/EXT-07-12388, (Hayes, Utterbeck 2007). To facilitate verification that all specifications are met, a written plan guides all inspections of the experiments components. The inspection plan for the AFC-2 experiment is “AFC-2A and 2B Inspection Plan” (Hyde 2008).

Figure 1 shows the full irradiation test assembly, capsule assembly and rodlet assembly. The irradiation test assembly consists of the experiment basket and capsule assembly, which contains six vertically stacked rodlet assemblies. The experiment basket of the test assembly is designed to interface the capsule assembly with the ATR and to act as a thermal neutron flux filter. The current basket design is an aluminum-sheathed cadmium tube. The aluminum sheath accommodates a cadmium tube thickness between 0.021 and 0.045 in. For the AFC-2A and 2B experiments, the cadmium thickness is the same as in the previous experiments, which is 0.045 in. The decrease in the thermal neutron flux will result in a reduction in the linear power in the fuel rodlets, which is necessary to meet the experiment design conditions.

The capsule assembly function is the following: (1) provide a second, robust barrier between the water coolant and the fuel, sodium and fission products, and (2) provide additional free volume for expansion of helium and fission gases should the cladding of any number of rodlets be breached during irradiation. Table 3 summarizes relevant design data for the capsule assembly. The capsule assembly was fabricated to meet the intent of the American Society of Mechanical Engineers (ASME), Section III, Class 1 Pressure Vessel Code Requirements. The capsule assembly design was identical in both experiments.

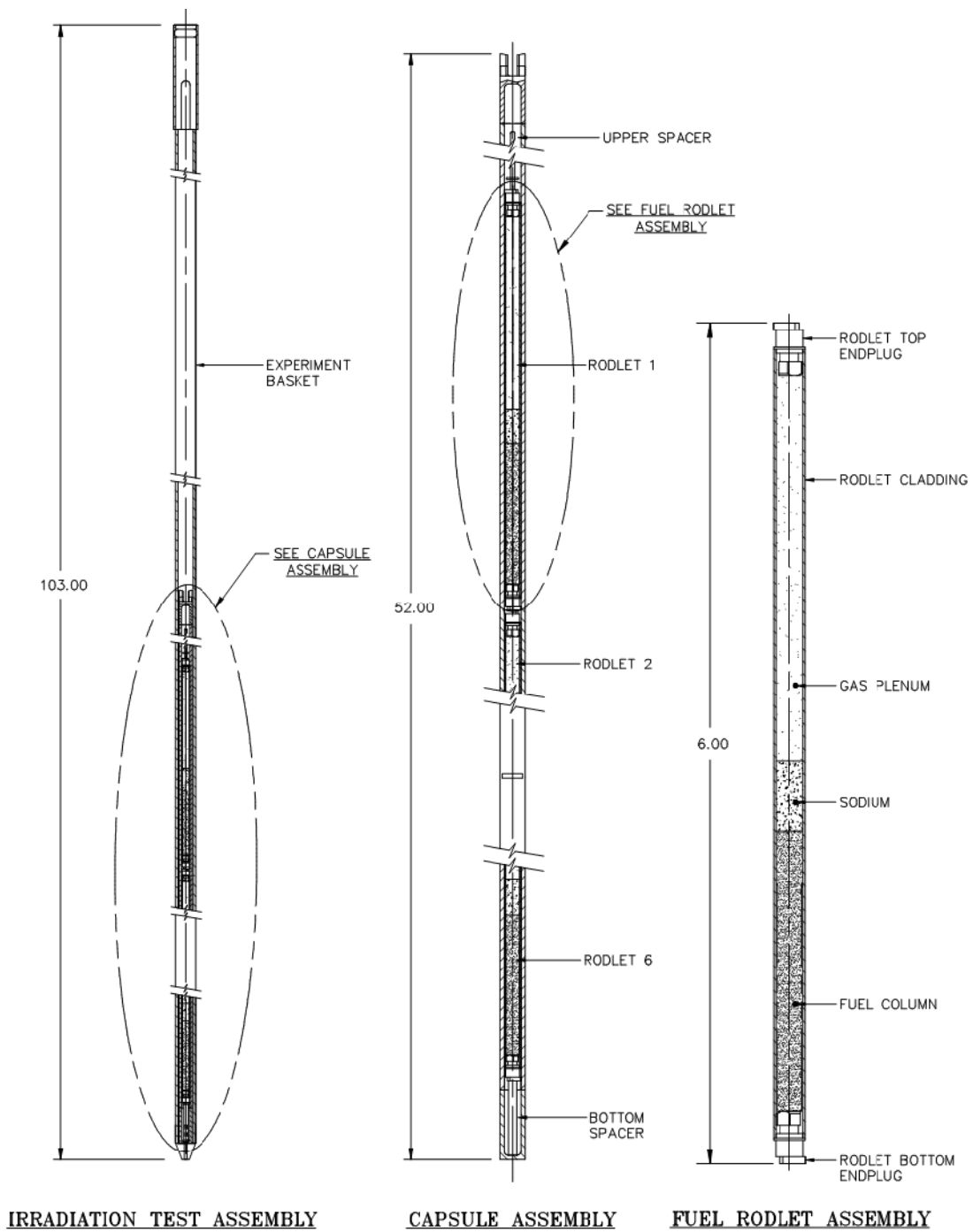


Figure 1. AFC-2 series irradiation test assembly for ATR east flux trap positions.

Table 3. Design data for capsule assembly.

Design Parameter	Value
Capsule Material	316SS
Capsule O.D.	0.354-in.
Capsule I.D.	0.234-in.
Capsule Length	52.000-in.
Capsule Free Volume	15.56 cm ³
Capsule-Rodlet Gap	0.0022-in.

The rodlet assembly is designed as a miniature length, fast reactor fuel rod. The rodlet assembly consists of the metallic fuel column, bond sodium, stainless steel Type 421 (HT-9) cladding and an inert gas plenum. The capsule, rodlet and metallic fuel radial dimensions are shown in Figure 2. The annular gap between the fuel column and rodlet inner diameter is initially filled with sodium and is designed to accommodate fuel swelling during irradiation. The annular helium-filled gap between the rodlet outer diameter and capsule inner diameter is designed to provide the thermal resistance necessary to achieve the design irradiation temperature of the fuel specimen.

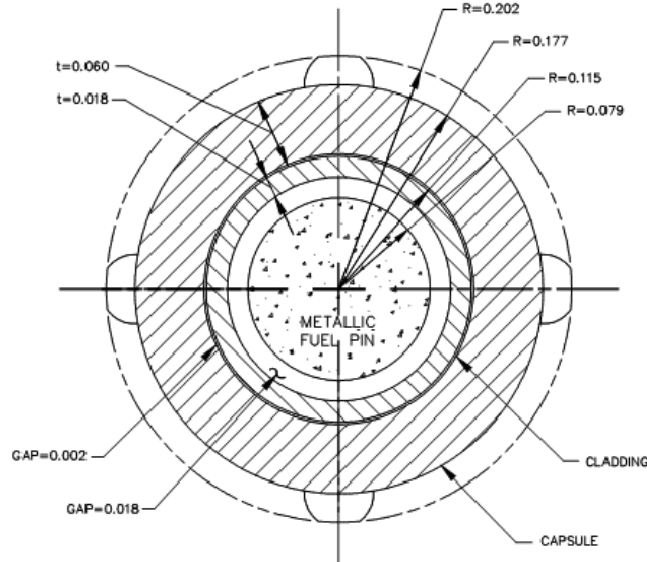


Figure 2. Radial dimensions of capsule and fuel rodlet assemblies for the AFC-2 metallic fuel tests.

Figure 3 shows the fuel rodlet assembly axial dimensions. Table 4 shows the materials used in constructing the rodlets along with their radial design dimensions. The design length of the metallic fuel column is 1.5 in.; the metallic fuel column may consist of a maximum of two slugs,

and the design diameter is 0.168 in. The bond sodium is designed to cover and exceed the fuel column height by between 0.25 and 0.50 in. The cladding for all rodlets is 6.0 in. long (including welded endplugs) with 0.230-in. outer diameter and 0.194-in. inner diameter.

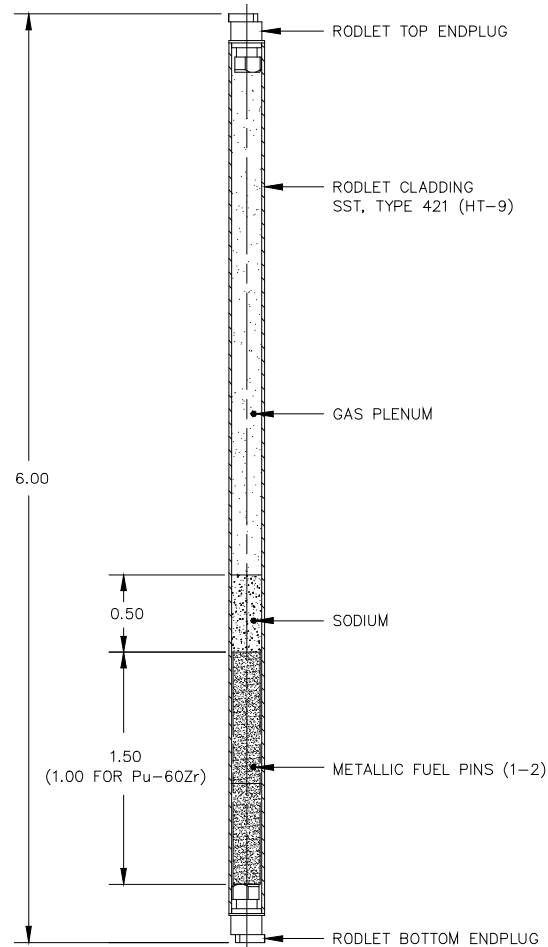


Figure 3. Rodlet assembly axial dimensions for the AFC-2 metallic fuel tests.

Table 4. Fuel rodlet design data.

Design Parameter	AFC-2A & B
Cladding Material	421SS (HT9)
Cladding O.D.	0.230 in.
Cladding I.D.	0.194 in.
Bond Material	Sodium
Fuel Type	Metallic Alloy
Fuel Smear Density	75%
Fuel Porosity	0%
Fuel O.D.	0.168 in.
Fuel Height	1.50 in.

Table 5 shows fuel experiment design conditions for the AFC-2 experiment. The objective is for each rodlet in these experiments to have a peak linear heat generation rate (LHGR) of 33.0 kW/m. The LHGR for each rodlet was calculated using the MCNp Coupled with ORIGEN2 (MCWO) analysis methodology. The final uranium enrichment value for each rodlet was based on these results.

Table 5. AFC-2A and AFC-2B experiment specifications.

Performance Parameter	AFC-2
Maximum Burnup	30 at.-%
Peak Rodlet Linear Power	
- Normal Operation	35 kW/m
- Off-Normal Limit	50 kW/m
Peak Cladding Temperature	
- Normal Operation	550°C
- Off-Normal Limit	650°C
Fuel Temperature	
- Normal Operation	900°C
- Off-Normal Limit	1100°C

The peak cladding temperature should not exceed 550°C during normal operation and 650°C during off-normal conditions. The expected peak thermal conditions during irradiation for these experiments were estimated based on the linear powers calculated by MCWO. In addition, the plenum pressures expected in each rodlet at a maximum burnup of 30 at.-% (i.e., depletion of initial Pu-239 + U-235) was conservatively estimated to confirm that the total pressure on the capsule assembly (the safety class boundary) will not exceed 370 psi (established as the pressure limit from mechanical analysis) during irradiation.

My role in the process described from here on was to oversee the entire fabrication and sample sectioning. This included writing guidance and control documents, arranging component fabrications, inspections, fuel movements, technique development, fuel casting and final assemblies. For characterization of the fuel, I restored the thermal mechanical analyzer (TMA) to operation and performed the TMA operations and data reduction. The remainder of the characterization activities was performed by others mentioned in the acknowledgments. For this thesis, I condensed and refined their work to be presented in this format.

2. FABRICATION AND EXPERIMENTAL RESULTS

All of the activities in the fabrication and experimental results section were performed directly or overseen by myself. Figure 4 shows the fabrication flow diagram for the AFC-2 experiments. This figure was used to guide fabrication and will be used in this document to guide the description of activities.

2.1 Fuel Slug Fabrication

This section will describe the fabrication of the metal fuel slugs that were tested. The process of taking raw feedstock and turning it into experimental fuel involves alloy mixing, homogenizing, and casting. The following paragraphs describe this process, the actual fuel that was cast, and samples that were cut from the original casting.

Alloy mixing consisted of mixing the raw materials as required to make the appropriate alloy specified in the fuel specification and is simply the process of weighing each needed constituent (see Figure 5) and getting it ready to melt together into a new alloy. Mixing control and direction is established by using facility procedures.

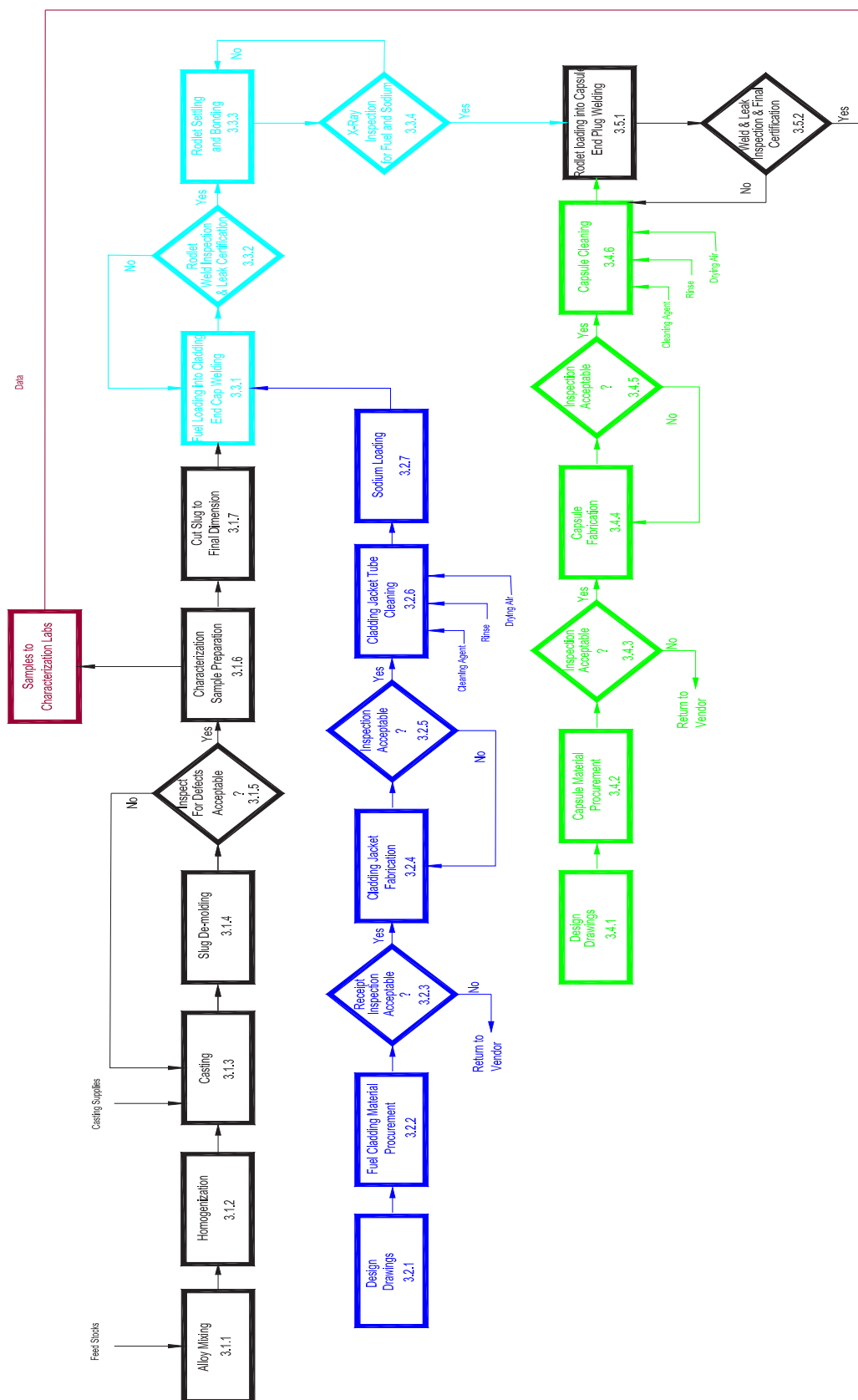


Figure 4. AFC-2 fuel, rodlet, and capsule fabrication.

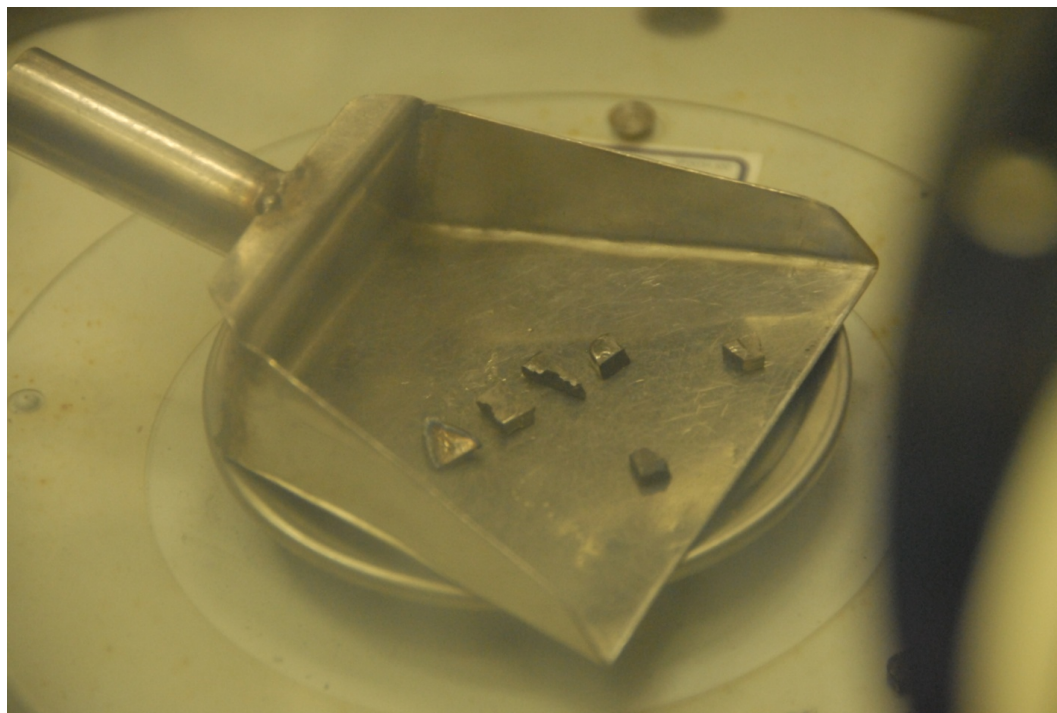


Figure 5. Fuel feedstock pieces in weighing pan.

Homogenization is the process of melting the alloy components together using an arc melting furnace. Each alloy was homogenized three times before casting. Figure 6 shows a once-melted button.

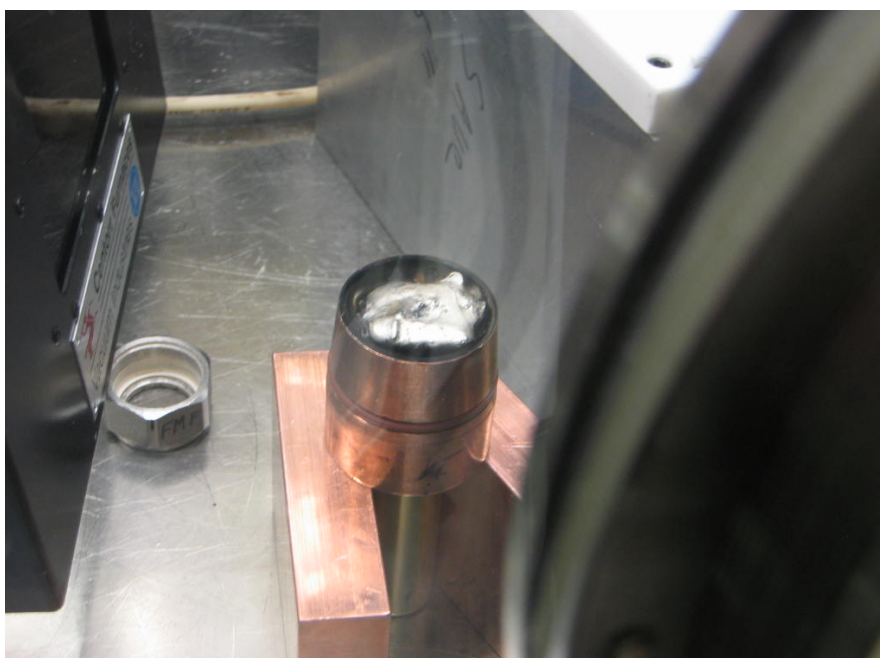


Figure 6. Alloy button on copper hearth.

Three of the six alloys needed for the complete experiment were cast in the Casting Laboratory (CL) using a suction casting technique developed for use in the CL. This technique uses the arc melting furnace to melt the alloy, followed by placing the open end of a quartz tube into the molten alloy. When the tube (mold) is in the molten alloy, a second operator draws a vacuum on the other end of the tube and the alloy is drawn (cast) inside the quartz tube, where it solidifies into a solid slug. Figures 7 and 8 show the suction casting process. Casting was performed using a 0.175 in. I.D. quartz tube that yields a fuel slug of 0.168-in. diameter. The quartz tube consists of old EBR-II casting tubes. Zirconium Oxide (ZrO_2) “mold wash” can be used to coat the molds if needed. The “mold wash” releases the mold and prevents the slug from sticking to the quartz. This was performed at the discretion of the operator/technician doing the casting. This technique was developed to address Am volatilization problems experienced in the past using vacuum injection casting (Trybus, Sanecki, and Henslee 1993).

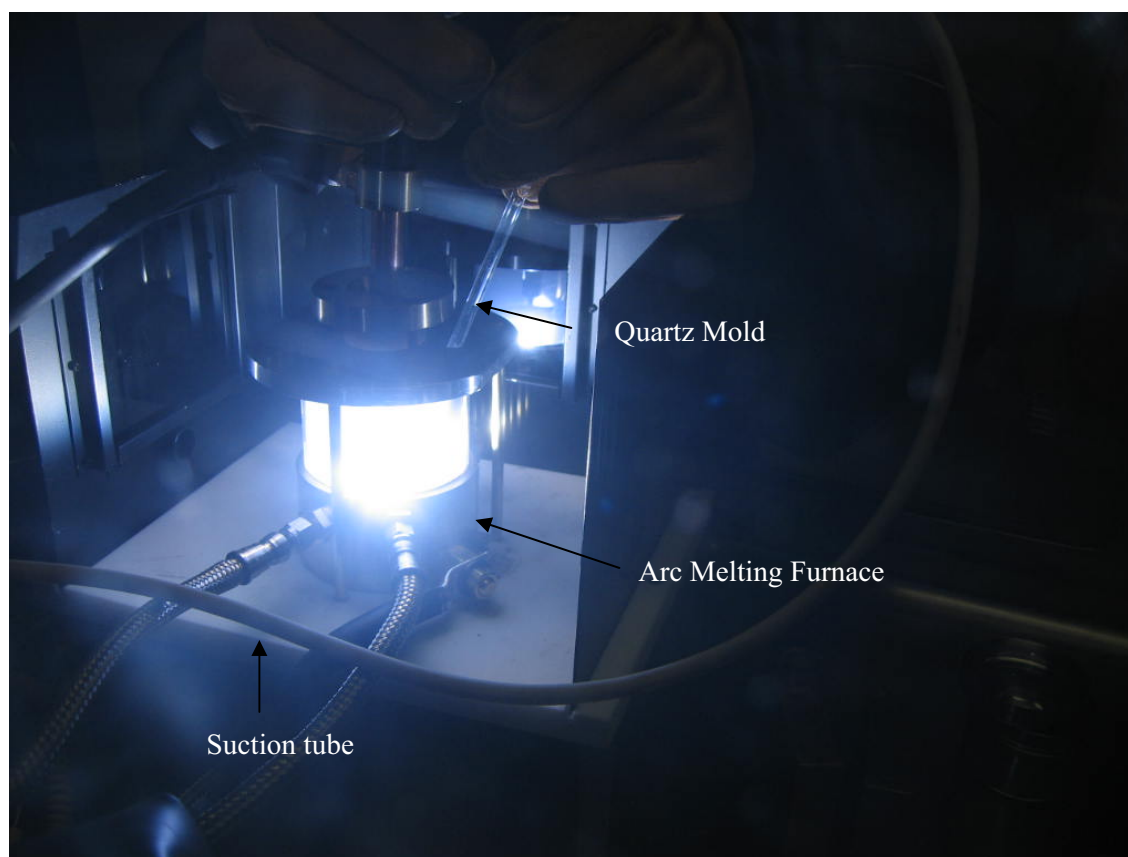


Figure 7. Arc melting furnace ready for suction casting.

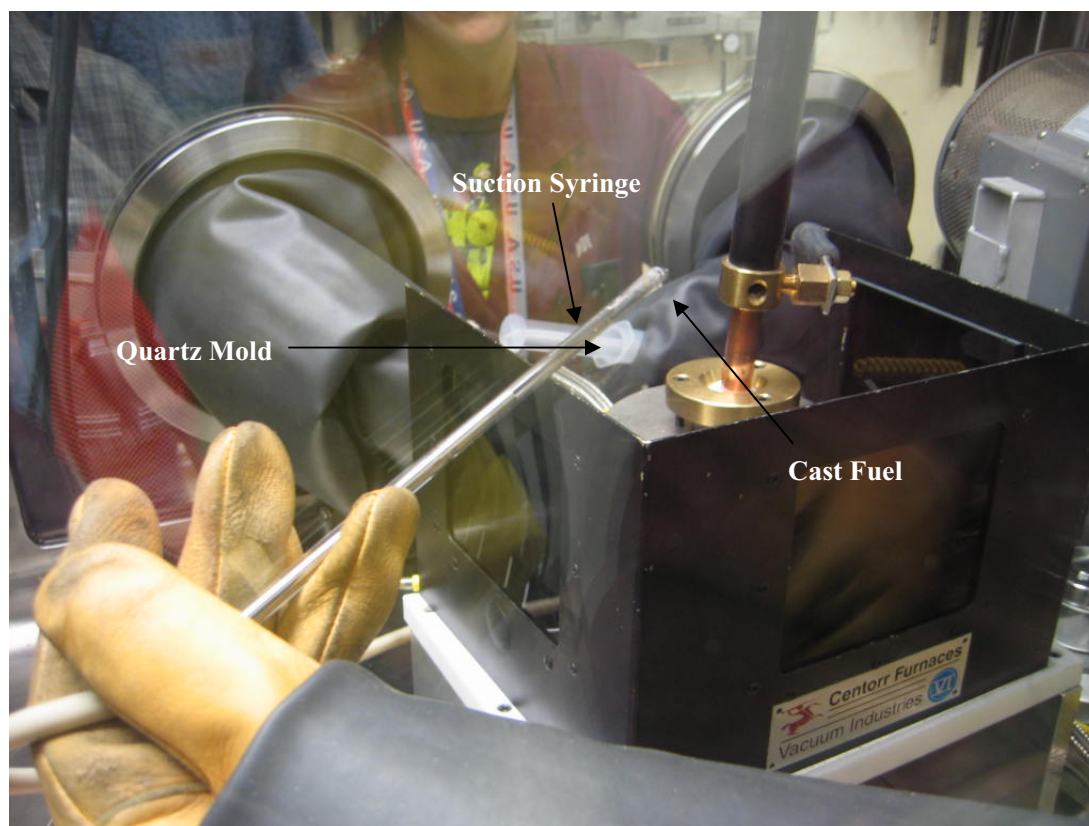


Figure 8. Suction cast fuel after cooling.

The suction casting technique has been used on many experimental fuel fabrication campaigns, but it is inconsistent and dependent on the experience of the technician doing the casting. As a result, it is difficult to repeat castings and each remelt negatively affects the flow characteristics of the melt. As a result, a new casting technique was developed by Gavin Knighton. This investigation was constrained to use the arc melting furnace power supply and, if possible, use the existing safety envelope developed for the arc melting furnace.

The first radiologically cold engineering evaluations were performed using a resistance-heating technique (see Figure 9) and coated carbon crucibles. This technique had potential, but carbon contamination seems to dramatically affect alloy behavior, especially after repeated melts. As a result, the resistance-heating technique was not completely developed for glovebox implementation.

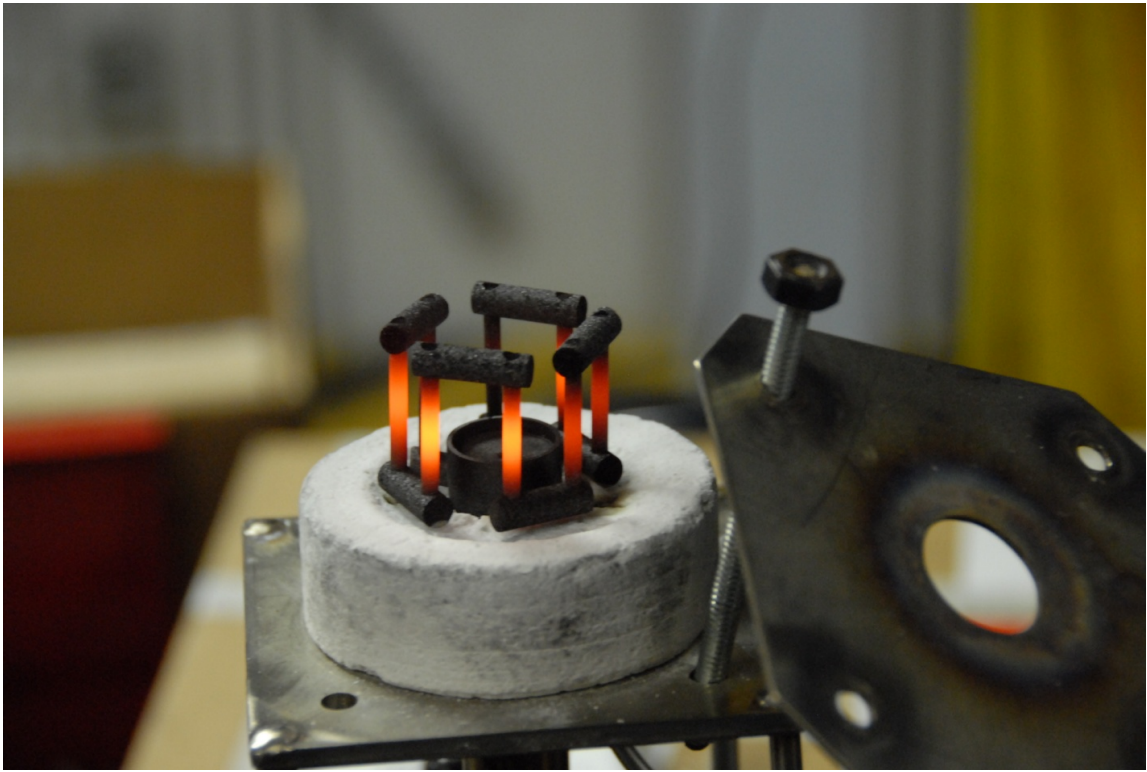


Figure 9. Resistance-heated furnace elements.

A new drop-casting technique, a refinement of a previously used gravity-casting process, was also investigated. This process uses the arc melting furnace, but instead of relying on suction to draw up molten material, it uses a small copper hearth with a hole in the middle for electrical conduction and a ceramic hearth for thermal insulation. This setup allows enough heat to remain in the melt until the material becomes completely molten (and with some super heat) and flows into the quartz mold in the center of the copper hearth. Figure 10 shows a new drop-casting hearth. Other casting techniques were investigated (Crawford et al. 1993; Harbur, Anderson, and Maraman 1970; Kruger 1966) and it was determined the new technique would not affect behavior during irradiation or characterization.

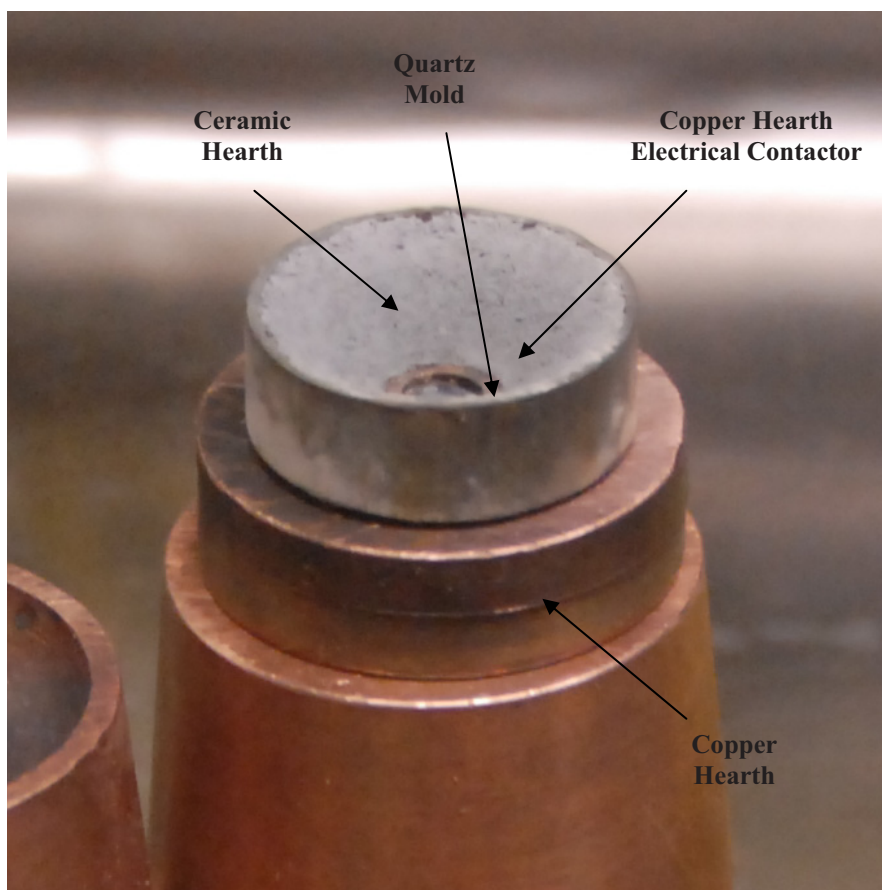


Figure 10. New drop-casting hearth(s).

Repeated castings with this technique and the same ceramic hearth produces a copper-looking coating on the hearth (see Figure 11). Analysis indicates drop casting produces no significant copper contamination in the fuel. Figure 12 shows a cast fuel slug inside the quartz mold.

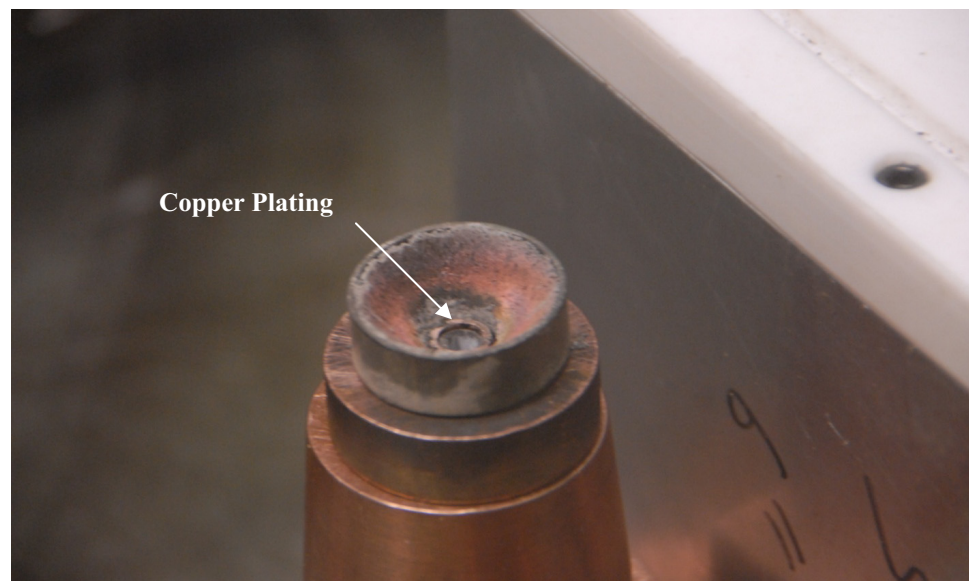


Figure 11. Drop casting hearth after several castings.



Figure 12. Inverted hearth(s) showing fuel inside quartz mold.

The white inside the quartz mold is the zirconia wash that can be used for coating. This technique was implemented in the AFCI glovebox to cast the last of the AFC2 experimental fuel. Figure 13 shows a successful 2-in. fuel casting.

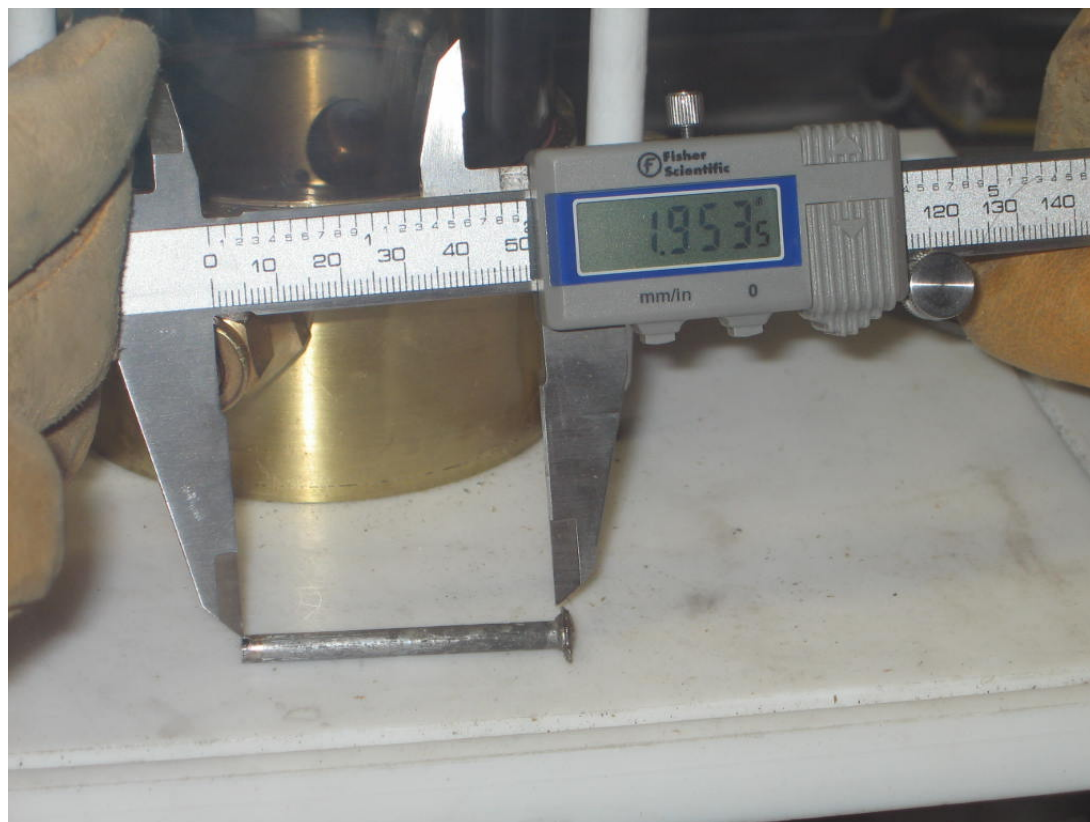


Figure 13. Drop-cast fuel slug.

The conclusion contains information on future research scale casting techniques. These techniques were not considered for AFC-2, because implementing their use in an existing glovebox is outside the existing scope of work and funding. However, investigating them for future use was deemed worthwhile.

The following samples were prepared for each alloy for analysis by Fuels Characterization personnel and Analytical Laboratory (AL) personnel. These samples were used for meeting the technical and functional requirements of the fuel specifications as well as for scientific studies and to generate data for other material property reports (Table 6 outlines the general requirements for the samples). The Buehler Saw, used for sectioning, appears in Figure 14.

Table 6. General characterization samples needed.

Analysis	Technique	Sample size		Mass (mg)	No. Samples
		Length (mm)	Diameter (mm)		
Elemental and isotopics	ICP-MS/ICP-AES			~500	1-2/cast [#]
Heat capacity	DSC	1.0-1.2	5.4*		≥2
Thermal expansion	TMA	5.0 - 12.0	4.0 - 10.0		≥1
Thermal diffusivity	LFD	1	11.0 - 12.5		≥1
	LFD	1.5	11.0 - 12.5		≥1
	LFD	2	11.0 - 12.5		≥1
As-cast phase Identification	XRD	1.0 - 1.2	4.0 - 5.0		3
Microstructure	SEM	1.0 - 2.0	4.0 - 5.0		≥1
FCCI	SEM	2.0 - 5.0	4.0 - 5.0		≥3
Annealed sample	XRD, SEM, TA	10.0 - 15.0	4.0 - 5.0		1

* Optimal diameter, however 4.0-5.0 diameter material will work.

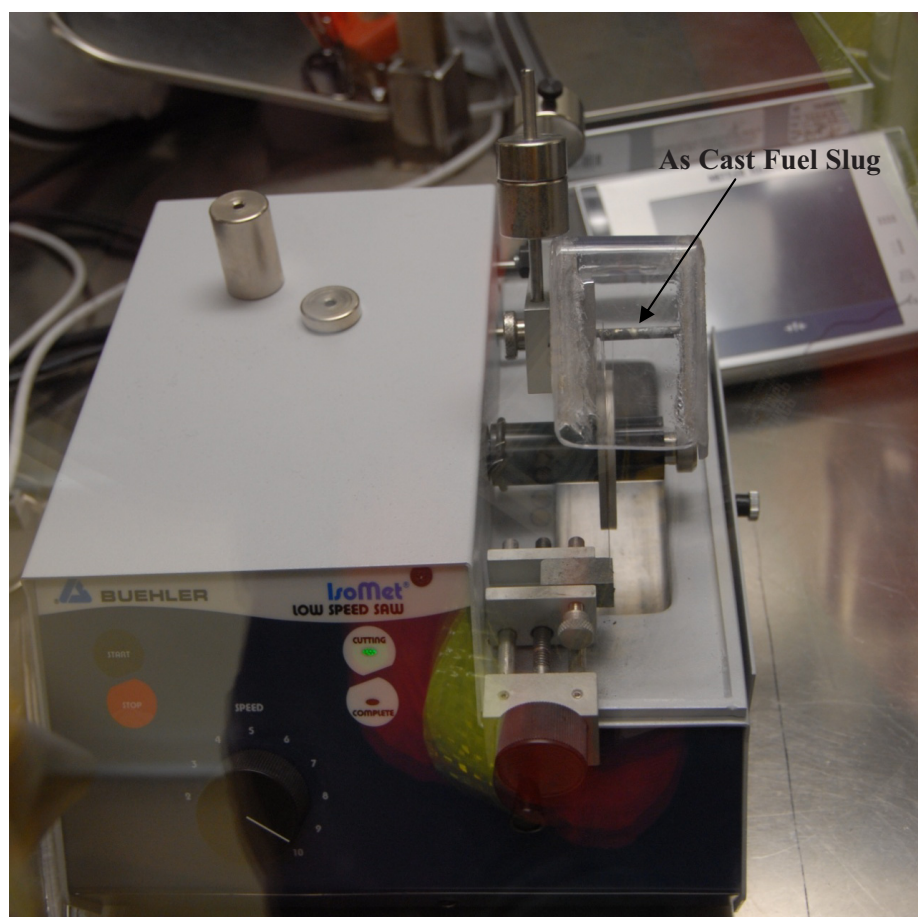


Figure 14. Sectioning samples using the Buehler Saw.

60U-20Pu-3Am-2Np-15Zr (A1) alloy was completely cast in the CL and sectioned for characterization in the Waste Form Testing Glovebox. The CL glovebox is an argon atmosphere glovebox operated at less than 50 ppm oxygen. Waste form testing is a negative pressure, air glovebox. In addition, the fuel is sectioned using water as a lubricant for the Buehler Saw.

A total of five slugs were cast in order to achieve all of the fuel and samples that were needed. Four slugs, approximately 0.75 in. each, were used as fuel for rodlets. The remainder of the material was sectioned as six chemistry and isotopics samples, two for scanning electron microscope (SEM), three Differential Scanning Calorimetry (DSC), three x-ray diffraction (XRD), and one TMA sample. An additional larger diameter laser flash diffusivity (LFD) sample was cast and sectioned into two LFD sections for analysis. The two SEM samples were mounted and polished and were transferred to the Electron Microscopy Laboratory (EML) for SEM analysis. Figure 15 shows representative pictures of the fuel and samples.

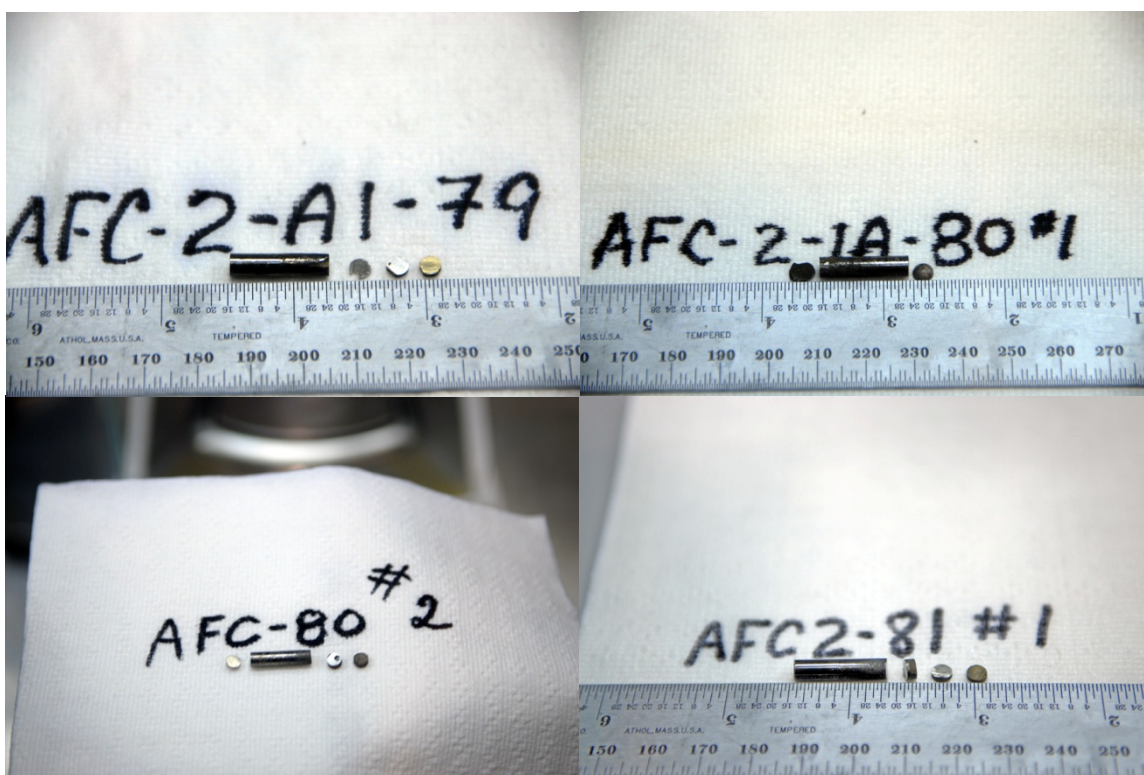


Figure 15. 60U-20Pu-3Am-2Np-15Zr (A1) fuel slugs and characterization samples.

The rare earth alloy consisting of 6% La, 16% Pr, 25% Ce, 53% Nd was alloyed using an arc-melting furnace in the INL Research Center (IRC). This alloy was also chemically analyzed and verified for use in the AFC-2 fuel.

59U-20Pu-3Am-2Np-1RE-15Zr (A2) was cast and sectioned in the Fuel Manufacturing Facility inside the new Advanced Fuel-Cycle Initiative (AFCI) glovebox. A total of four slugs were cast using the drop-casting technique. Two slugs were used as fuel; the remainder was sectioned into samples. A sample was sectioned from each of the fuel slugs for chemistry and isotopics, five 1-mm samples were sectioned for SEM, DSC, or XRD and two 2-mm samples were sectioned for diffusion couples. The remaining slug material was used for archiving, thermal-mechanical analysis (TMA), and anneal samples. The LFD sample remains to be cast. Figure 16 shows representative pictures of the fuel slugs and 1-mm samples.

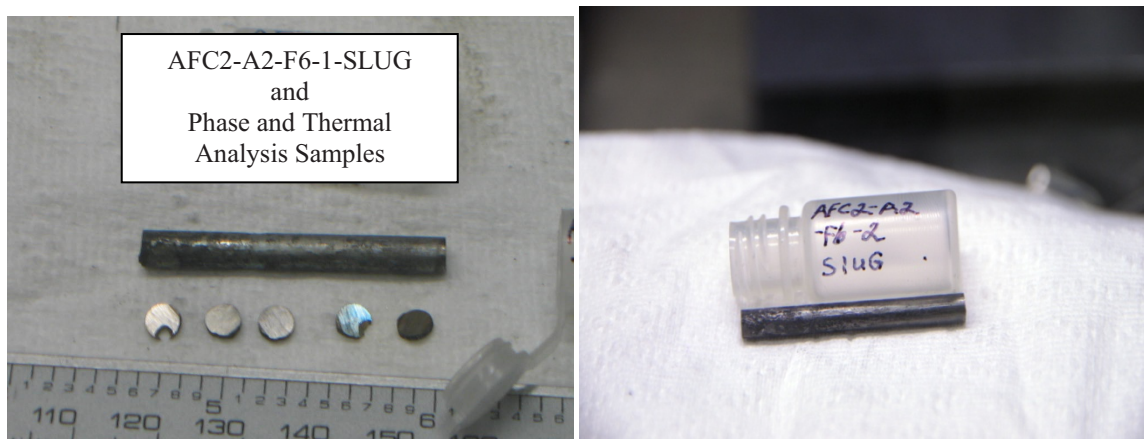


Figure 16. 59U-20Pu-3Am-2Np-15Zr (A2) fuel slugs and characterization samples.

58.5U-20Pu-3Am-2Np-1.5RE-15Zr (A3) alloy was completely cast in the CL and sectioned for characterization in the Waste Form Testing Glovebox. A total of four slugs and a 12-mm-diameter laser flash sample were cast to achieve all of the needed fuel and samples. Three slugs were cut from these original castings to be used as fuel for rodlets (Figure 17). The remainder of the material was sectioned as six chemistry and isotopics samples, two SEM, three DSC, three XRD, two LFD and one TMA sample. The two SEM samples were mounted and polished and were transferred to EML for SEM analysis.

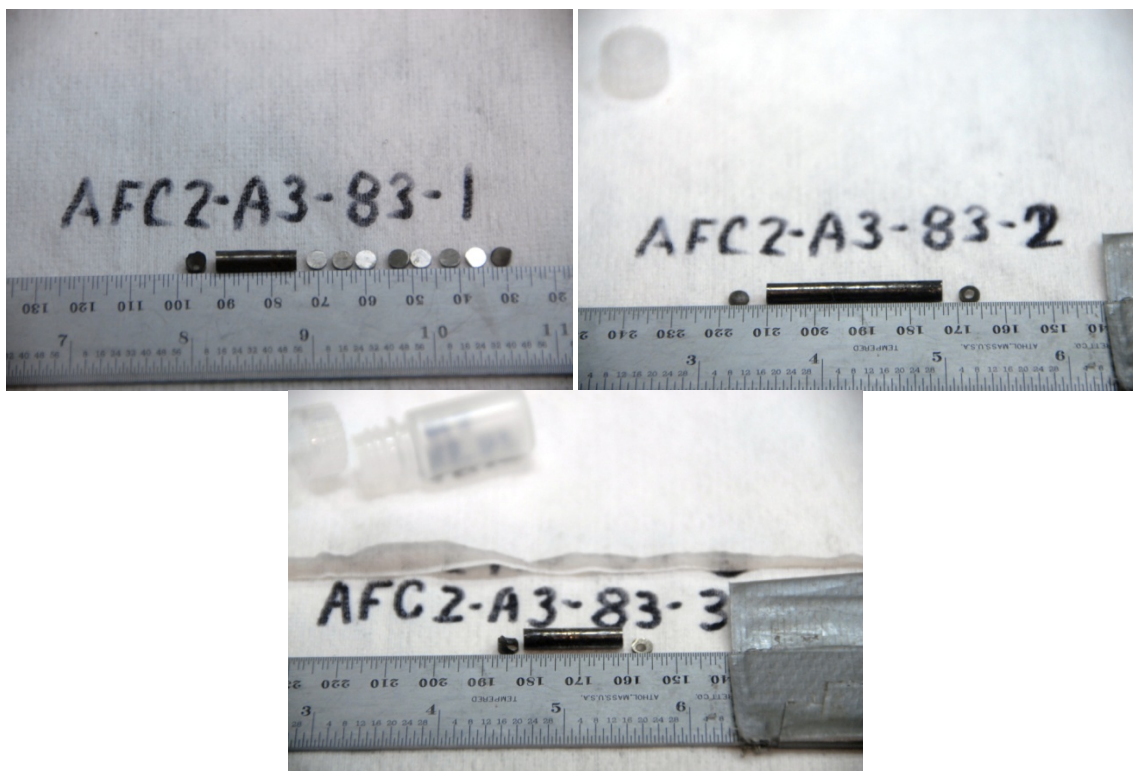


Figure 17. 58.5U-20Pu-3Am-2Np-1.5RE-15Zr (A3) fuel slugs and characterization samples.

40.5U-30Pu-5AM-3Np-1.5RE-20Zr (A4) was cast and sectioned in the AFCI glovebox; a total of three slugs were cast using the drop-casting technique. Two slugs were used as fuel; the remainder was sectioned into samples. A sample was sectioned from each of the fuel slugs for chemistry and isotopics; in addition, a second sample was taken from one slug to verify homogeneity. Two 1-mm samples were sectioned for SEM, DSC, or XRD. The remaining slug material was used for archiving, TMA, and anneal samples. The LFD sample still remains to be cast. Figure 18 shows representative pictures of the fuel slugs.

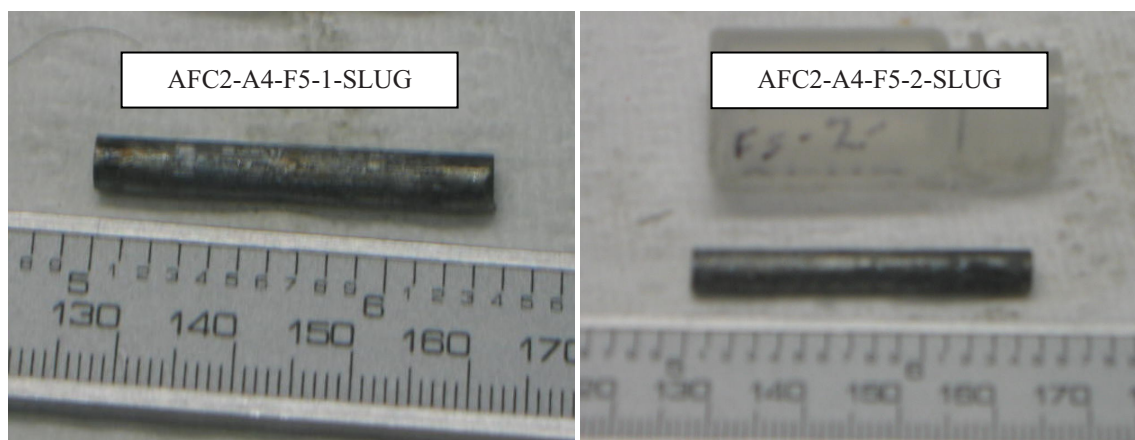


Figure 18. 40.5U-30Pu-5Am-3Np-1.5RE-20Zr (A4) fuel slugs.

41U-30Pu-5Am-3Np-1RE-20Zr (A5) was cast and sectioned in the AFCI glovebox; a total of five slugs were cast using the drop-casting technique. Four slugs were used as fuel; the remainder was sectioned into samples. A sample was sectioned from AFC2-A5-F4-3, AFC2-A5-F4-4, and AFC2-A5-F4-5 slugs for chemistry and isotopics. AFC2-A5-F4-2 is a small 7.21-mm slug; AFC2-A5-F4-3 was cast immediately after, so it is assumed to have the same chemistry. Five 1-mm samples were sectioned for SEM, DSC, or XRD. The remaining slug material was used for archiving, TMA, and anneal samples. The LFD sample still remains to be cast. Figure 19 shows representative pictures of the fuel slugs and samples.

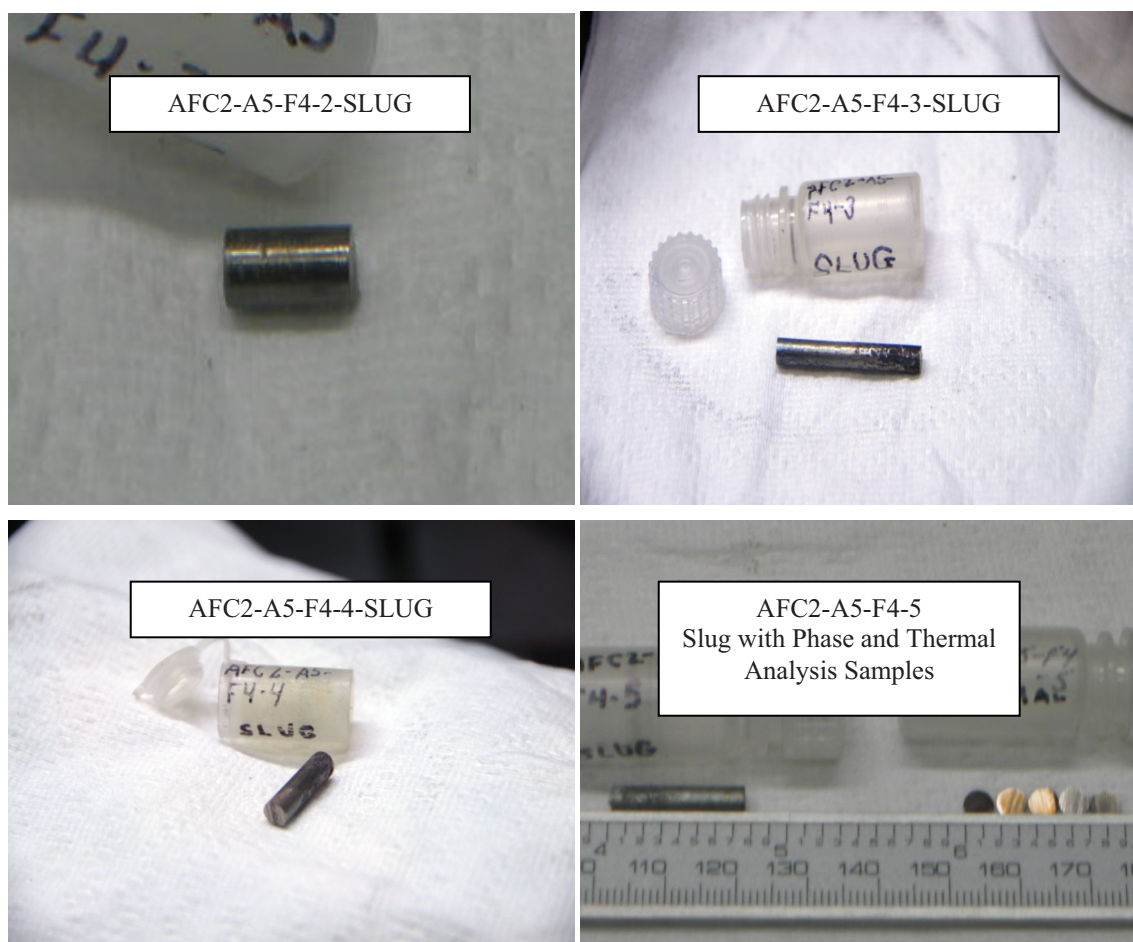


Figure 19. ^{41}U - ^{30}Pu - ^{5}Am - ^{3}Np - ^{1}RE - ^{20}Zr (A5) fuel slugs and samples.

^{42}U - ^{30}Pu - ^{5}Am - ^{3}Np - ^{20}Zr (A6) alloy was completely cast in the CL and sectioned for characterization in the Waste Form Testing Glovebox. A total of six slugs and a 12-mm-diameter laser flash sample were cast to achieve all of the needed fuel and samples. Four slugs cut from these original castings are to be used as fuel. The remainder of the material was sectioned as seven chemistry and isotopics samples, two SEM, three DSC, four XRD, three FCCI, two LFD and one TMA sample. The two SEM samples were mounted and polished and were transferred to EML for SEM analysis. Figure 20 shows fuel and characterization samples.

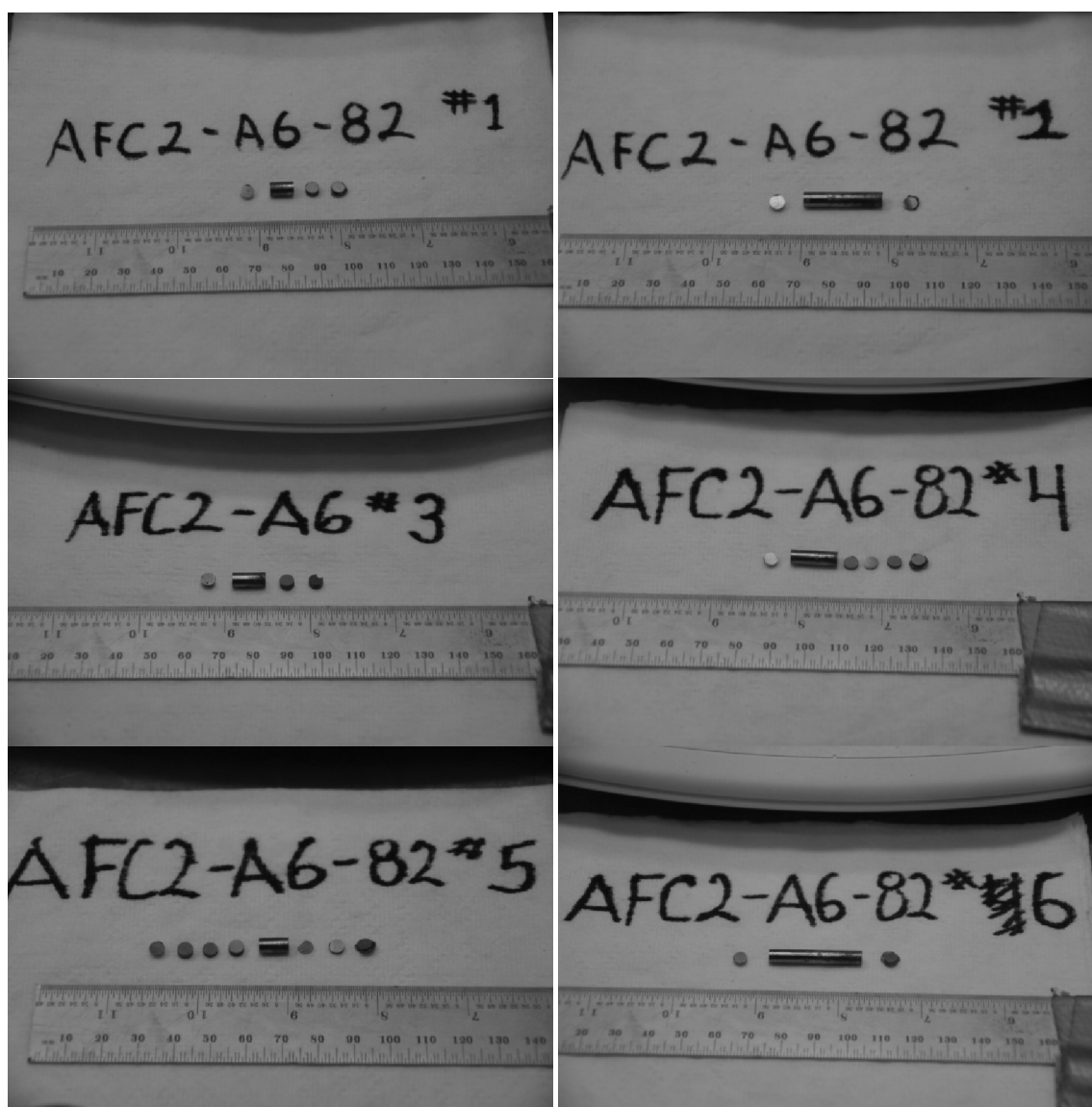


Figure 20. ^{42}U - ^{30}Pu - ^{5}Am - ^{3}Np - ^{20}Zr (A6) fuel slugs and characterization samples.

Fuel slugs used for the actual experiment are generally cut to length in conjunction with sample sectioning. Table 7 shows the data on fuel physical properties and casting source for AFC-2 fuel slugs. Density is determined by the Archimedes method when possible and, otherwise, by dimensional analysis. The fuel specification calls for the fuel to be within $\pm 5\%$ of the theoretical density of the alloy, determined by the rule of mixtures. This target density is included in Table 7 as well.

Table 7. AFC-2 fuel physical properties.

Slug Designation	Rodlet Designation	Mass (gr)	Length (mm)	Density (g/cc)	Target Density
AFC2-A1-79-ROD1	AFC2A-R1	4.068	19.24	*13.74	14.04
AFC2-A1-80-1-ROD1	AFC2A-R1	4.196	18.84	*14.50	14.04
AFC2-A1-80-2-ROD1	AFC2B-R1	3.888	18.24	*13.88	14.04
AFC2-A1-81-1-ROD1	AFC2B-R1	4.225	19.36	*14.07	14.04
AFC2-A2-F6-1-SLUG	AFC2A-R2	8.006	37.69	14.16	13.92
AFC2-A2-F6-2-SLUG	AFC2B-R2	8.047	38.05	14.10	13.92
AFC2-A3-83-1-ROD1	AFC2A-R3	3.664	17.36	*13.54	13.86
AFC2-A3-83-3-ROD1	AFC2A-R3	4.498	20.72	*13.93	13.86
AFC2-A3-83-2-ROD1	AFC2-XX	8.003	37.22	*13.77	13.86
AFC2-A4-F5-2-SLUG	AFC2A-R4	7.525	36.93	13.40	12.75
AFC2-A4-F5-1-SLUG	AFC2B-R4	6.814	35.02	12.97	12.75
AFC2-A5-F4-2-SLUG	AFC2A-R5	1.480	7.21	13.38	12.81
AFC2-A5-F4-3-SLUG	AFC2A-R5	5.910	30.58	12.71	12.81
AFC2-A5-F4-4-SLUG	AFC2B-R5	3.373	17.55	12.41	12.81
AFC2-A5-F4-5-SLUG	AFC2B-R5	3.747	19.08	12.92	12.81
AFC2-A6-82-2-ROD1	AFC2A-R6	4.628	23.33	*12.83	12.92
AFC2-A6-82-4-ROD1	AFC2A-R6	2.891	14.36	*12.88	12.92
AFC2-A6-82-5-ROD1	AFC2B-R6	1.731	8.58	*12.93	12.92
AFC2-A6-82-6-ROD1	AFC2B-R6	5.854	29.24	*12.89	12.92

* Archimedes

Requirements dictate each alloy fuel column to be one or two slugs totaling 1.5-in. long + 0, -0.2 (38.1 mm -33.02 mm) with a diameter of 0.168 in. + 0.001, -0.003 (4.29 mm – 4.19 mm). However, all six alloys did not shrink after cooling, as did a straight uranium/zirconium alloy. As a result, all fuel slugs were larger in diameter than was written in the fuel specification. The actual fuel was all 0.175 in +0.001, -0.003. In accordance with quality control requirements for irradiation experiments, this was documented in the As-Built Data Package and is covered under a Nonconformance Report (NCR).

In general, the fuel was all close to the target compositions. The fuel specification was written very tightly and, as a result, in accordance with quality control requirements for irradiation experiments, this was all documented for presentation to those responsible for experiment oversight. Figures 21–29 show the chemical analysis results from the cast fuel and the target compositions. The bars represent the errors associated with the measurement technique and the range associated with the fuel specification or target composition. The numerous data points

around the target composition represent each analysis performed on a given alloy, as a result some alloys have up to six data points represented.

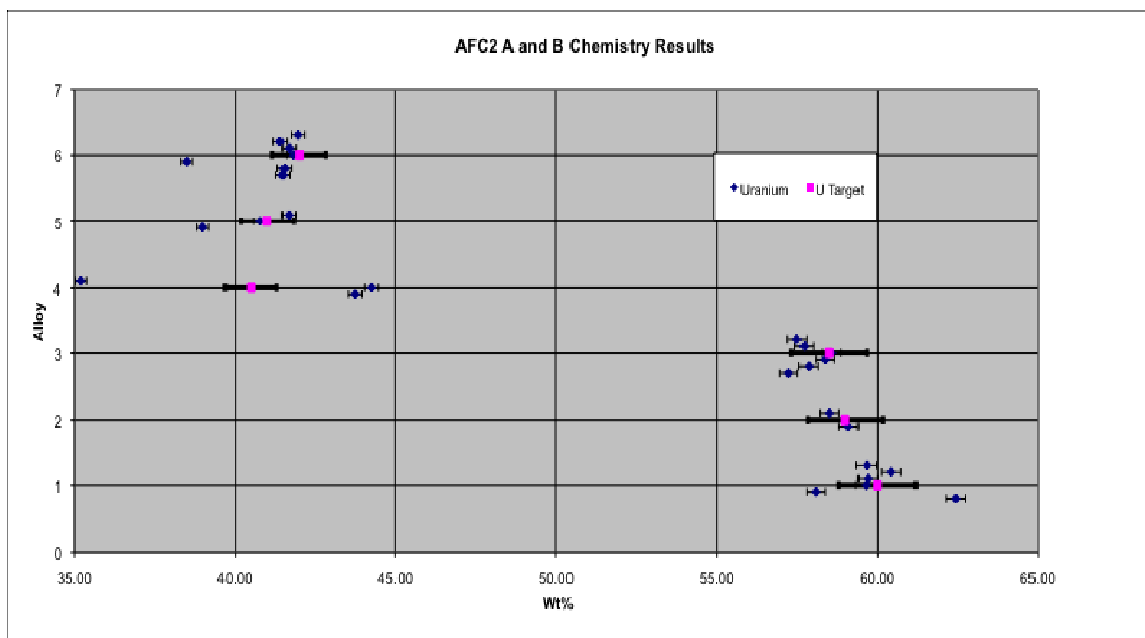


Figure 21. Uranium composition of cast fuel compared to target compositions.

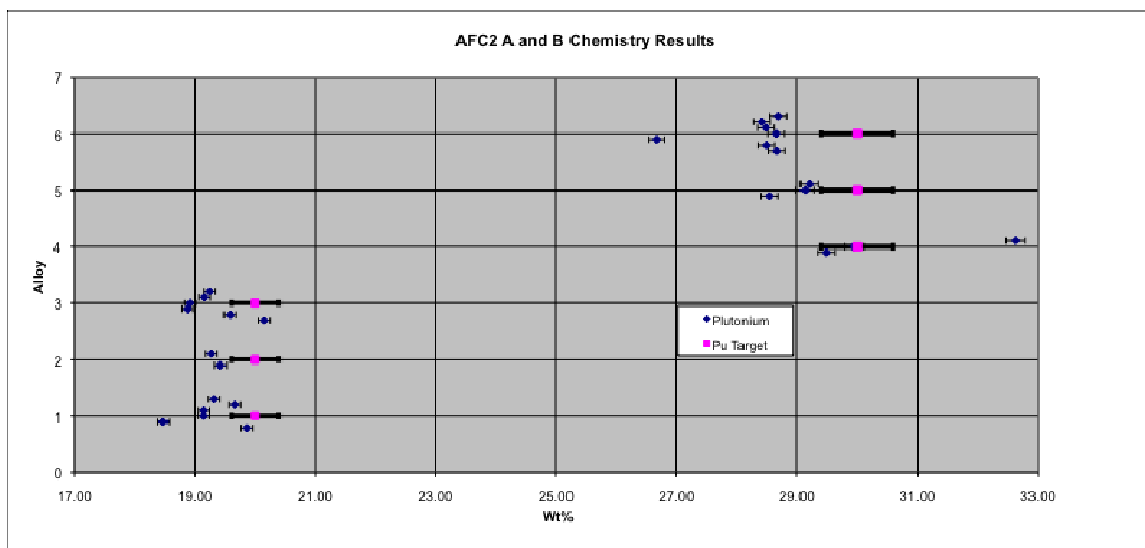


Figure 22. Plutonium composition of cast fuel compared to target compositions.

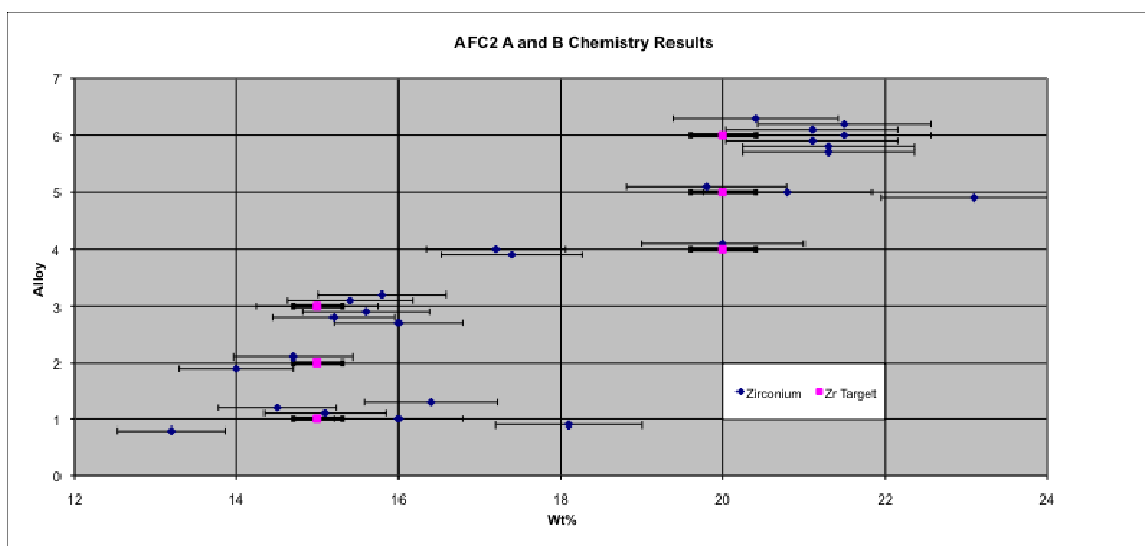


Figure 23. Zirconium composition of cast fuel compared to target compositions.

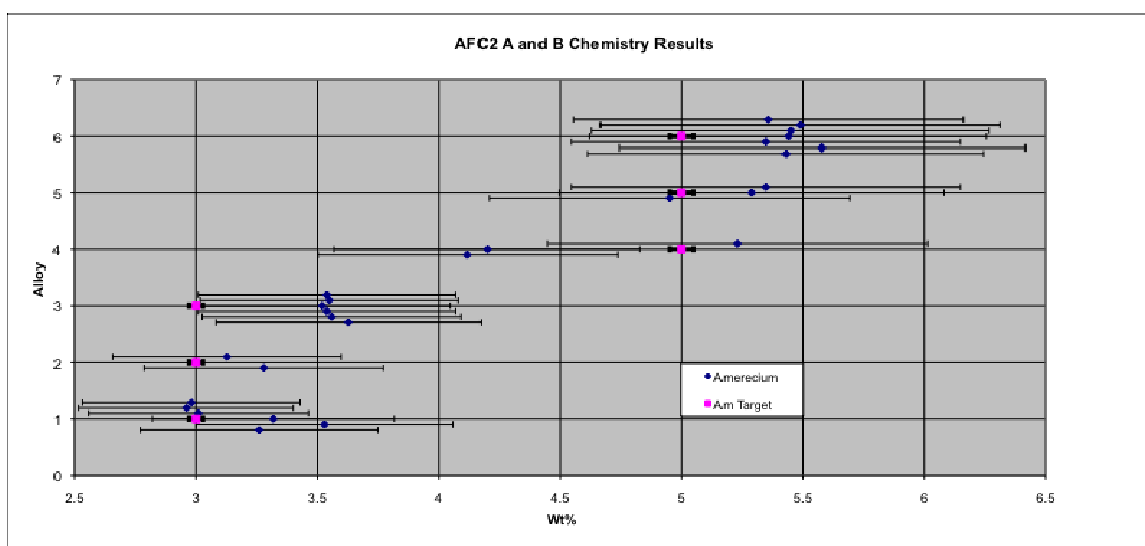


Figure 24. Americium composition of cast fuel compared to target compositions.

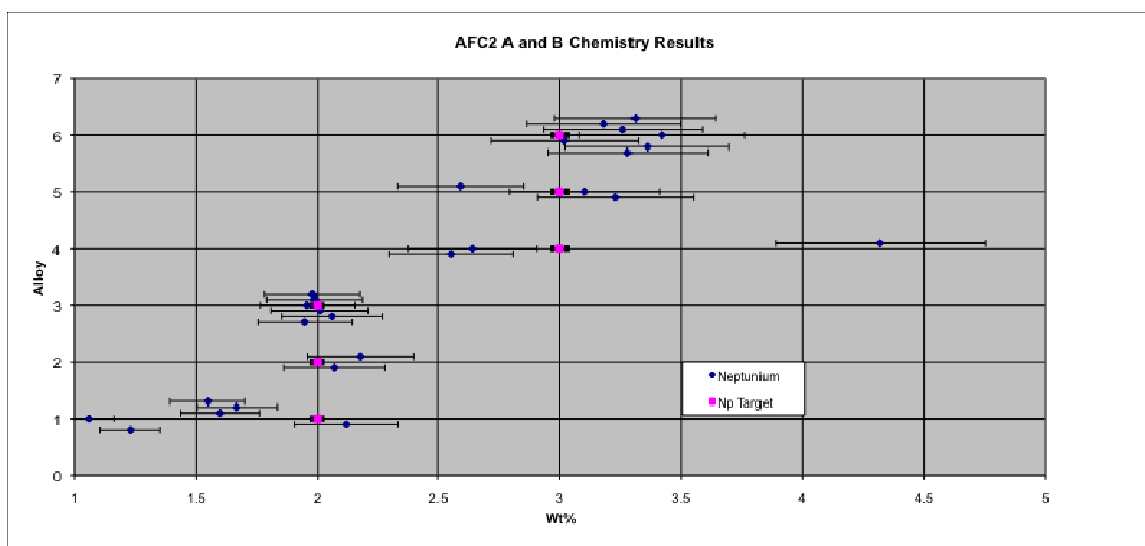


Figure 25. Neptunium composition of cast fuel compared to target compositions.

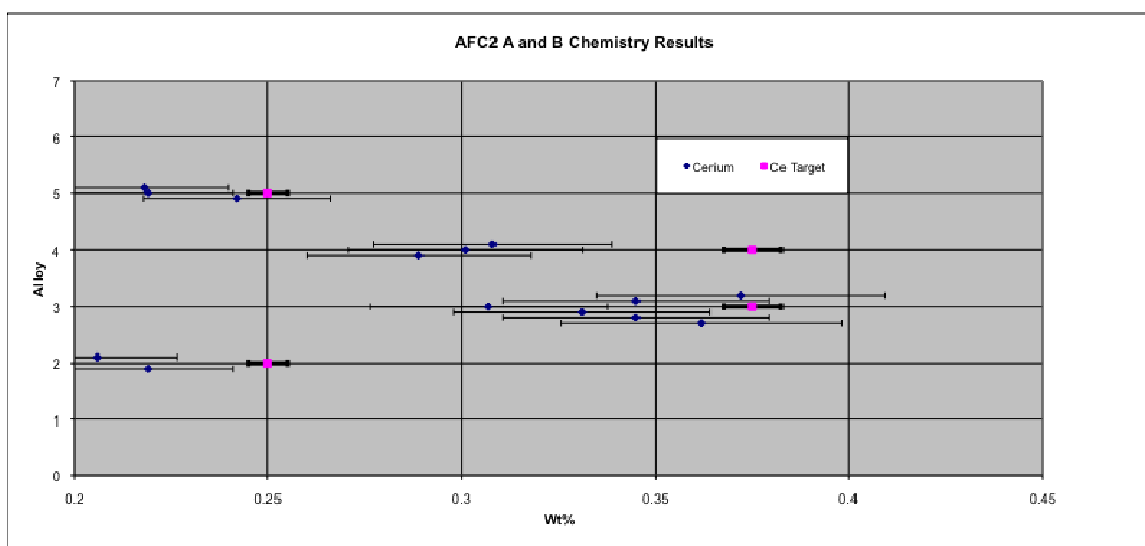


Figure 26. Cerium composition of cast fuel compared to target compositions.

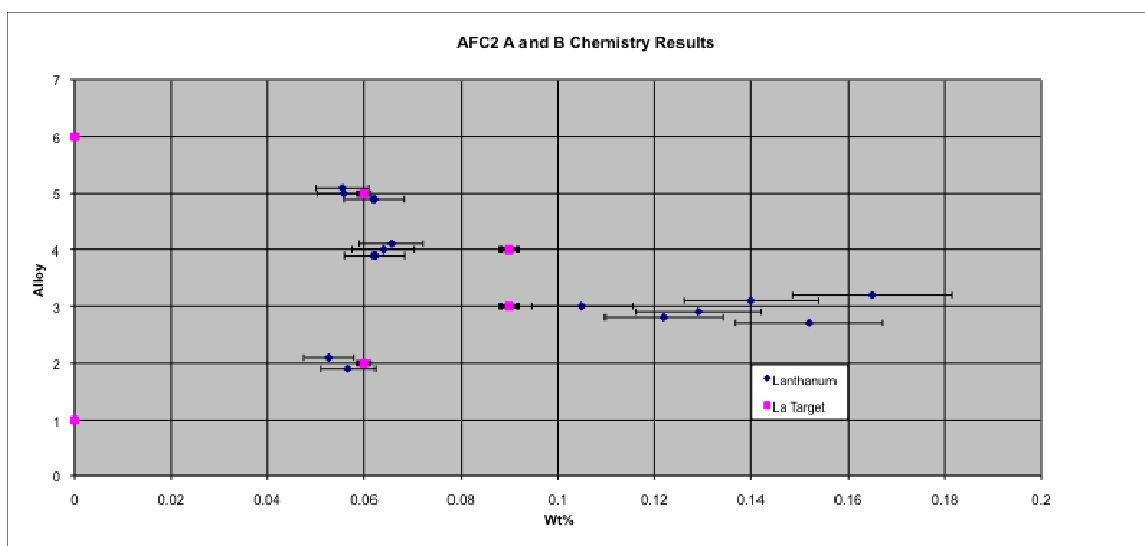


Figure 27. Lanthanum composition of cast fuel compared to target compositions.

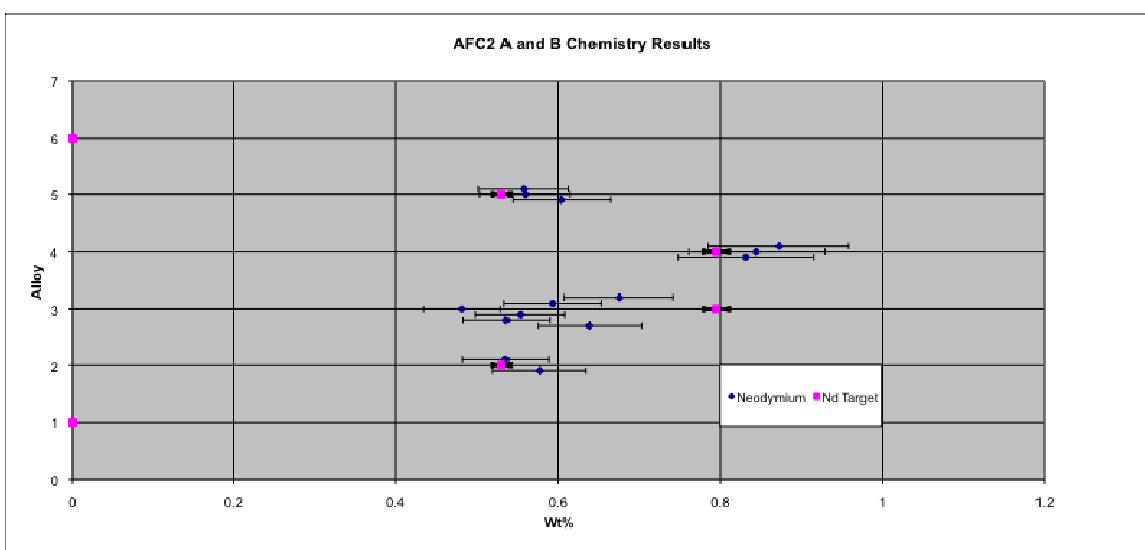


Figure 28. Neodymium composition of cast fuel compared to target compositions.

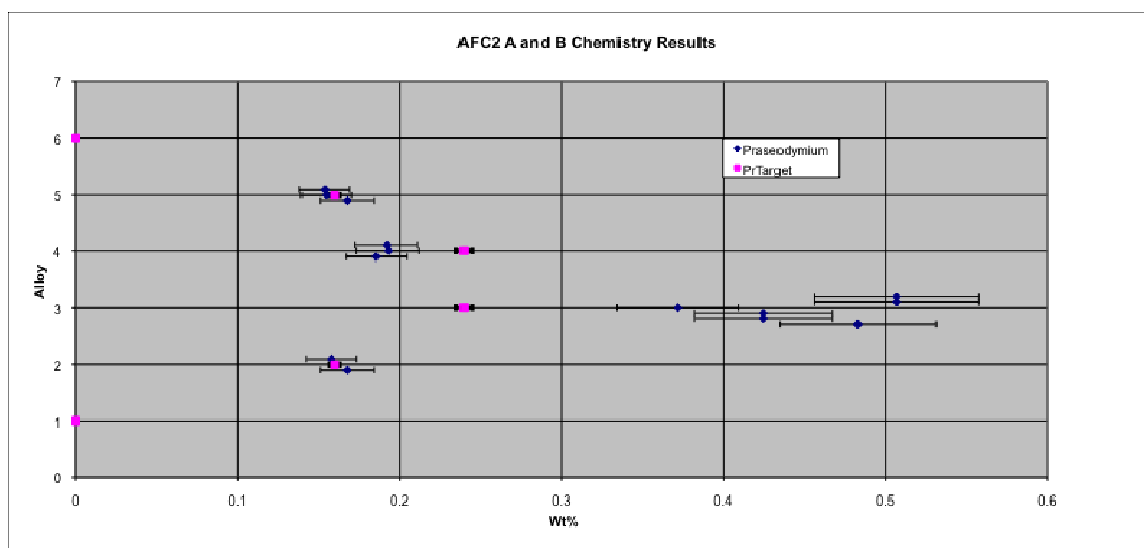


Figure 29. Praseodymium composition of cast fuel compared to target compositions.

Individually, each alloy has the following specific elemental issues:

- 60U-20Pu-3Am-2Np-15Zr (A1)

All samples from this alloy were reasonably close to the target composition. Pu is somewhat low but the others all have variations above and below the target wt%.

- 59U-20Pu-3Am-2Np-1RE-15Zr (A2)

Only two samples from this alloy were analyzed. For each element or group of elements the measured wt% with its error bars overlap with the target range.

- 58.5U-20Pu-3Am-2Np-1.5RE-15Zr (A3)

All elements, for all four samples of this alloy, overlap with the target range.

- 40.5U-30Pu-5Am-3Np-1.5RE-20Zr (A4)

This alloy did have significant variation from the target composition. At this time there is no explanation other than in homogeneities in the melt. No further testing has been done.

- 41U-30Pu-5Am-3Np-1RE-20Zr (A5)

Only two samples from this alloy were analyzed. For each element or group of elements the measured wt% with its error bars overlap with the target range.

- 42U-30Pu-5Am-3Np-20Zr (A6)

All samples from this alloy were reasonably close to the target composition. Pu is somewhat low but the others all have variations above and below the target wt%.

2.2 Cladding Fabrication

This section describes the fabrication and control of the cladding tubes and end plugs.

The design drawings for the rodlet components are all documented and controlled. Cladding used to encapsulate the fuel slugs for this test was excess Alloy HT-9 EBR-II cladding tubes. All cladding tubes are traceable to the manufacturer certification. Sections of length suitable for AFC-2 fuel specimens were cut from these original vendor stocks. Traceability of the cut sections to the original serialized cladding tube were maintained by re-serializing each new cut section and by logging the correspondence between the original tubes and cut sections. The traceability log was maintained in the Experiment As-Built Data Package.

Rodlet components were fabricated and inspected to be within the tolerances specified in the rodlet drawings mentioned earlier. This was all accomplished in INL machine shops.

The end plug-to-tubing joint of the fuel rodlet is considered to be a butt joint with integral backing, which conforms to a Category C joint on a Class 3 vessel per “ASME Boiler and Pressure Vessel Code,” Section III, ND-3351.3. The joint was fabricated as a Type 2 joint as required by ND-4243 and was fabricated to allow for 100% penetration. The welds for both ends of the AFC-2 rodlets were done in the AFCI glovebox using an ARC Machines Orbital welder. Figure 30 shows a cross-section micrograph of the cladding end plug weld. This micrograph was used as part of the package to qualify the weld process in the AFCI glovebox.

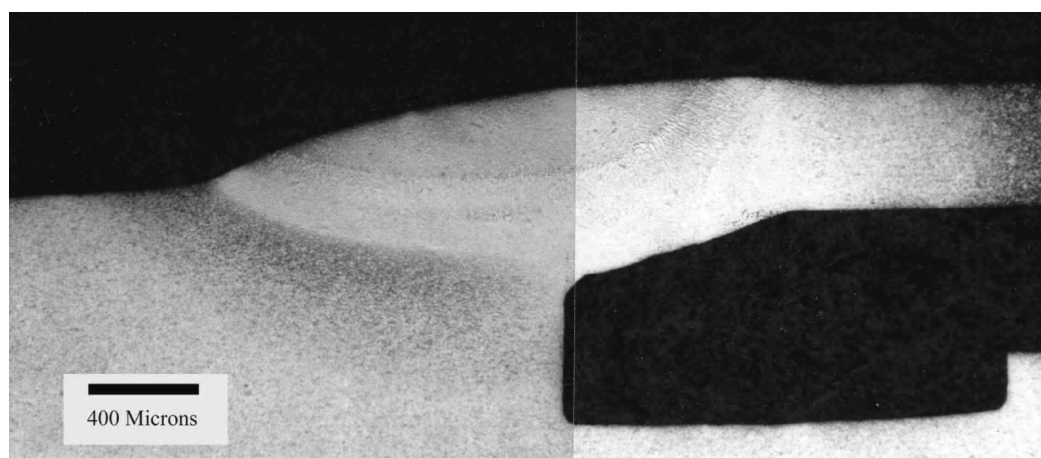


Figure 30. AFC-2 rodlet weld micrograph.

Data relating to weld qualification for each weld type are available for inspection from the AFC welding engineer. Weld inspection data for each weld, including the weld qualification package and process control specimen inspection data, was included in the AFC-2 As-Built Data Package.

The cladding tubes with the first end plug welded were weld inspected and leak checked to the requirements established in the fuels specification (Hyde 2007) and the “AFC-2 Fuel Rodlet and Capsule Final Inspection Plan,” PLN-2443 (Hyde 2008).

Jacket cleaning was done as needed to meet the requirements of the TFR fuels specification using the appropriate work request that, in effect, is a simple wipe down to make sure there is no contamination.

The sodium was loaded into the cladding jackets in the AFCI glovebox as specified in the fuel specification. The essential requirement is that the mass of the loaded sodium be 0.40 ± 0.01 gr and be documented in a Process Worksheet.

2.3 Rodlet Loading and Sealing

Rodlets were loaded and welded in an atmosphere of 70% argon and 30% helium. This was verified with a calibrated He analyzer that is integral to the “vac” atmosphere section of the AFCI glovebox. Figure 31 illustrates rodlet components.

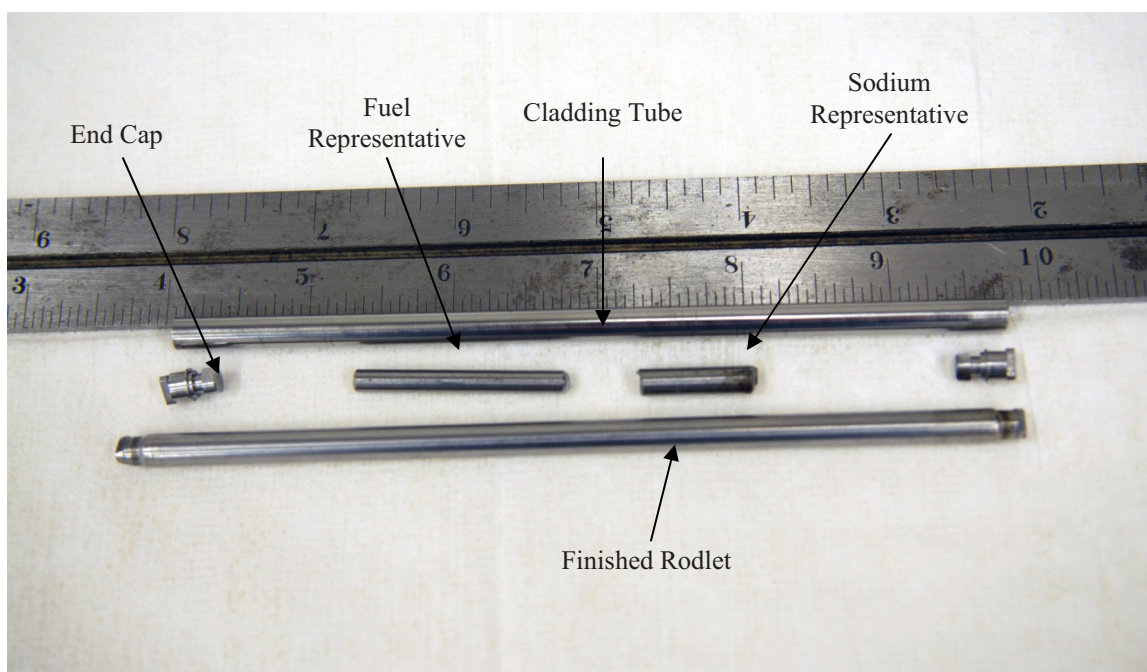


Figure 31. Rodlet components.

Finished fuel rodlets were subject to helium leak testing in accordance with the Inspection Plan (Hyde 2008).

Radiographic inspection was performed in accordance with the Inspection Plan (Hyde 2008). Radiographs for this inspection were included in the As-Built Data Package. Figure 32 shows an example of an x-ray weld inspection radiograph.

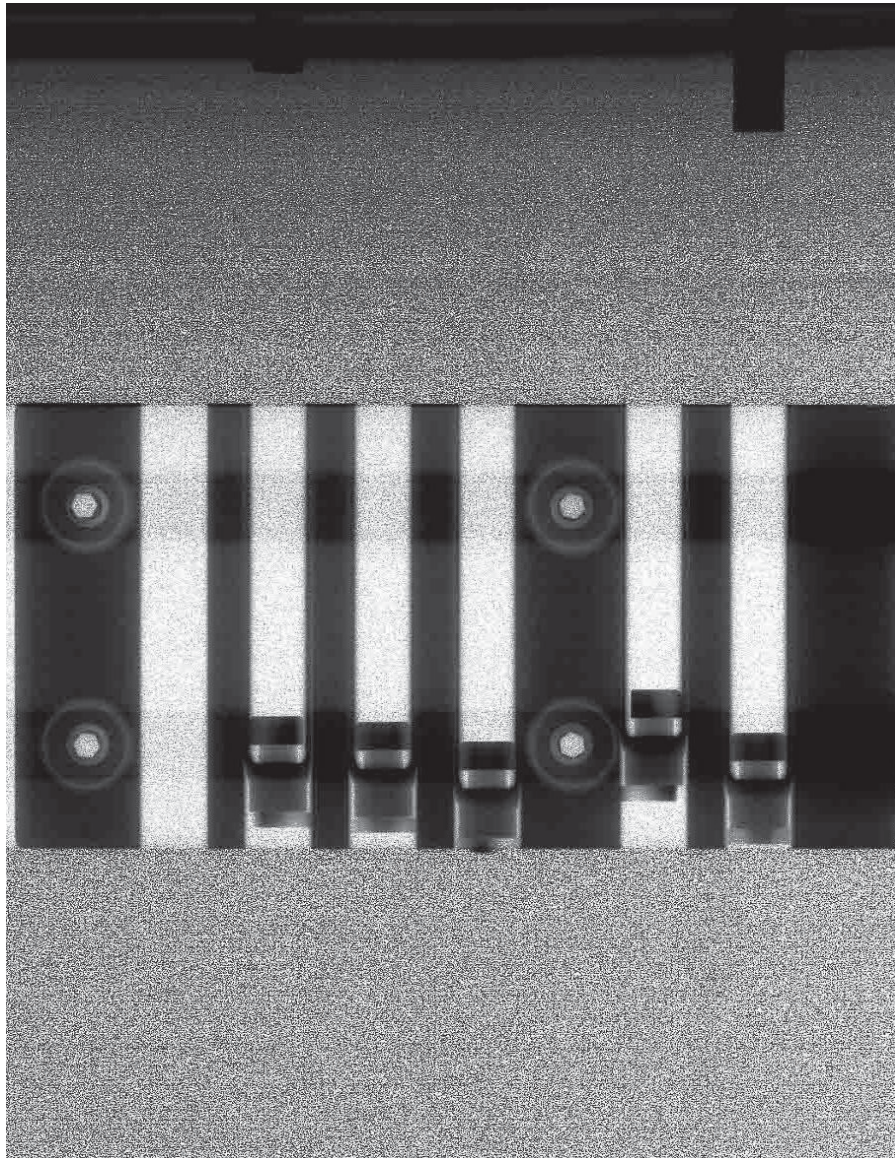


Figure 32. Rodlet closure weld radiograph.

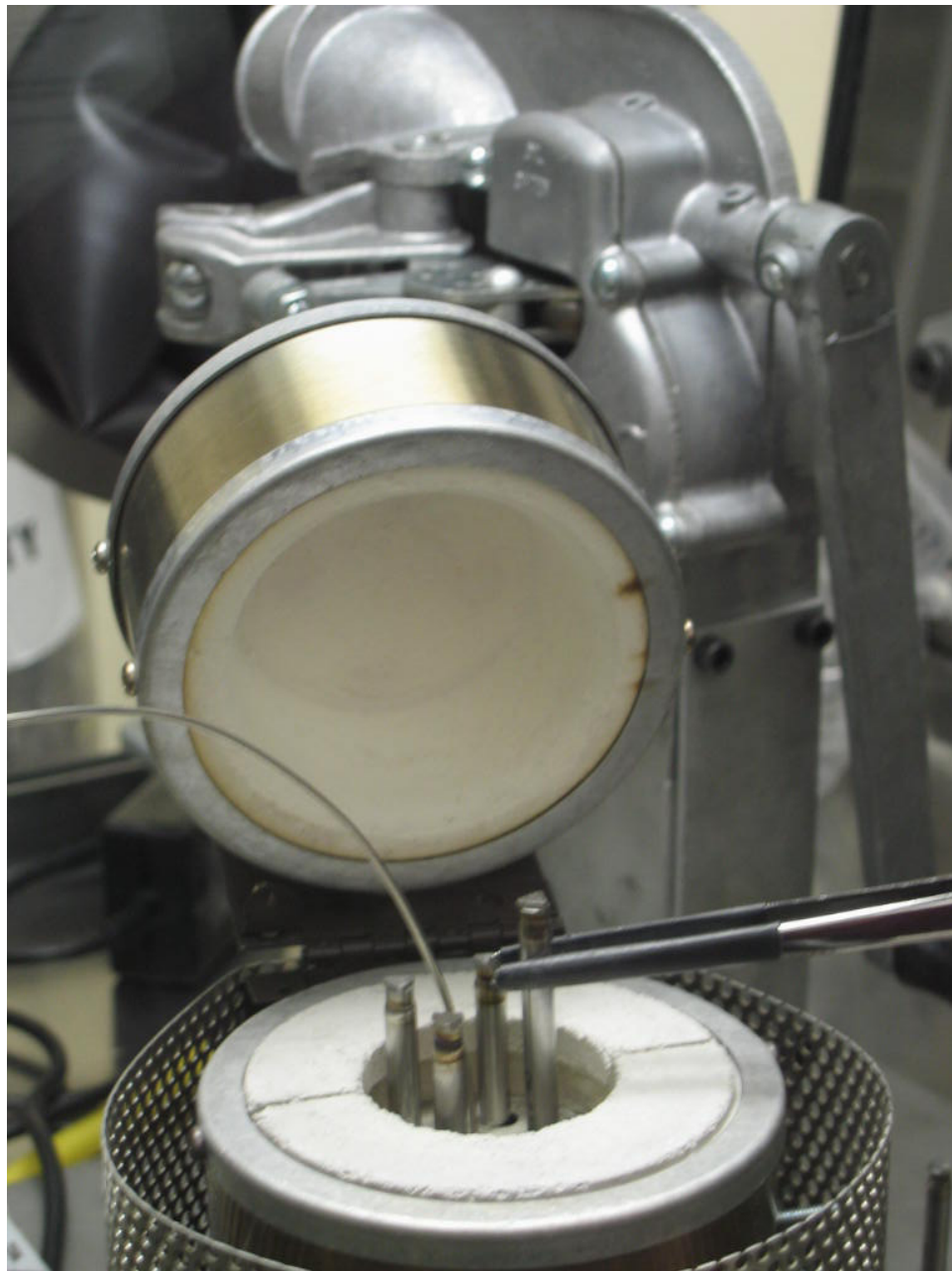


Figure 34. Settling and bonding furnace with four rodlets in place.



Figure 35. Copper chill block for cooling rodlets.

Radiographic inspection was performed to verify the integrity of the final product. The radiograph in Figure 36 shows an example of fuel and sodium positions and levels inside a sealed rodlet.

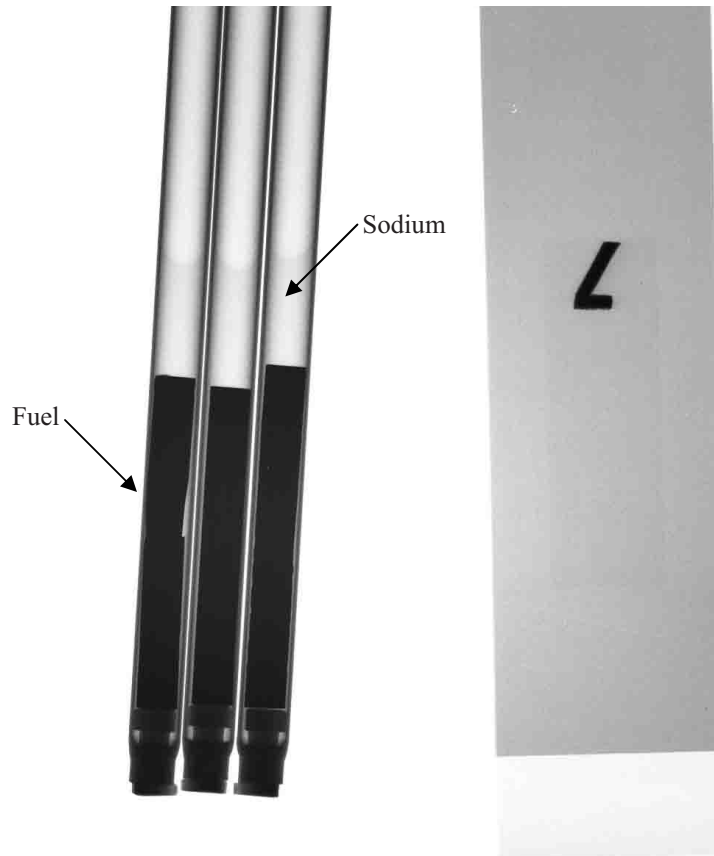


Figure 36. Rodlet radiograph showing fuel and sodium levels.

2.4 Capsule Fabrication

The following paragraphs describe the fabrication of the rodlet capsules.

The design drawings for the rodlet components are all documented and controlled. Capsule material was purchased to QA Level 1 to meet the specifications outlined in the controlled drawings. For the AFC-2A and 2B capsules, we used material purchased in the past for ATR experiments.

The containment vessel design was identical in both experiments. The experiment capsule is constructed to meet the intent of “ASME Section III, Class 1, Pressure Vessel Code,” and is considered to be Quality Assurance Level 1 fabrication.

Weld procedure specifications for the containment capsule top and bottom capsule closure welds are controlled using company procedures.

Two capsules were need to be fabricated, plus two equivalent shortened sections for welding controls. One of the two capsule tubes containing the fuel rodlets was etched AFC-2A and the other AFC-2B.

After the first end plug is welded on, it is radiographed and leak checked. Figure 37 shows a radiograph of a capsule end plug weld.

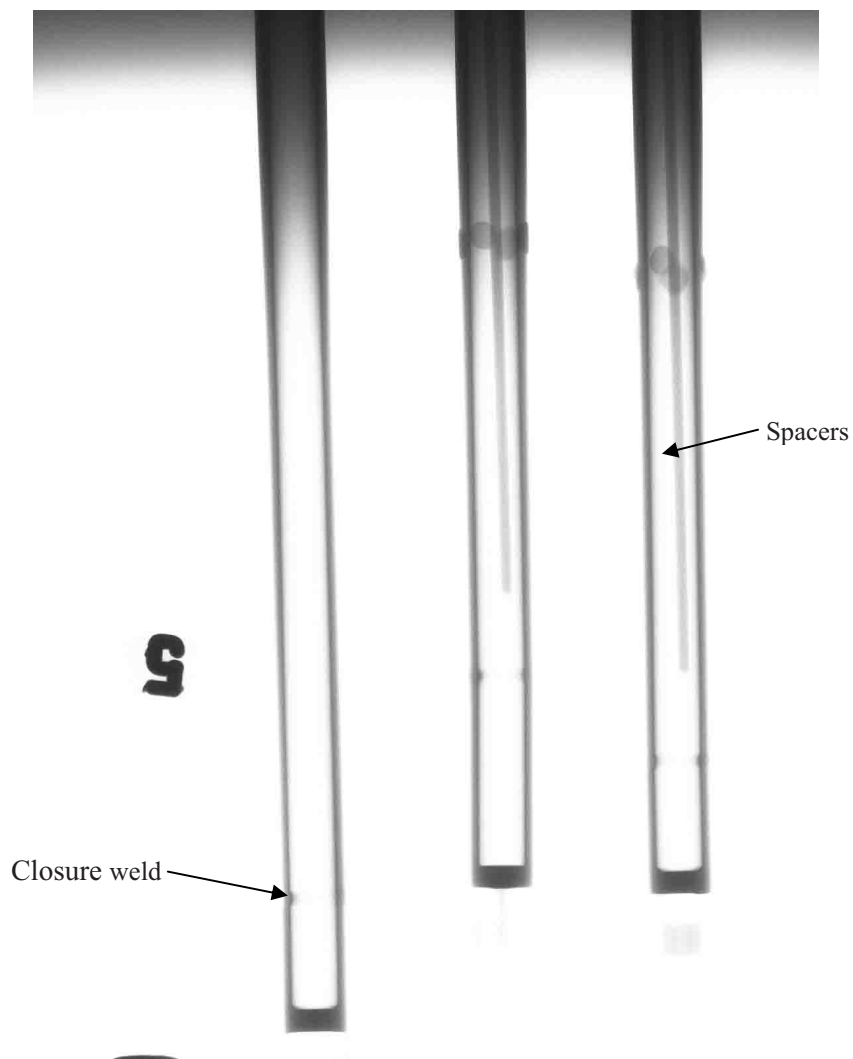


Figure 37. Capsule end plug radiograph.

Data relating to weld qualification for each weld type are available for inspection from the AFC welding engineer. Weld inspection data for each weld, including the weld qualification package and process control specimen inspection data, was included in the AFC-2 As-Built

Data Package(s). If a loaded capsule fails to meet the welding and leak rate standards, it could be re-welded once.

Lastly, the capsules are cleaned as needed to meet the requirements in the fuels specification using the appropriate work request. This is essentially a wipedown with an ethanol non-lint cloth.

2.5 Capsule Assembly

This section describes the loading of the rodlets into the capsule, capsule end plug welding, and the associated inspections. This section also includes the description of the As-Built Data Package required for ATR acceptance of the experiment.

Experiment assembly was conducted in accordance with procedure. Loading of the experiment stack was witnessed and verified as detailed in this procedure. The experiment containment capsule is filled with helium and welded inside a He-filled chamber in accordance with this procedure. Helium purity in the capsule is guaranteed through process knowledge, process qualification, and sampling of process control specimens. Gas process control specimens were collected before and after welding of each capsule. The helium gas content of all process control specimens was analyzed by mass spectrometry at the MFC Analytical Laboratory. The requirement is 99.5-100%.

Welding of the capsule top closure was in accordance with procedure. All welds made on process control specimens were non-destructively inspected and the documents referenced therein. Welds made on process control samples were destructively inspected to validate weld quality.

Capsule AFC-2A was loaded with the appropriate rodlets as follows in Table 8.

Table 8. Capsule AFC-2A.

Rodlet Order	Rodlet Designation	Fuel Designation
1- (Top)	AFC2A-R1	AFC2-A1
2	AFC2A-R2	AFC2-A2
3	AFC2A-R3	AFC2-A3
4	AFC2A-R4	AFC2-A4
5	AFC2A-R5	AFC2-A5
6- (Bottom)	AFC2A-R6	AFC2-A6

Capsule AFC-2B was loaded with the appropriate rodlets as follows in Table 9.

Table 9. Capsule AFC-2B.

Rodlet Position	Rodlet Designation	Fuel Designation
1-(Top)	AFC2B-R1	AFC2-A1
2	AFC2B-R2	AFC2-A2
3	AFC2-XX	AFC2-A3
4	AFC2B-R4	AFC2-A4
5	AFC2B-R5	AFC2-A5
6-(Bottom)	AFC2B-R6	AFC2-A6

Figures 38-43 show the capsule assembly process.



Figure 38. Etched capsules with spacer and end caps.



Figure 39. Verifying rodlet serial numbers and loading order.

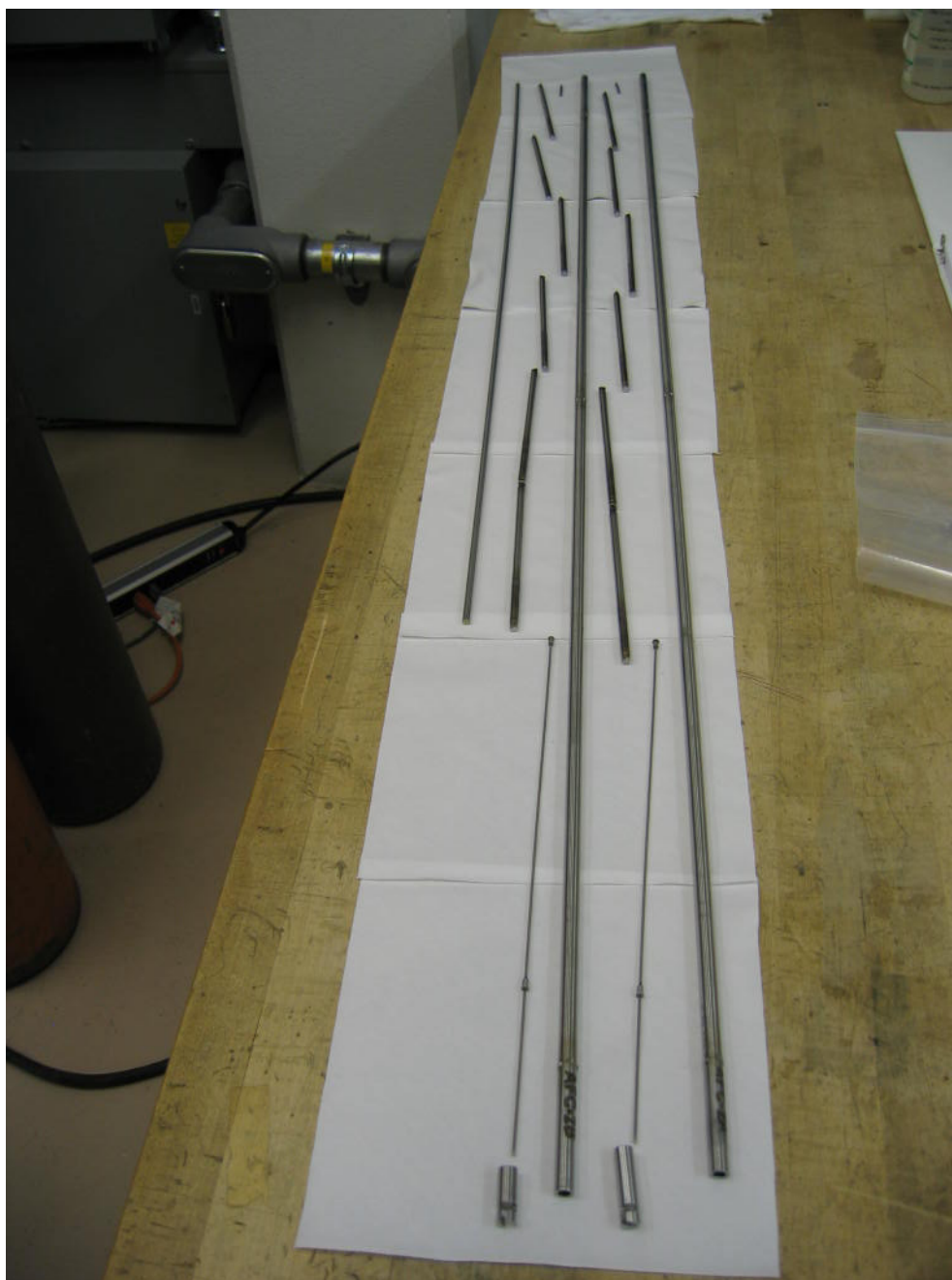


Figure 40. Rodlets and spacers laid out for loading into capsule. (The rod to the far left is a push rod for loading rodlets.)

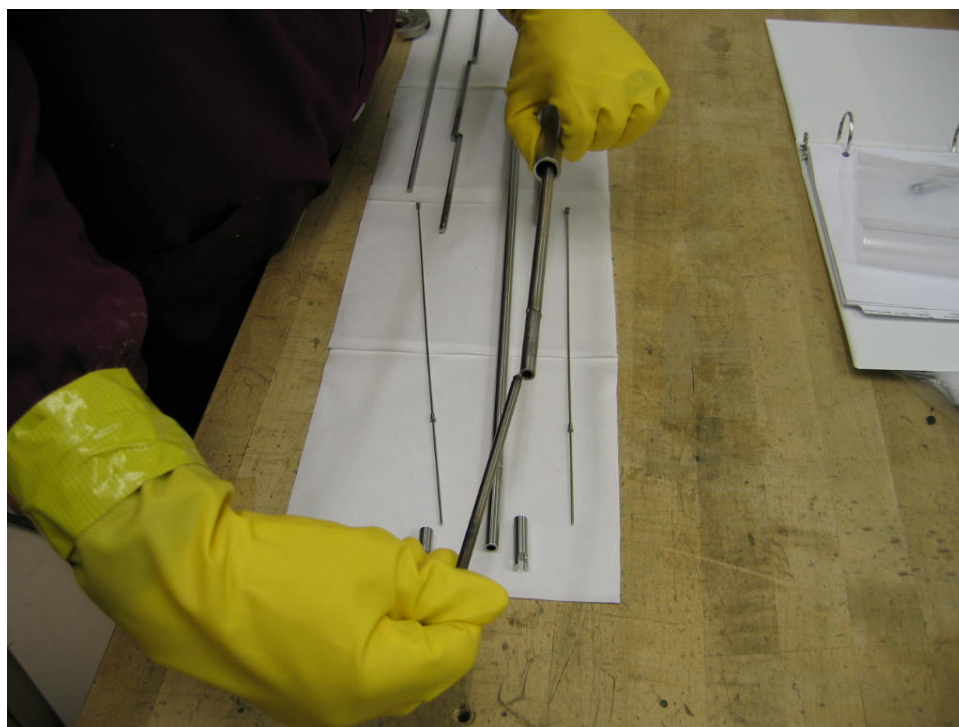


Figure 41. Inserting rodlet into capsule.

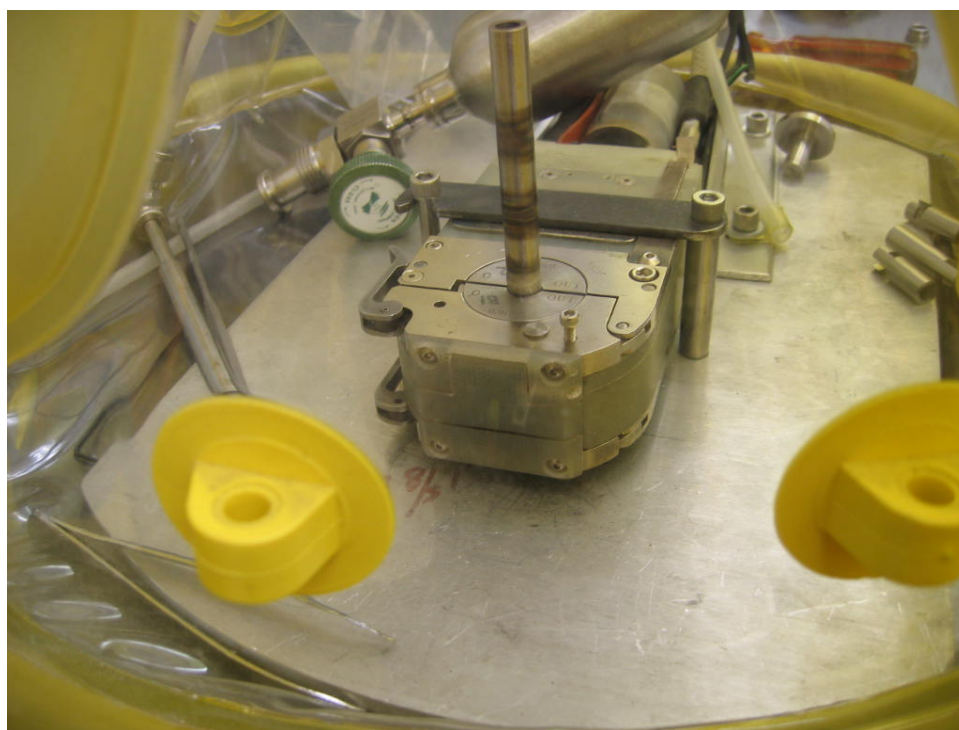


Figure 42. Orbital welding system for capsule closure inside a He glove bag with a test tube shown in place.



Figure 43. Inserting a loaded capsule into the orbital welding enclosure.

Finished capsules were subject to helium leak tests and radiographic inspection in accordance with the Inspection Plan (Hyde 2008). The radiograph in Figure 44 depicts a completed capsule showing a rodlet inside.

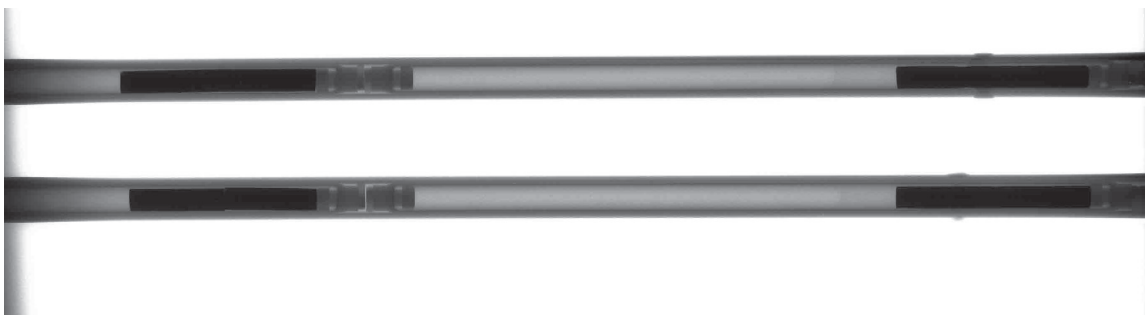


Figure 44. Capsule radiograph verifying rodlet position.

As-Built Fuel Rodlet Summary Data Sheets and Fuel Rodlet Summary Final Inspection Sheets were provided for each fuel rodlet (Hyde 2008). Requirements for these data sheets are called out in the fuel specification. As-built data sheets were provided for the assembled experiment capsules as detailed in Inspection Plan (Hyde 2008). A complete set of as-built drawings were provided for all component parts of this experiment and for the final assembled test capsule.

All fuel, cladding components, rodlets, capsule components, finished capsule assemblies, and irradiation hardware that do not meet the standards stated in the TFR fuel specification were reported via reporting procedure.

3. TMA EXPERIMENTAL RESULTS

Samples were cut from each alloy rod to be run in the Thermo-Mechanical Analyzer (TMA) to determine the coefficient of thermal expansion and to investigate phase transitions as a function of temperature. The instrument used to measure the thermal expansion was a Shimadzu TMA-50H. The instrument was calibrated by running a Platinum standard then doing a correction based on this curve to correct to the published Pt curve (Edsinger, Reilly and Schodey 1986). Pt standard runs are shown in Figure 45 below.

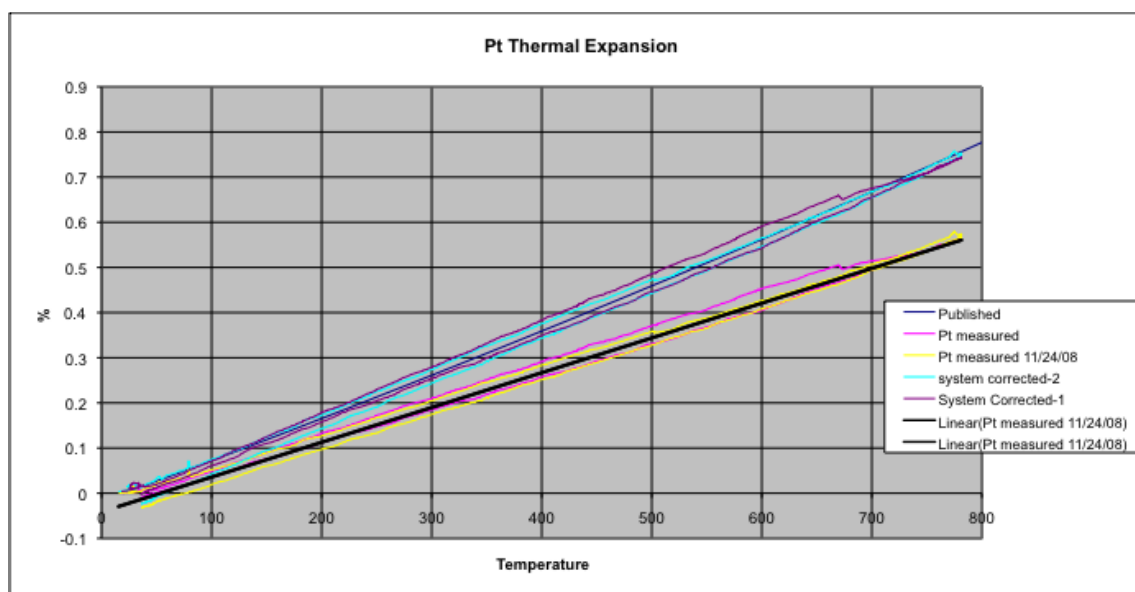


Figure 45. Pt Standard heating and cooling curves.

The system correction is a linear correction as a function of temperature. The correction is applied to the percentage expansion directly by adding 0.00023 times the measured temperature

to the measured percent expansion. System Corrected % Expansion= Measured % Expansion + $0.00023 \times \text{Temperature}$.

Figure 46 shows a fuel sample in the TMA. This picture was taken after a heating and cooling run. The measurement stylus has moved off center during the testing cycle. Most runs did not experience this movement. The ones that did, showed a distinct step function in the plotted data curve and were corrected or discarded. Note the two thermocouples on each side of the sample. One controls the temperature of the furnace and the other records the temperature of the sample.

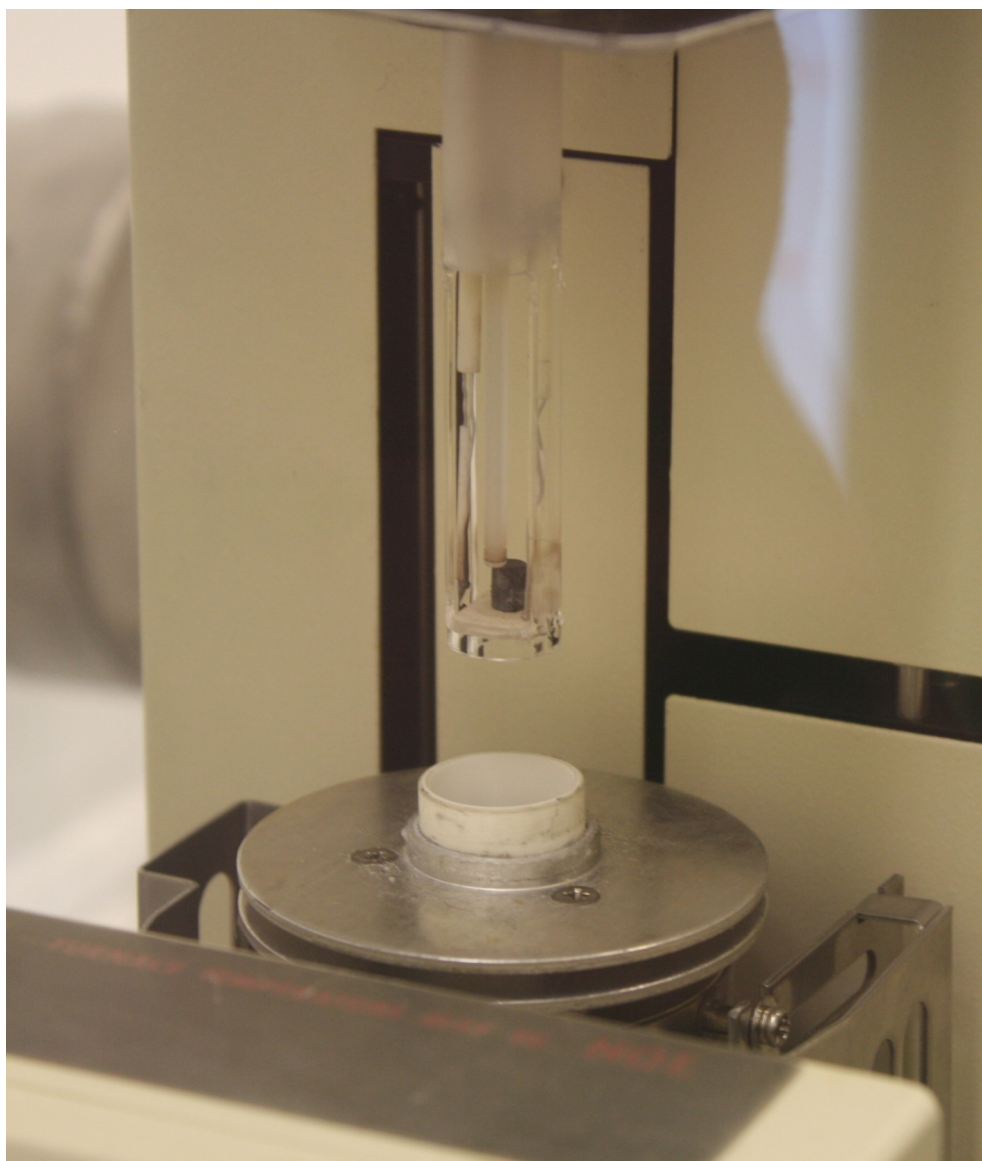


Figure 46. Open TMA showing sample.

As with all testing with minor actinide-containing materials, the TMA measurements are performed in a glovebox. Figure 47 shows the TMA inside its glovebox, just in front of the glove ports. The glovebox is used to contain radioactive contamination, but it makes working on and with delicate instruments difficult and cumbersome.



Figure 47. Tim Hyde working with the TMA in the glovebox.

Each run went from ambient temperature to 800°C with a ramp rate of 3°C per min. Each sample was run repeatedly in an attempt to obtain a steady state curve.

- 60U-20Pu-3Am-2Np-15Zr (A1)

The TMA 60U-20Pu-3Am-2Np-15Zr (A1) sample was cycled three times. The third run did show evidence of surface oxidation. Figure 48 shows these runs with the expansion zeroed from the start of the heating cycle. This alloy sample was one of the less repeatable samples and did demonstrate some probe movement during the cycle runs.

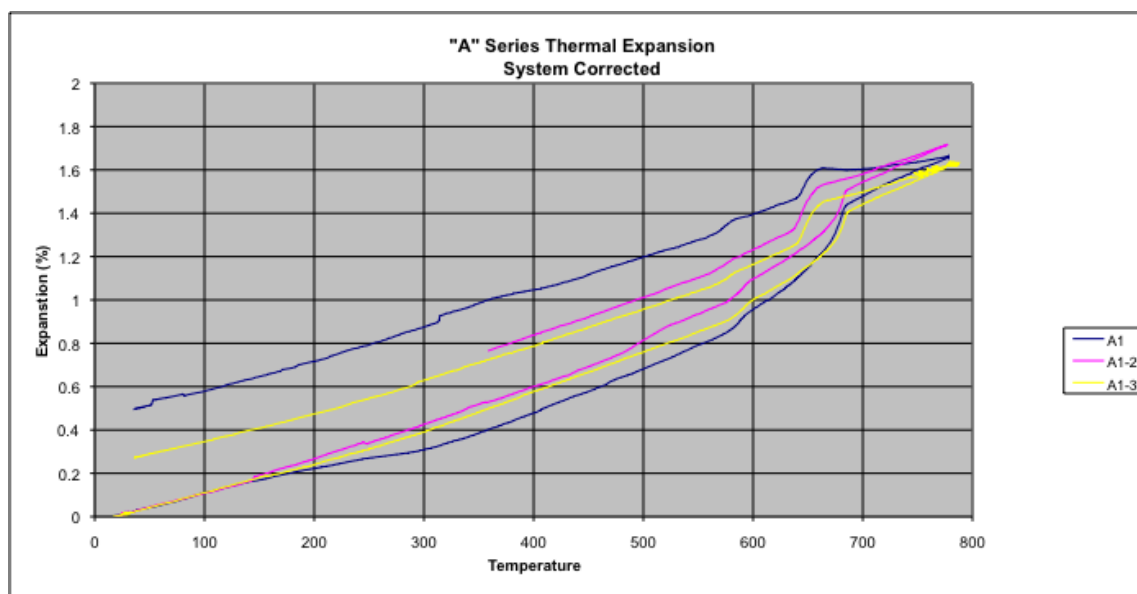


Figure 48. 60U-20Pu-3Am-2Np-15Zr (A1) TMA heating and cooling curves.

During heating, the alloy shows a phase transformation at 587°C and another at 680°C.

During cooling, the phase transitions are at 640°C and then again at 575°C.

- 59U-20Pu-3Am-2Np-1RE-15Zr (A2)

The TMA 59U-20Pu-3Am-2Np-1RE-15Zr (A2) sample was cycled two times. This sample showed good repeatability. The curves are shown in Figure 49 and are zeroed on cooling.

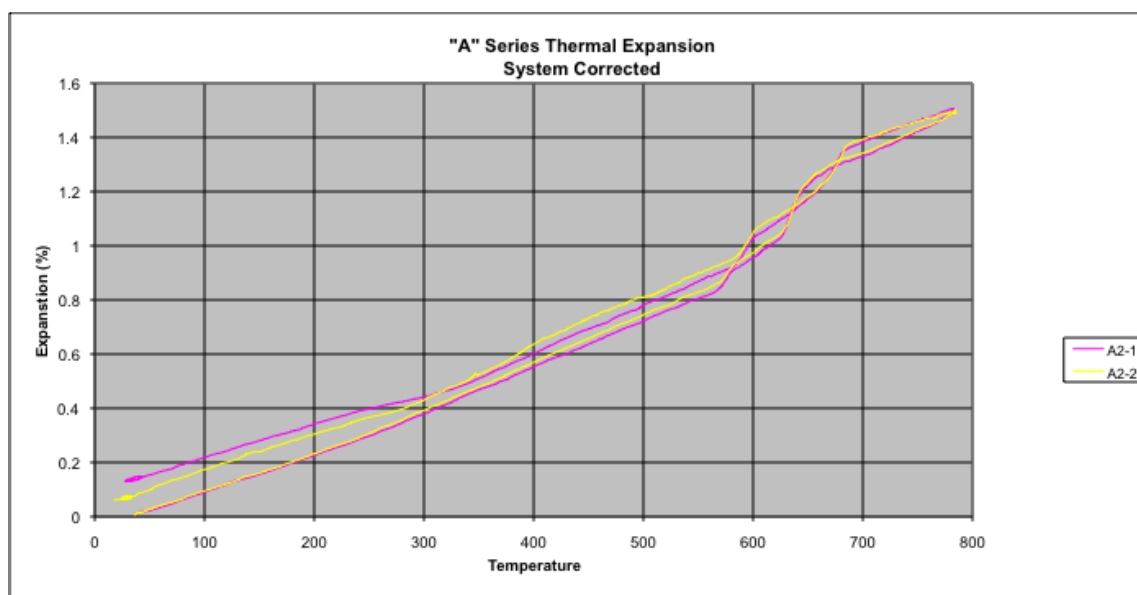


Figure 49. 59U-20Pu-3Am-2Np-1RE-15Zr (A2) TMA heating and cooling curves.

This alloy shows a more significant lower temperature phase change at 595°C on heating and then at 570°C on cooling. The higher temperature phase change is at 680°C on heating and then 630°C on cooling.

- 58.5U-20Pu-3Am-2Np-1.5RE-15Zr (A3)

The TMA 58.5U-20Pu-3Am-2Np-1.5RE-15Zr (A3) sample was cycled three times. Figure 50 shows these runs with the expansion zeroed from the end of the cooling cycle. This was done because of the apparent mechanical movement during the heating cycle.

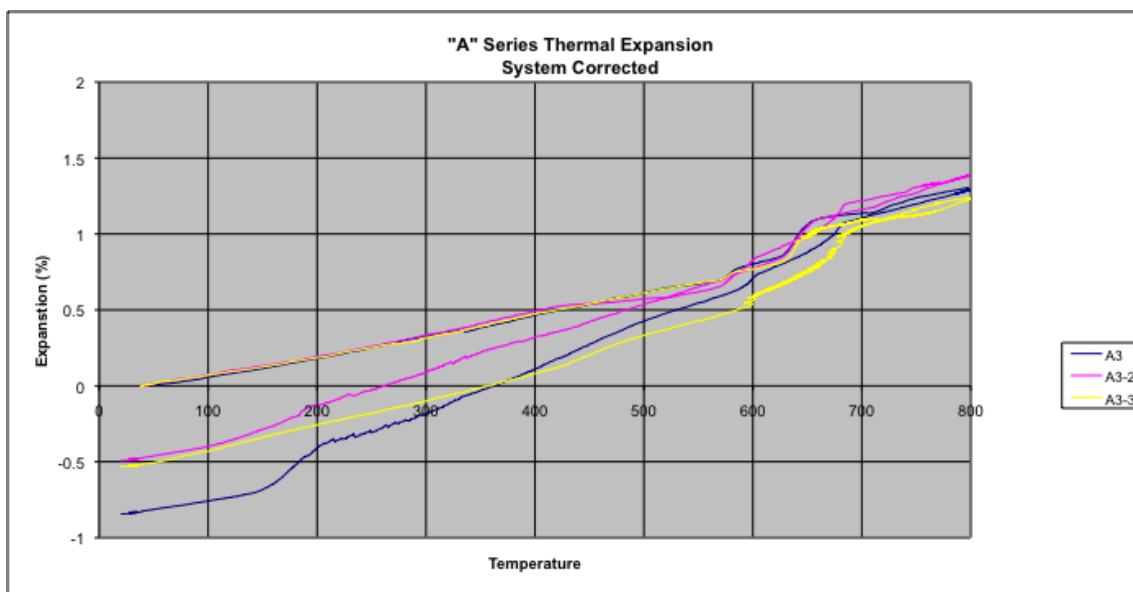


Figure 50. 58.5U-20Pu-3Am-2Np-1.5RE-15Zr (A3) TMA heating and cooling curves.

This alloy shows a phase transition at 595°C on heating and then at 575°C on cooling. The higher temperature transition is fairly short on heating and occurs at 680°C. This transition is broader on cooling and occurs between 650°C and 525°C.

- 40.5U-30Pu-5Am-3Np-1.5RE-20Zr (A4)

The TMA 40.5U-30Pu-5Am-3Np-1.5RE-20Zr (A4) sample was cycled only once. Figure 51 shows these runs with the expansion zeroed from the start of the heating cycle. This alloy showed a repeatable heating and cooling curve so it was not re-run because of time constraints.

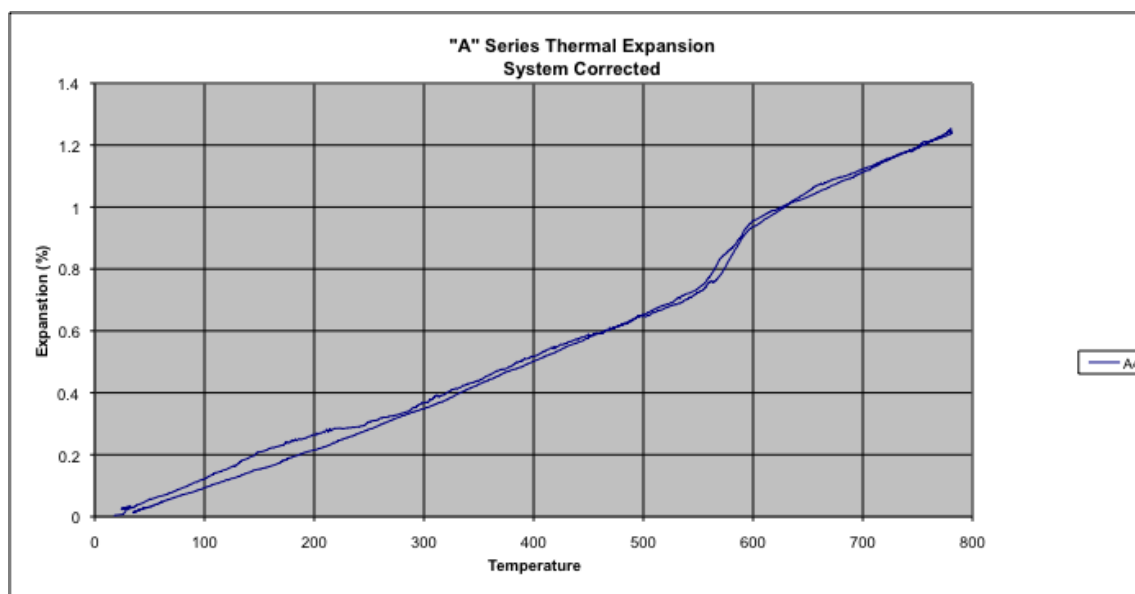


Figure 51. 40.5U-30Pu-5Am-3Np-1.5RE-20Zr (A4) TMA heating and cooling curves.

This alloy shows only one significant phase transition. This transition occurs between 570°C and 595°C on heating and then between 575°C and 560°C on cooling. There is a change in slope on heating around 650°C. Given the data from other techniques this could be a weak indication of a phase change.

- 41U-30Pu-5Am-3Np-1RE-20Zr (A5)

The TMA 41U-30Pu-5Am-3Np-1RE-20Zr (A5) sample was cycled two times. The data acquisition system failed on the first cooling cycle so the sample was run again. Figure 52 shows these runs with the expansion zeroed from the start of the heating cycle. This alloy also demonstrates good repeatability and no homogenization changes.

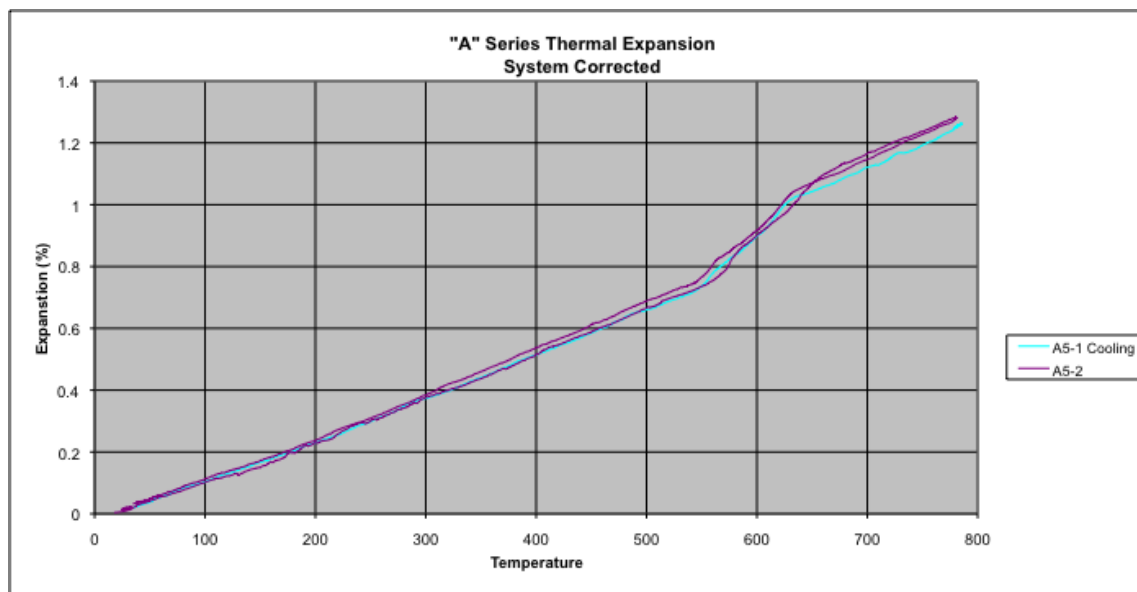


Figure 52. 41U-30Pu-5Am-3Np-1RE-20Zr (A5) TMA heating and cooling curves.

This alloy again shows two phase transitions. The lower temperature phase change occurs at 570°C on heating and then at 550°C on cooling. The higher temperature phase occurs at 650°C on heating and then at 625°C on cooling.

- 42U-30Pu-5Am-3Np-20Zr (A6)

The TMA 42U-30Pu-5Am-3Np-20Zr (A6) sample was cycled three times. Figure 53 shows these runs with the expansion zeroed from the start of the heating cycle. This alloy sample was one of the more repeatable samples and did demonstrate the system is clean and functioning properly.

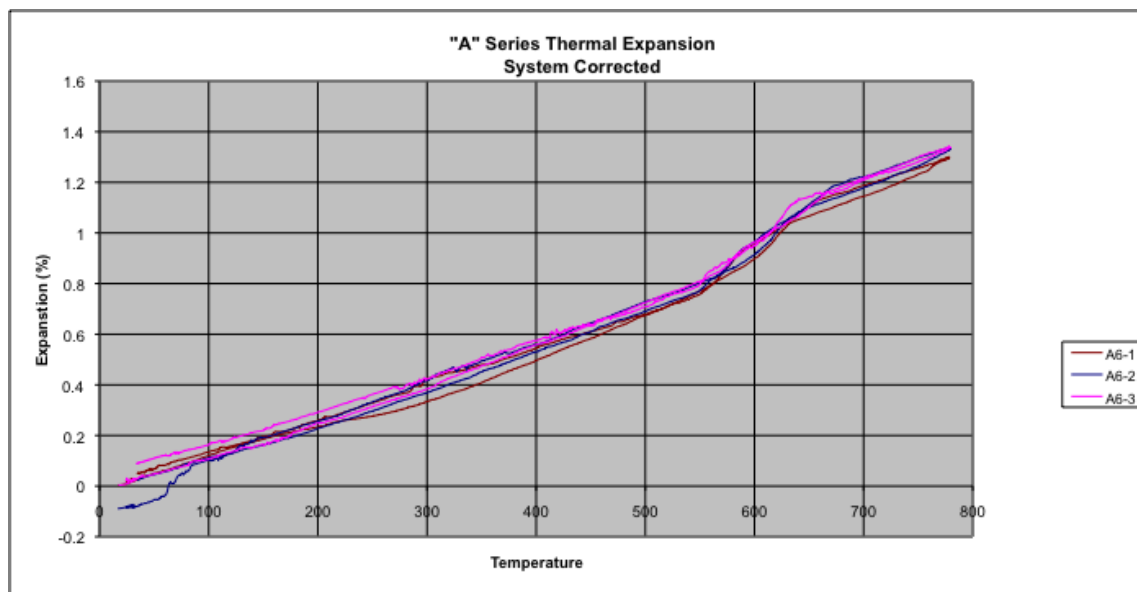


Figure 53. ^{42}U - ^{30}Pu - 5Am - 3Np - 20Zr (A6) TMA heating and cooling curves.

This alloy shows two phase changes, with the lower temperature change not having a dramatic change on the thermal expansion and occurring between 550°C and 575°C , on both heating and cooling. The higher temperature phase change occurs at 670°C on heating and then 620°C on cooling.

Figure 54 shows the complete series of thermal expansion curves. All of the alloys show very similar expansion characteristics, a transition around 560°C , and another at about 650°C . This result is promising, in that all of the elemental additions to the alloys do not seem to change the basic fundamental phases. There are two primary reasons this is good: (1) that the starting fuel can tolerate significant rare earth residuals from pyroprocessing, and (2) that the fuel will be less likely to experience major phase changes as fission products build up in the fuel during irradiation.

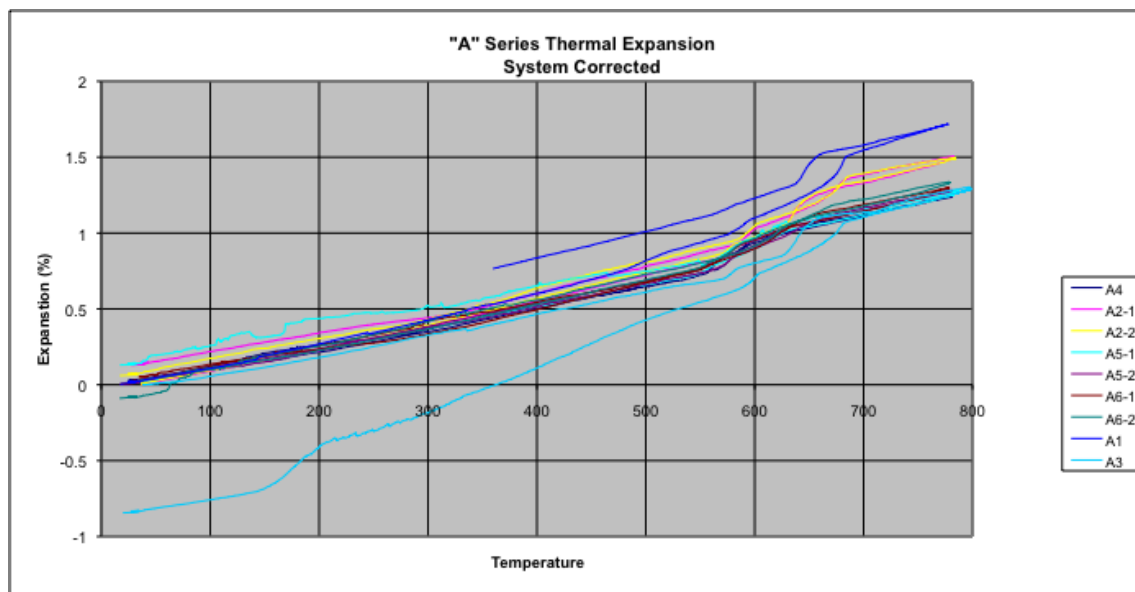


Figure 54. “A” series thermal expansion.

4. DISCUSSION

Extensive characterization of the fuel alloys was performed by others within the INL (I performed or supervised all previous work in this thesis). This analysis is presented here and is used to validate and discuss the TMA results. In addition, this analysis shows a more complete picture of the experimental fuel’s phase and thermo-physical properties.

4.1 Scanning Electron Microscopy

Samples from each alloy were mounted and polished for metallographic and SEM analysis. Transverse sectioned samples were cut from the as-cast fuel slugs using a slow speed Buehler saw in an air glovebox. All prepared SEM samples were nominally 4.3 mm in diameter and cut to 1-2 mm widths. Little state of the art metallography preparation equipment is available for use on minor actinide-containing materials. As a result, all preparation was done in a glovebox using hand polishing techniques. As a result, the surfaces to be examined are quite rough. The SEM is used for grain size analysis and phase composition analysis using the Energy Dispersive X-ray (EDX) capability.

Microstructural characterization was performed using the Zeiss 960A SEM in the Electron Microscopy Laboratory (EML) at the INL Materials and Fuels Complex (MFC). The microscope is equipped with an Oxford Link Petafet energy-dispersive x-ray (EDX) detector and an Oxford Microspec WDX 600 wavelength-dispersive x-ray (WDX) spectrometer. Low-magnification

images showing the entire samples were recorded as 4×5 in. Polaroid images (Polaplan 52 film) and scanned. The remaining images, and all spectra, were collected and recorded using ISIS Suite Revision 3.2 software. All chemical analyses used a working distance of 25 mm, optimal for both the EDX and WDX spectrometers. Secondary electron (SE) and backscattered electron (BSE) images were taken to study and document the microstructures, and EDX spectroscopy was used to perform qualitative chemical analyses. X-ray maps were obtained by using the WDX spectrometer to show spatial distributions of elements. The samples were sputter coated with a thin layer of Pd before examination to reduce charging from the electron beam (Janney and Kennedy 2010; Kennedy and Janney 2007; Kennedy et al. 2008; Kennedy et al. August 2008).

- 60U-20Pu-3Am-2Np-15Zr (A1)

Two samples from the 60U-20Pu-3Am-2Np-15Zr (A1) composition were examined, each from a separate casting. Figure 55 shows low-magnification images of the AFC2-A1-79-SEM1 and AFC2-A1-80-2-SEM1 samples in which the samples appear similar. The porosity in the samples occurs as widely-spaced round holes and smaller, irregular voids. Neither of these types of porosity has any discernible influence on the microstructure of the adjacent material.

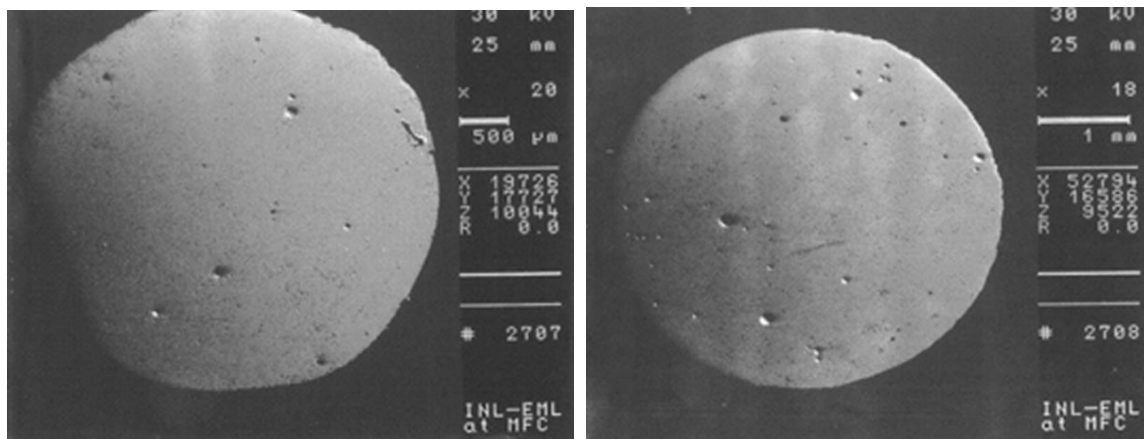


Figure 55. Low-magnification images of the 60U-20Pu-3Am-2Np-15Zr (A1) casting samples, AFC2-A1-79-SEM1 (top) and AFC2-A1-80-2-SEM1 (bottom).

Figure 56 shows a higher magnification SE image of the fuel around one of the larger pores. The microstructure consists of two phases: a matrix phase, which appears light-colored in SE images, and an inclusion phase, which appears darker in both SE and BSE images (Figures 56 and 57). Backscattered electron images (see Figure 57) show that both a light and a dark

contrast phases exist in the matrix phase resulting from gradual variations. This likely indicates compositional gradients within this phase.

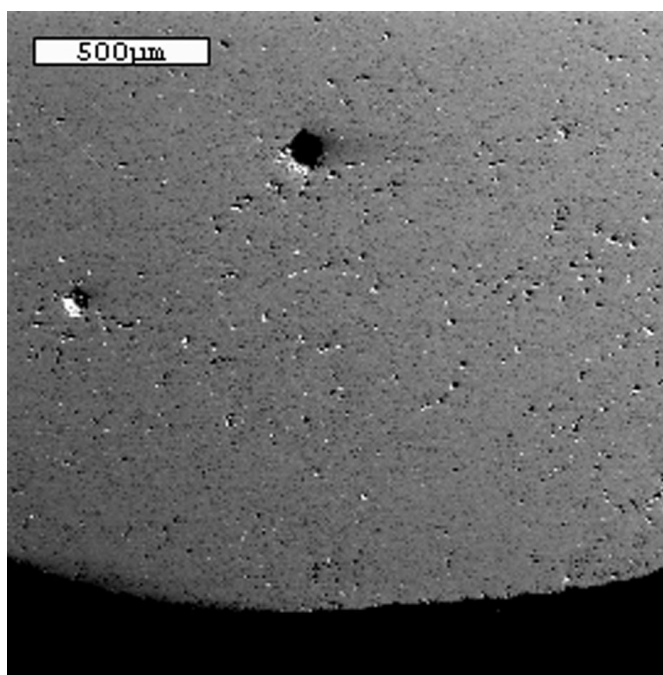


Figure 56. Secondary electron image of the 60U-20Pu-3Am-2Np-15Zr (A1) sample AFC2-A1-79-SEM1. Large dark areas in center and at left are internal porosity. Smaller dark areas are inclusions.

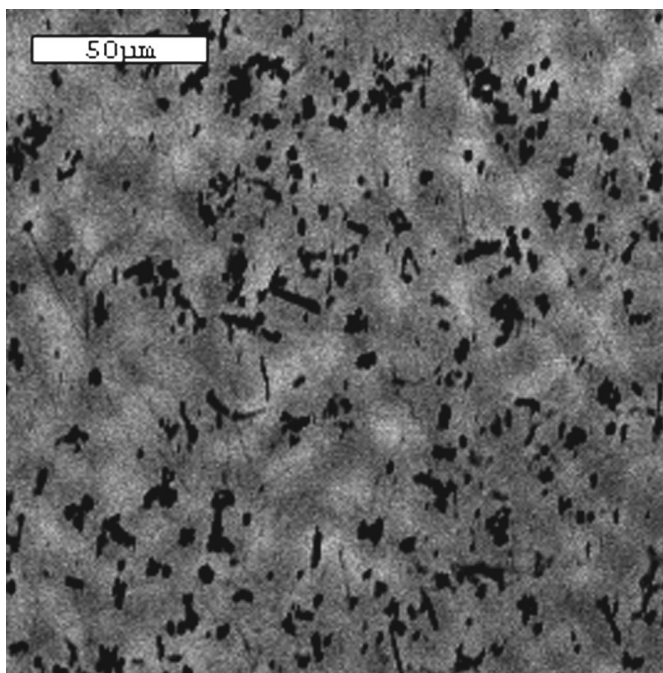


Figure 57. Higher magnification BSE image of the 60U-20Pu-3Am-2Np-15Zr (A1) sample AFC2-A1-79-SEM1.

The 60U-20Pu-3Am-2Np-15Zr (A1) inclusions appear as long slender dendrites, closely spaced clusters of small individuals, and others appear globular (see Figures 58 and 59). The maximum observed lengths of the elongated inclusions are $\sim 50\text{ }\mu\text{m}$, and some globular inclusions are approximately $20\text{ }\mu\text{m}$ across. No systematic variations related to distance from the edges of the samples were observed.

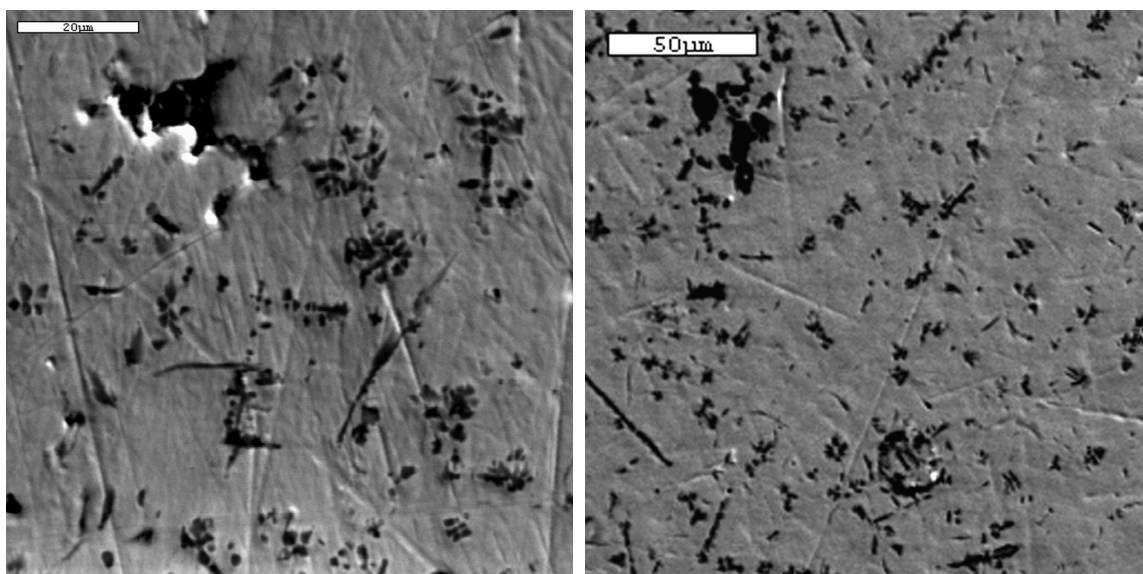


Figure 58. Secondary electron (SE) images of the 60U-20Pu-3Am-2Np-15Zr (A1) samples, AFC2-A1-79-SEM1 (top) and AFC2-A1-80-2-SEM1 (bottom).

Figure 59 shows the representative x-ray maps obtained from the AFC2-A1-80-2-SEM1 sample. The inclusions are enriched in Zr and depleted in the actinides while the matrix is enriched in the actinides. A few inclusions are enriched in Si; likely they are particles of the silicon carbide abrasive used in sample preparation that became embedded in the sample surface. The x-ray maps indicate a fairly even distribution of Pu, Am, and Np throughout the matrix phase but some gradual variation in uranium. No grain boundaries can be resolved.

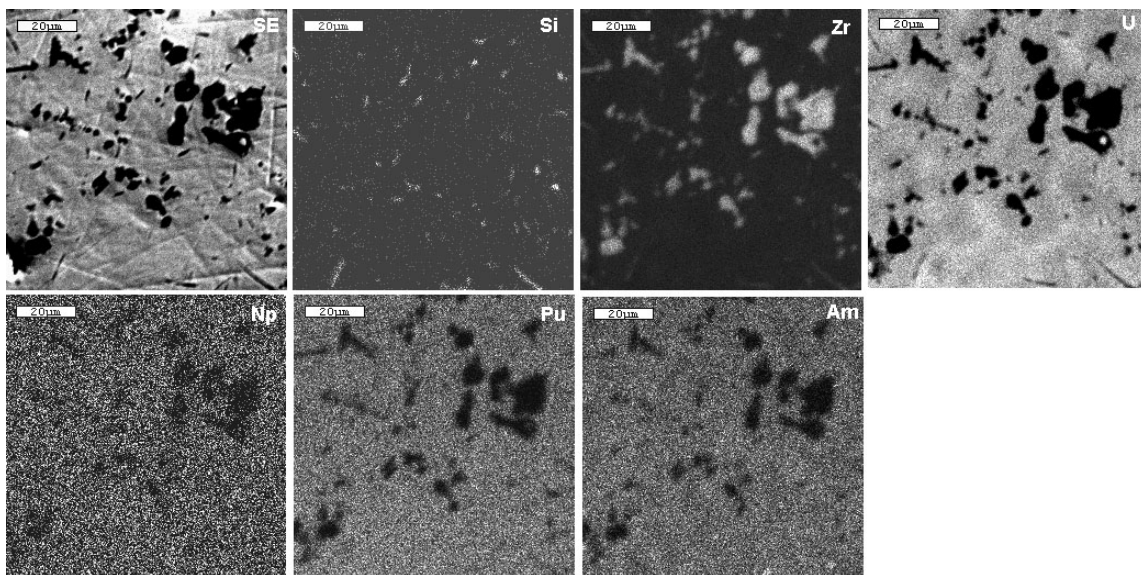


Figure 59. X-ray maps of the 60U-20Pu-3Am-2Np-15Zr (A1) sample, AFC2-60U-20Pu-3Am-2Np-15Zr (A1)-80-2-SEM1.

The available data from the SEM microstructural analysis on the 60U-20Pu-3Am-2Np-15Zr (A1) composition sample suggest that the sample consists of two phases:

1. High Zr content inclusions are low in actinides. Zr inclusions are similar to those seen in similar U-19.3wt%Pu-14.5wt% Zr, three component alloys (Leibowitz, Veleckis, and Blomquist 1988);
 2. A matrix, which is higher than the inclusions in the actinides.
- 59U-20Pu-3Am-2Np-1RE-15Zr (A2)

Figure 60 shows a low-magnification Polaroid image of the entire sample. The numbers in Figure 60 indicate areas selected for detailed analysis. All data from the interior of the sample were similar and suggested that the interior of the sample was homogeneous.

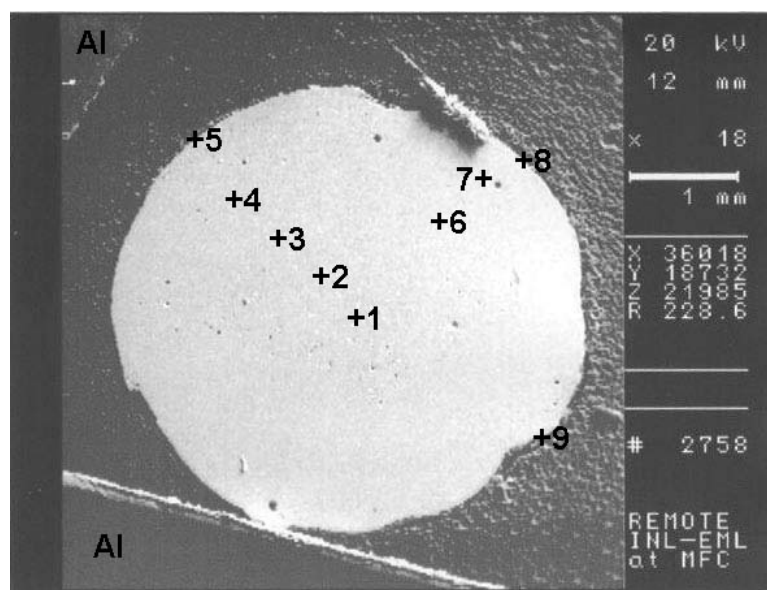


Figure 60. Low-magnification image showing the entire 59U-20Pu-3Am-2Np-1RE-15Zr (A2) sample. Al indicates aluminum tape.

Figure 61 is a compilation of BSE and SE images showing the microstructure of the sample from the center to the edge. The pores are irregularly distributed, but show no apparent differences between the edges and interior areas of the sample. Near the edge of the sample, inclusions formed perpendicular to the edge. Smaller inclusions and areas with patchy contrast appear uniform in size and shape throughout the sample.

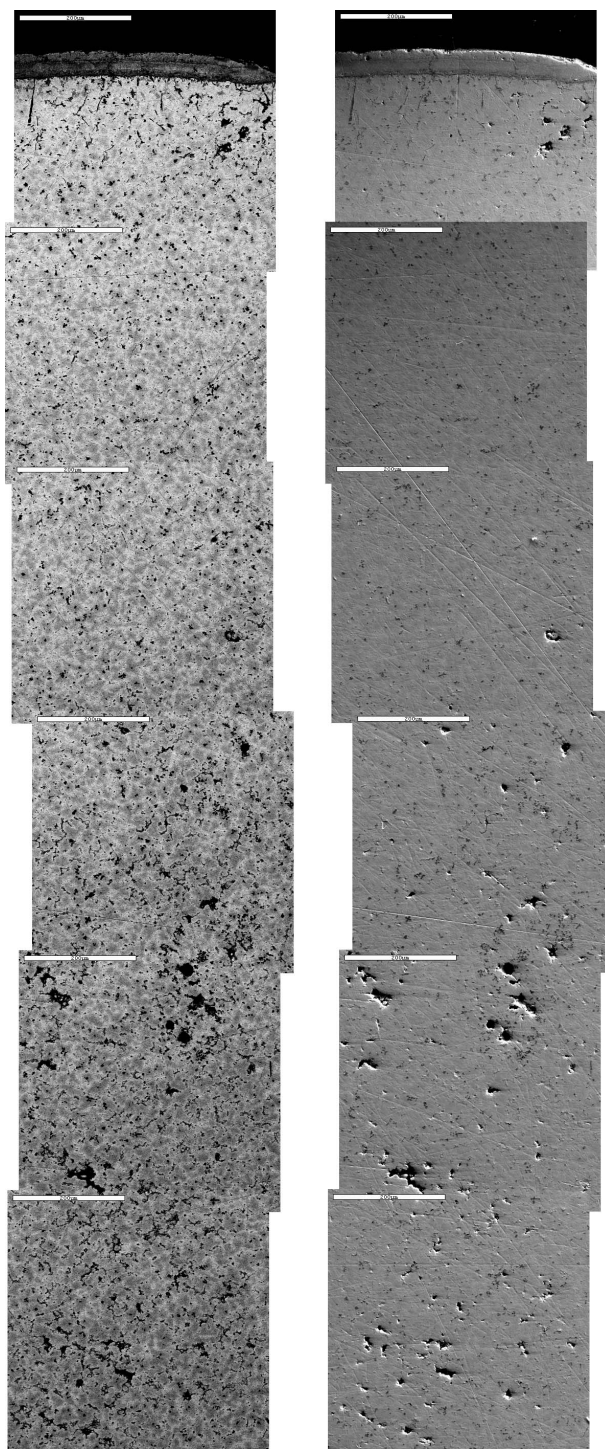


Figure 61. BSE and SE compiled images show microstructure of 59U-20Pu-3Am-2Np-1RE-15Zr (A2) sample from center to edge. Scale bars are 200 μm .

Figure 62 shows SE, BSE, and WDX x-ray maps from the interior of the 59U-20Pu-3Am-2Np-1RE-15Zr (A2) sample. Bright areas in the oxygen map in Figure 62 correspond to surface irregularities visible in the SE images and probably indicate small amounts of high-oxygen surface contaminant that occurred during sample preparation. Bright areas in the Zr map (see Figure 62) correspond to some of the dark inclusions observed in the BSE and SE images, and bright areas in the Ln (RE) maps correspond to the remaining dark inclusions. These observations suggest there are two kinds of inclusions: one that is high in Zr and lower in RE, and one that is high in RE. The two kinds of inclusions can be distinguished in SE and low-contrast BSE images because the high Zr content inclusions appear significantly darker than the high RE content inclusions. Both types of inclusions are lower in U and Pu than the surrounding matrix. Am has a distinctly different distribution from the other actinides, and all bright areas in the Am map correspond to high RE content inclusions, although the reverse is not true (i.e., some high RE content inclusions apparently do not have higher Am concentrations than the surrounding matrix). It is not unexpected that the RE elements and some of the actinides would behave similarly (Ward 1986).

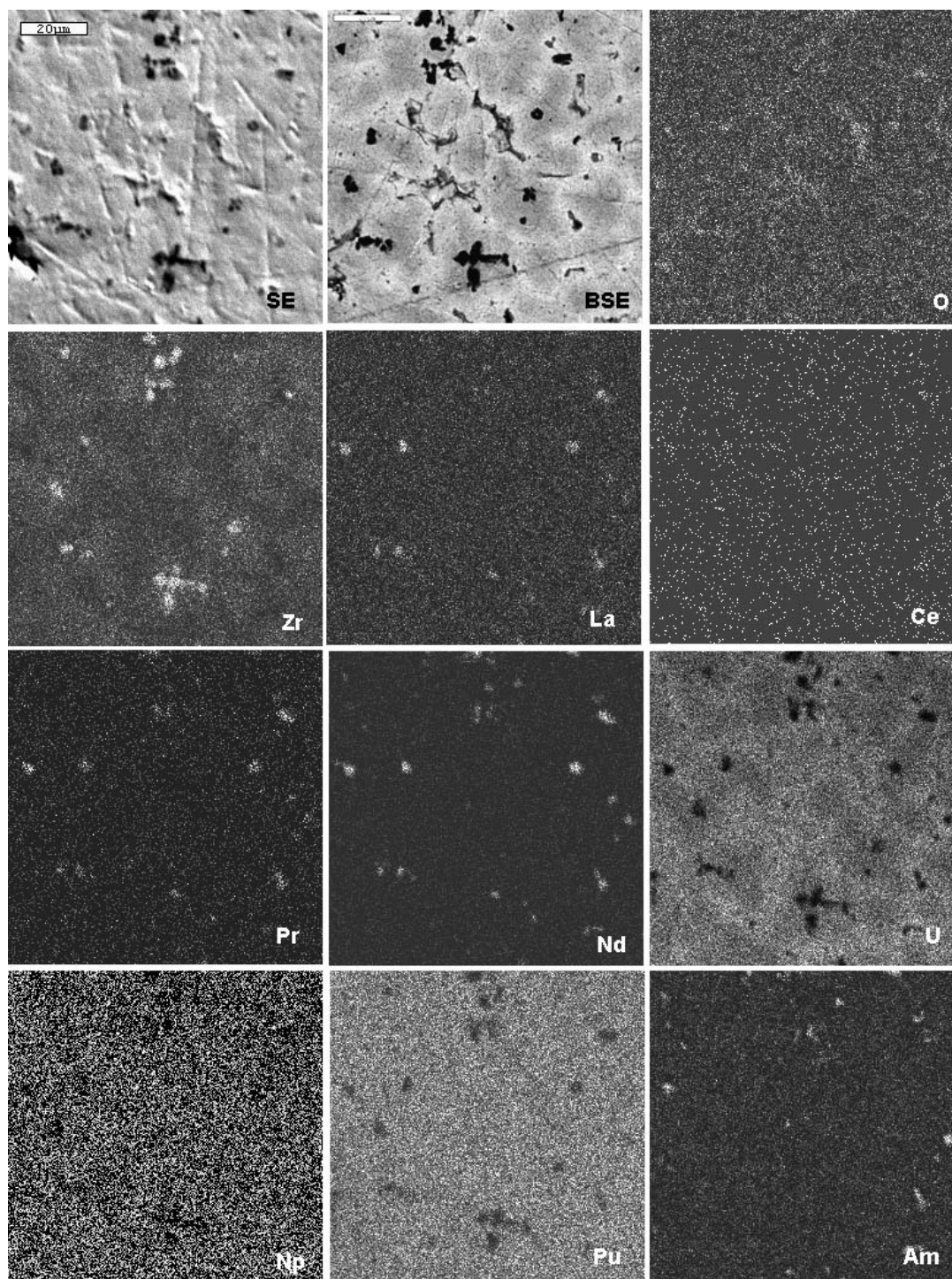


Figure 62. SE, BSE and WDX x-ray maps from the interior of the ^{59}U - ^{20}Pu - 3Am - 2Np - 1RE - 15Zr (A2) sample.

Figure 63 displays an SE image and x-ray maps at higher magnification obtained from the center area of the sample. This map confirms that all areas that are high in Am are also high in Nd, but that some Nd inclusions are not high in Am.

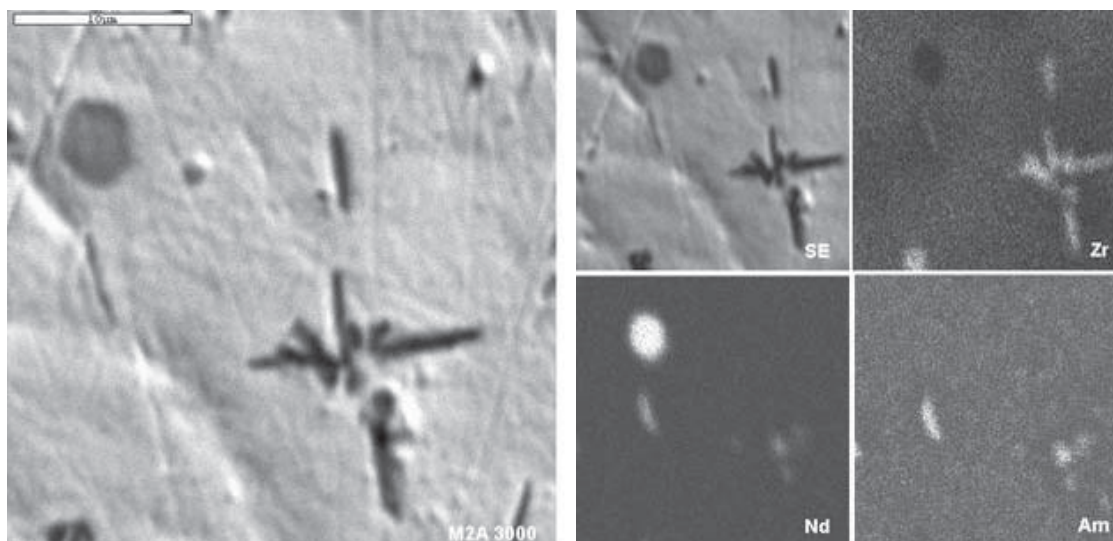


Figure 63. Higher-magnification images of internal area of the ^{59}U - ^{20}Pu - 3Am - 2Np - 1RE - 15Zr (A2) fuel sample: on left, larger SE image; on right, WDX x-ray maps using the Zr $L\alpha$, Nd $L\alpha$, and Am $M\beta$ x-rays.

Figure 64 shows x-ray maps from the rind at the edge of the specimen. The data in Figure 64 were collected at an accelerating voltage of 30 kV.

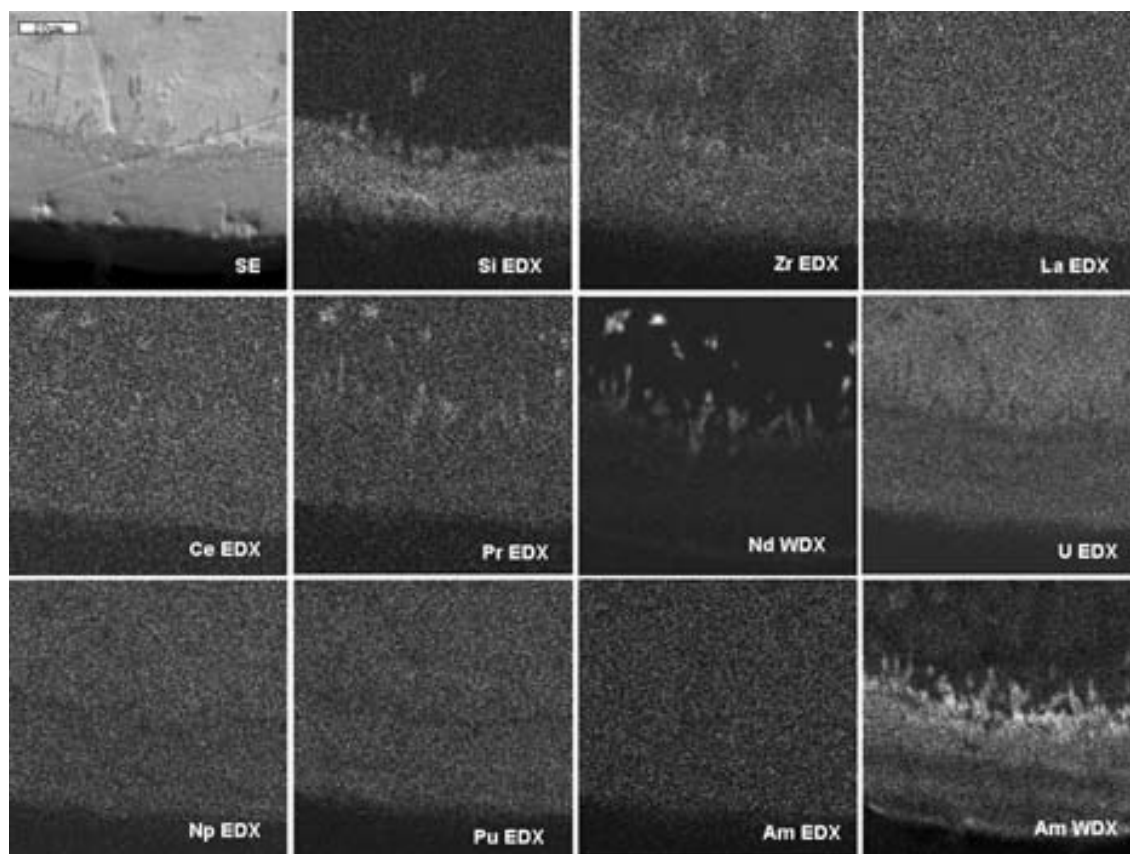


Figure 64. X-ray maps from the rim region. EDX maps used the Zr $K\alpha$, La $L\alpha$, U $L\alpha$, Np $L\alpha$, Pu $L\alpha$, and Am $L\alpha$ x-rays. WDX maps used Nd $L\alpha$ and Am $M\beta$ x-rays.

The Si map in Figure 65 indicates that the rind is high in Si. The boundary between the high Si rind and the interior of the sample appears irregular. The Zr map suggests that the Zr content in the rind is slightly higher than the interior. The Pr map has a greater number of lighter contrast spots and also suggests that the boundary between the rind and interior may be irregular. The rind appears lower in U than the interior of the sample. The Am WDX map shows that the high-Nd “fingers” are also high in Am.

Figure 65 contains more images of the edge region showing the high Si rind. Each row contains an SE image, a high-contrast BSE image, and a low-contrast BSE image. The images show that the rind has a complex structure and is different than the inner matrix.

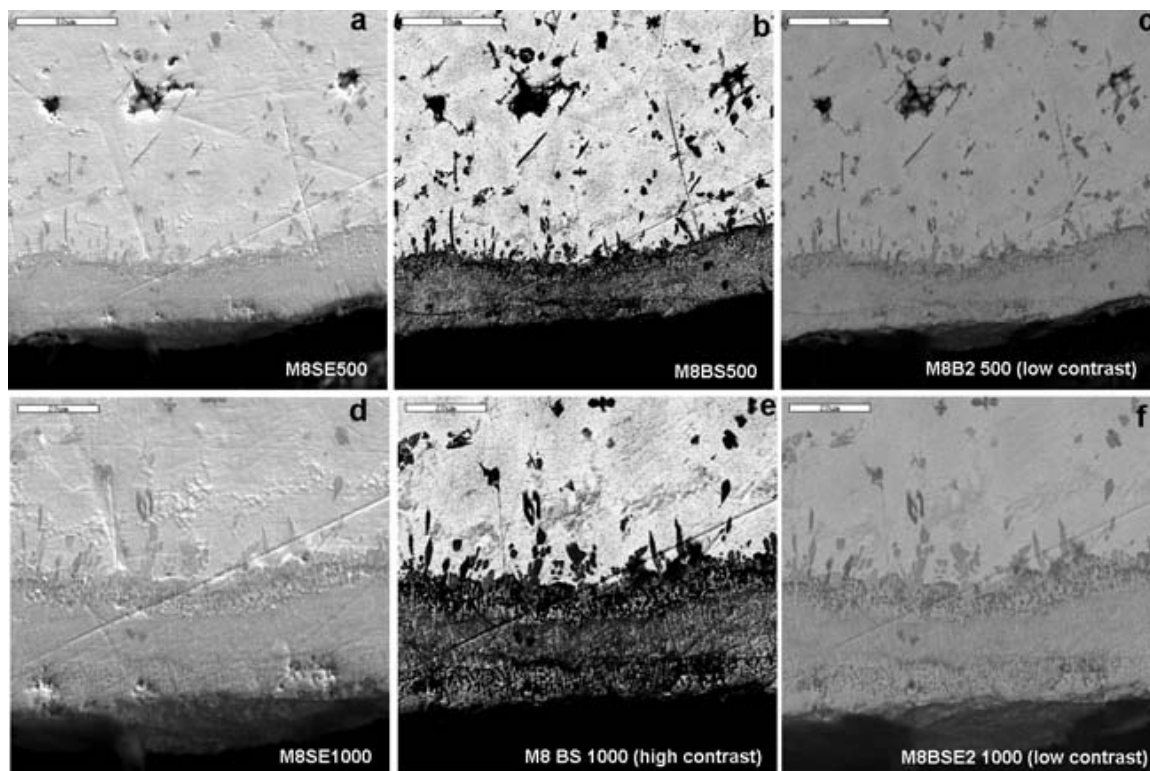


Figure 65. Micrograph images of the rim region: (a) SE image (b) high-contrast BSE image (c) low-contrast BSE image (d) SE image (e) high-contrast BSE image (f) low-contrast BSE image.

The available data from the SEM microstructural analysis on the 59U-20Pu-3Am-2Np-1RE-15Zr (A2) composition sample suggest that the sample consists of at least five phases:

1. High Zr content inclusions, which are low in actinides;
2. High RE content inclusion, which is low in U, Pu, Zr, and high Am content. These Am-rich inclusions are the smaller of the high RE inclusions;
3. High RE content inclusions, which are low in U, Pu, Zr, and a low Am content. These low Am content inclusions are the larger of the RE inclusions;
4. High Si rind region on the outside of the sample;
5. A matrix, which is higher than the inclusions in U, Pu, and probably Np. BSE images show a fairly uniform patchy contrast throughout the matrix. Areas that were light in BSE images were higher in U and lower in Zr, while areas that were darker in the BSE images were higher in Zr and lower in U.

were higher in Zr and lower in U. Pu appeared fairly uniformly distributed throughout the matrix. Little could be concluded about the distribution of Np because of its low concentration. Boundaries between high U and high Zr content areas are always diffuse, and it is not clear whether these areas are separate phases or different compositions in a single-phase solid solution.

- 58.5U-20Pu-3Am-2Np-1.5RE-15Zr (A3)

One sample from the (58.5U-20Pu-3Am-2Np-1.5RE-15Zr (A3)) fuel slug was examined. All of the data presented here are from the AFC2-A3-83-1-SEM1 sample (see Figure 66).

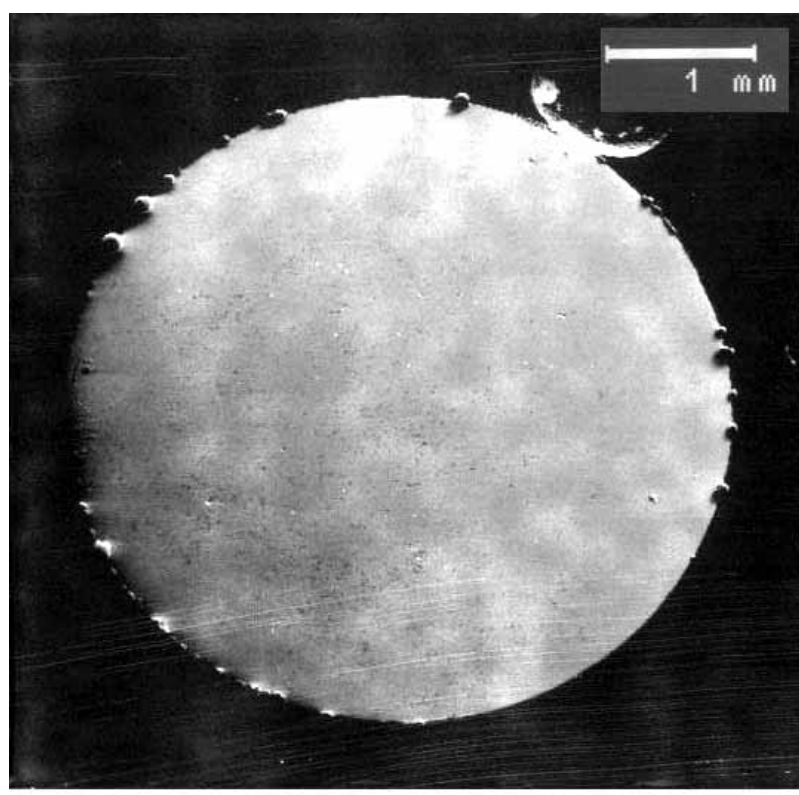


Figure 66. Low magnification images of the 58.5U-20Pu-3Am-2Np-1.5RE-15Zr (A3) casting sample AFC2-A3-83-1-SEM1.

Figure 67 shows that the distribution and shapes of the inclusions found in the 58.5U-20Pu-3Am-2Np-1.5RE-15Zr (A3) sample. Both light and dark contrast phases are observed in the matrix phase resulting from gradual variations in contrast and may indicate compositional gradients within this phase (see Figure 68).

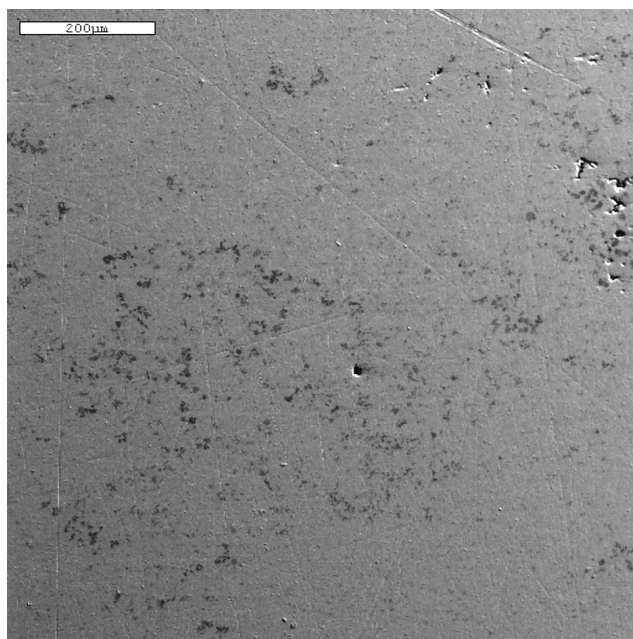


Figure 67. Secondary electron (SE) image of the 58.5U-20Pu-3Am-2Np-1.5RE-15Zr (A3) sample, AFC2-A3-83-1-SEM1.

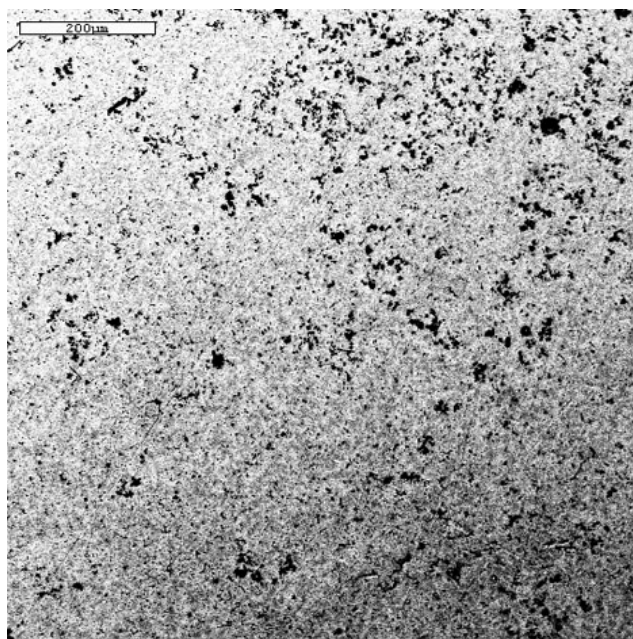


Figure 68. Backscattered electron image (BSE) of the 58.5U-20Pu-3Am-2Np-1.5RE-15Zr (A3) sample, (AFC2-A3-83-1-SEM1).

A more detailed examination of the features of the microstructure revealed that the phases in the rare-earth doped 58.5U-20Pu-3Am-2Np-1.5RE-15Zr (A3), like 59U-20Pu-3Am-2Np-1RE-15Zr (A2), are more complex than that found in the non-RE-containing alloys. The image shown in Figure 69 suggests the possible presence of at least five different types of inclusions, surrounded by a matrix that appears similar to that observed in 60U-20Pu-3Am-2Np-15Zr (A1). Inclusion A (see Figure 69) is very dark with a blocky shape. Inclusion B is long and slender with intermediate contrast. Inclusion C is rounded with internal phase contrast variations, but similar in contrast to B. Inclusion D is intermediate between A and B in contrast. Inclusion E is lighter than the matrix in SE images and darker than the matrix in BSE images.

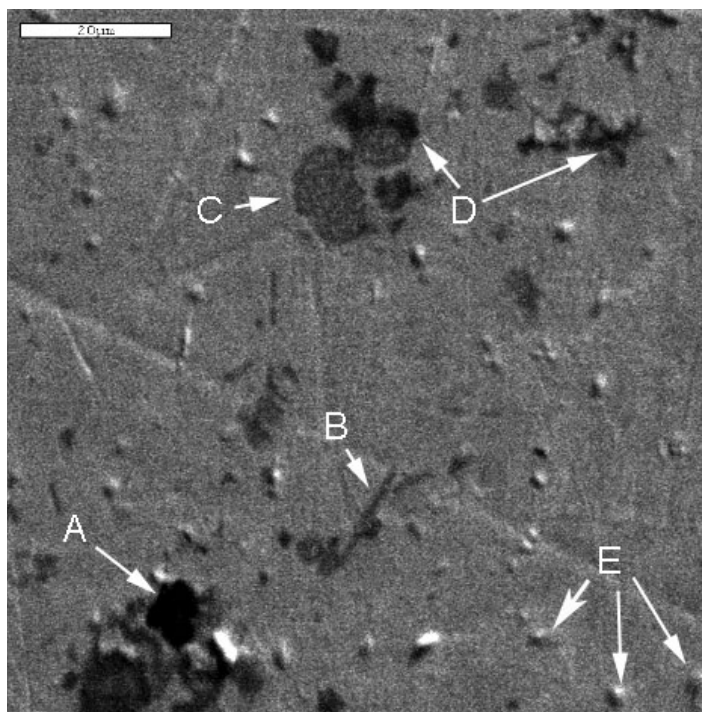


Figure 69. Secondary electron image of the 58.5U-20Pu-3Am-2Np-1.5RE-15Zr (A3) sample, (AFC2-A3-83-1-SEM1).

X-ray maps from the center of the sample (see Figure 70) confirm the similarities and differences between the inclusions in 58.5U-20Pu-3Am-2Np-1.5RE-15Zr (A3). Maps for C and Si (not shown) indicate that inclusion A is silicon carbide (probably a particle of the abrasive used to grind the sample surface). Inclusions B and C are enriched in rare-earth elements (La, Ce, Pr, Nd) and depleted in Zr and the actinides (U, Np, Pu, Am). Inclusion D is enriched in Zr and depleted in actinides and rare-earth elements. Figure 70 also illustrates another unique characteristic of composition 58.5U-20Pu-3Am-2Np-1.5RE-15Zr (A3): Am is enriched in small inclusions like those labeled E in Figure 71. These inclusions are depleted in U. Although concentration relationships for the rare-earth elements (La, Ce, Pr, and Nd) and Np and Pu are difficult to confirm because of the low contrast in the maps for these elements in the areas with high-Am inclusions, the x-ray maps suggest that the inclusions may be enriched in rare-earth elements and depleted in Np and Pu.

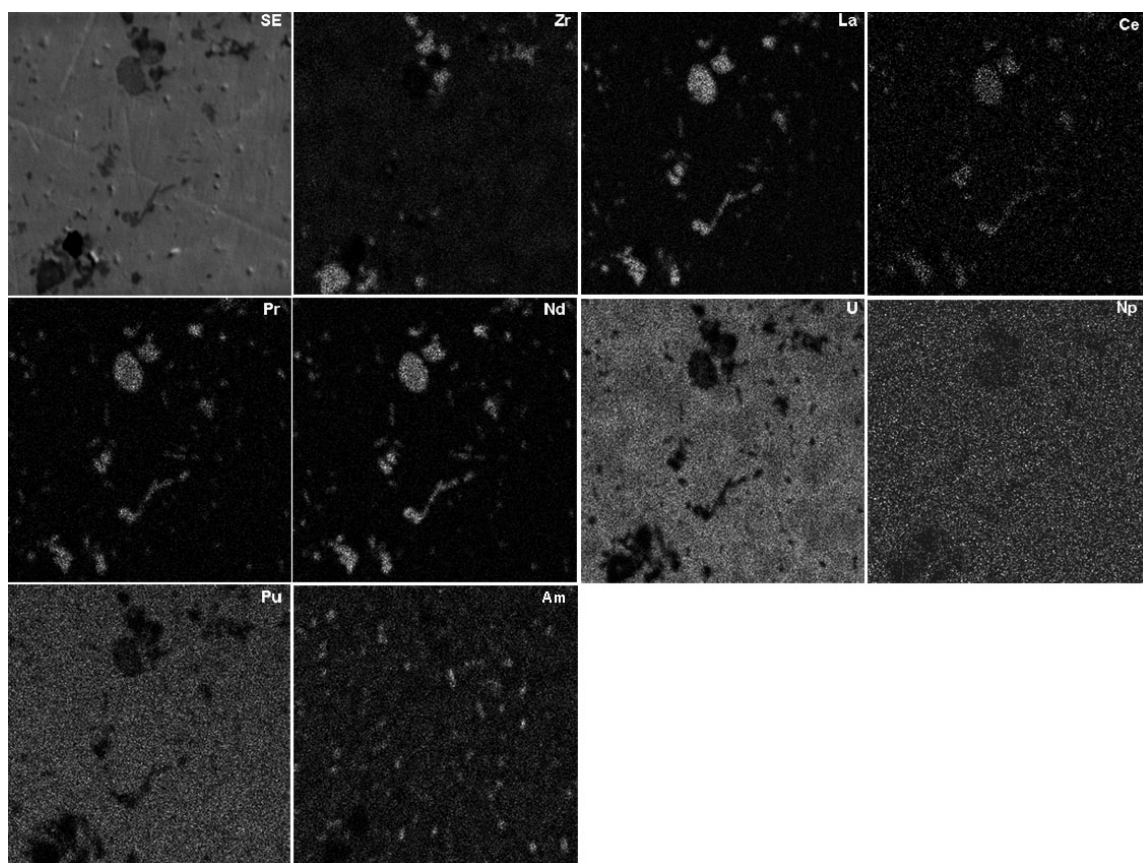


Figure 70. X-ray maps of the center of the 58.5U-20Pu-3Am-2Np-1.5RE-15Zr (A3) casting sample, AFC2-A3-83-1-SEM1.

Comparisons between the x-ray maps of Figure 70 and x-ray maps obtained from the edge of the same sample (see Figure 71) illustrate further complexities in the behavior of Am. The SE image and all of the maps –except that for Am in Figure 71– show relationships similar to those observed in Figure 70, suggesting that inclusions of types B, C, and D (but not A or E) occur in this area. Although the Am map in Figure 71 suggests a distribution of Am similar to that shown in Figure 70, no correlation exists between the high-Am areas seen in the x-ray map and any features observed in the SE images or the other elemental x-ray maps.

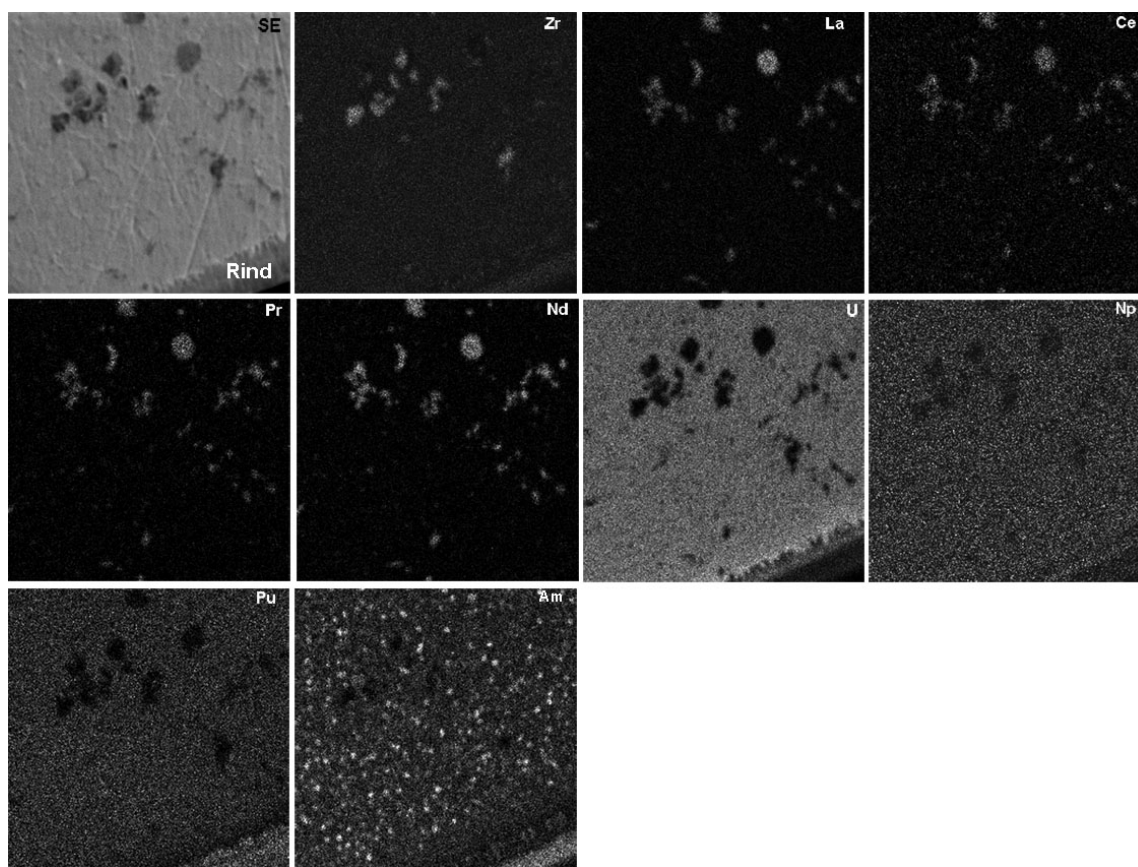


Figure 71. X-ray maps of the edge region of the 58.5U-20Pu-3Am-2Np-1.5RE-15Zr (A3) sample, (AFC2-A3-83-1-SEM1).

Just like the 59U-20Pu-3Am-2Np-1RE-15Zr (A2) alloy, the available data from the SEM microstructural analysis on the 58.5U-20Pu-3Am-2Np-1.5RE-15Zr (A3) sample suggest that the sample consists of at least five phases:

1. High Zr content inclusions, which are low in actinides;
2. High RE content inclusion, which is low in U, Pu, Zr, and high Am content. These Am-rich inclusions are the smaller of the high RE inclusions;

3. High RE content inclusions, which are low in U, Pu, Zr, and a low Am content. These low Am content inclusions are the larger of the RE inclusions;
 4. High Si rind region on the outside of the sample;
 5. A matrix, which is higher than the inclusions in U, Pu, and probably Np. BSE images show a fairly uniform patchy contrast throughout. Light areas in BSE images were higher in U and lower in Zr, while areas that were darker in the BSE images were higher in Zr and lower in U. Pu appeared fairly uniformly distributed throughout the matrix. Little could be concluded about the distribution of Np because of its low concentration. Boundaries between high U and high Zr content areas are always diffuse, and it is not clear whether these areas are separate phases or different compositions in a single-phase solid solution.
- 40.5U-30Pu-5Am-3Np-1.5RE-20Zr (A4)

Figure 72 shows scanned thermal prints of SE and BSE images.

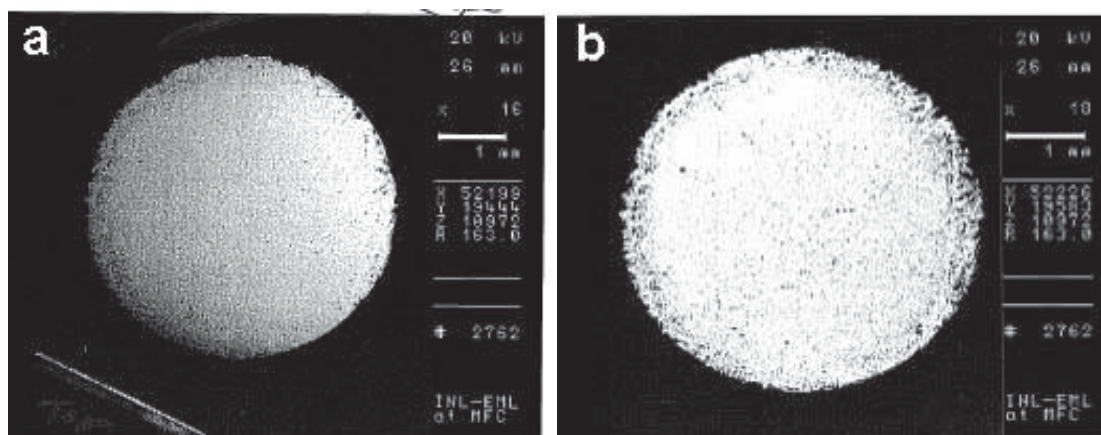


Figure 72. Scanned thermal prints showing low-magnification: (a) SE and (b) BSE images of an 40.5U-30Pu-5Am-3Np-1.5RE-20Zr (A4) sample. Scale bars: 1 mm.

The images in Figure 73 are traverse sections across the sample collected at relatively low magnifications. The irregular boundaries between the dark ring and center of the sample can be clearly seen and confirm that the dark material occurs only near the edge of the sample. Concern over the interaction with the fuel and the mold (as well as trying to reduce mold waste) resulted in experiments performed with Zr molds (Crawford et al. 1993). For the AFC-2 series of experiments it was decided not to use traditional quartz molds.

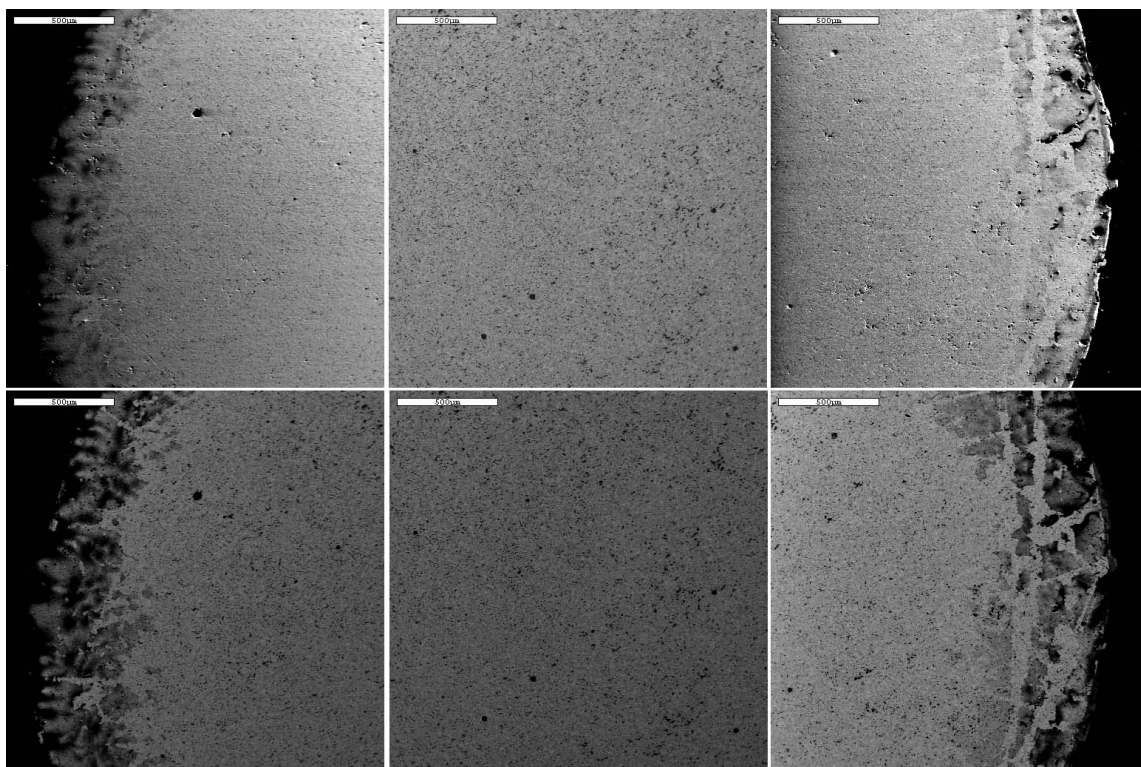


Figure 73. Overlapping SE (top row) and BSE images (bottom row) traversing 40.5U-30Pu-5Am-3Np-1.5RE-20Zr (A4) sample.

The x-ray maps (see Figure 74) show distributions of other elements. Inclusions can be divided into three groups: high content Si, high Zr content, and high Ln content. All four of the REs (La, Ce, Pr, and Nd) have similar distributions. U, Np, and Pu are lower in the high RE content and high Zr content inclusions than in the majority of the sample, suggesting that these elements occur primarily in the matrix. Variations in intensity in the Zr maps indicate that the matrix contains significant concentrations of Zr. Concentrations of U and Zr in the matrix both show patchy distributions and vary inversely (i.e., high content U areas are low in Zr and vice versa), as observed in other fuel samples. Concentrations of Np show patchy variations similar to that in U. Concentrations of Pu in the matrix appear constant. Areas with high concentrations of Am correspond closely to high RE content inclusions, although some high RE content inclusions are not high in Am. Am concentrations in the matrix adjacent to high Am content inclusions appear slightly lower than elsewhere, suggesting that the matrix may also contain significant Am. These observations correspond very closely to what was observed in the 58.5U-20Pu-3Am-2Np-1.5RE-15Zr (A3) alloy even though this 40.5U-30Pu-5Am-3Np-1.5RE-20Zr (A4) alloy is higher in U content and lower in Pu and Zr.

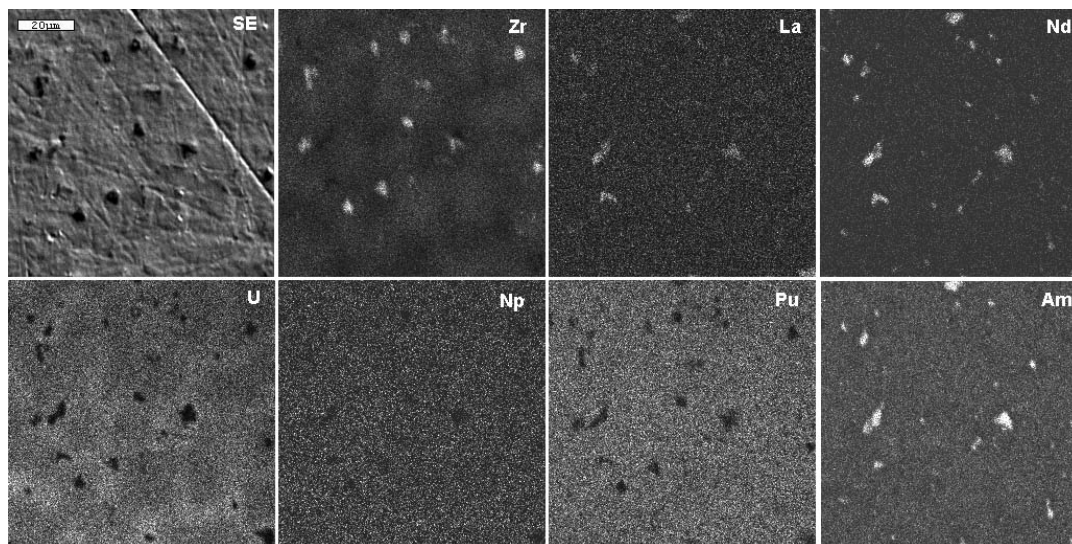


Figure 74. WDX x-ray maps (collected at 20 kV). Scale bar: 20 microns.

Distributions of U, Pu, and Zr are similar to previous samples and again show an inverse relationship between the concentrations of U and Zr in the matrix. The distribution of Pu in the matrix appears uniform, and contrast in the Np map is too low to tell whether concentrations of U and Np vary together. Distributions of La and Nd are similar. Close examination of the Nd and Am maps indicates that all high Am content areas are also high in Nd, but some high Nd content areas are not high in Am.

Figure 75 shows data obtained from an area about a third of the way from the edge of the sample to the center, and contains an SE image and two different contrasted BSE images of the same area. Close examination of the SE (see Figure 75a) and low-contrast BSE image (see Figure 75b) shows that some inclusions are darker than others. Patchy contrast in the matrix is particularly noticeable in the high-contrast BSE image (see Figure 75c).

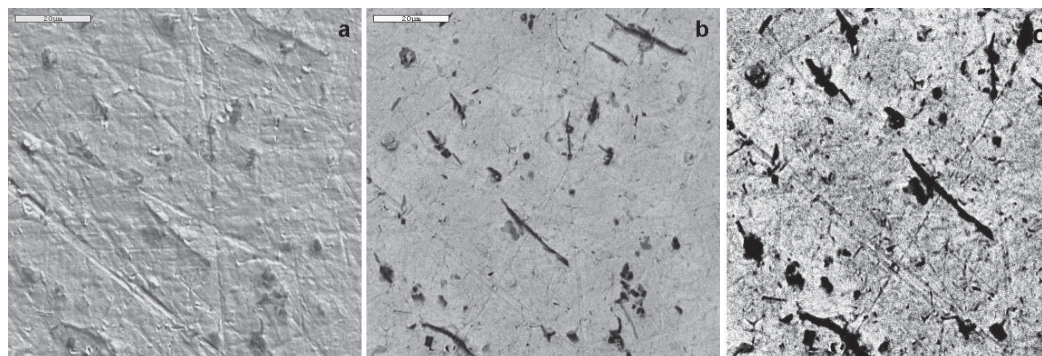


Figure 75. Images from an area about 1/3 of the way from the edge of the 40.5U-30Pu-5Am-3Np-1.5RE-20Zr (A4) sample to the center: (a) SE. (b) BSE, low contrast. (c) BSE image, higher contrast. Scale bars: 20 microns.

The x-ray maps in Figure 76 indicate that the actinide distributions are similar to those in previous x-ray maps. The long, slender inclusions are high in both Zr and Si, while some shorter, rounder ones have Zr without Si. The matrix material in the Zr and U maps has patchy contrast, with areas that are high in Zr being low in U and vice versa. Contrast in the U map corresponds to that in the high-contrast BSE image (see Figure 75c). All lanthanide elements apparently occur together, and, essentially, all high Am content areas are also high in Nd (but not always the reverse, i.e., some high Nd content areas are not high in Am).

Figure 77 shows SE and BSE images from a section of the rind at the edge of the sample. Black surface deposits can be observed in the upper left corner and along the lower edge of the BSE image. The area of the rind adjacent to the fuel appears to exhibit parallel-oriented dark contrast features, some of which extend into the fuel from the edge of the rind. Contrast in the matrix appears uniform. The inclusions have a variety of shapes, and some are far darker in BSE images than others. Many inclusions contain sharply delimited dark and light contrast areas. Dark-colored inclusions are typically high in Si and Zr, while light-colored ones are high in REs.

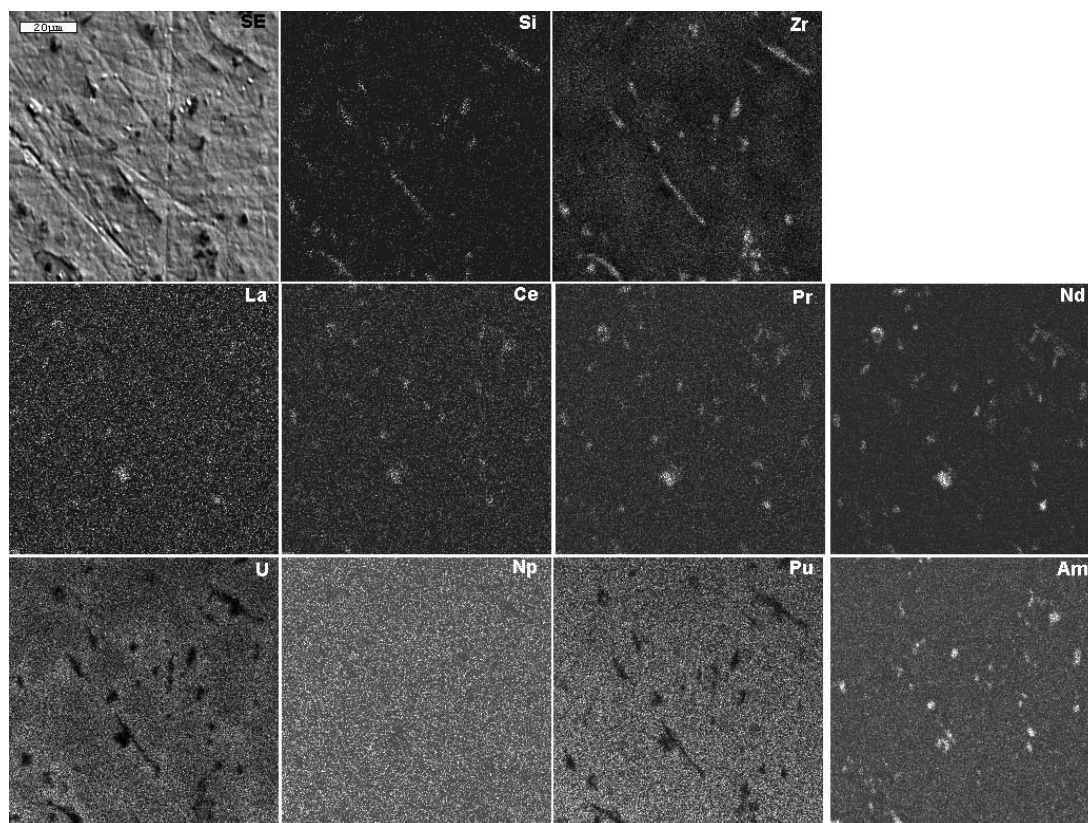


Figure 76. WDX x-ray maps (collected at 20 kV) from the area shown in Figure 75. Scale bar: 20 microns.

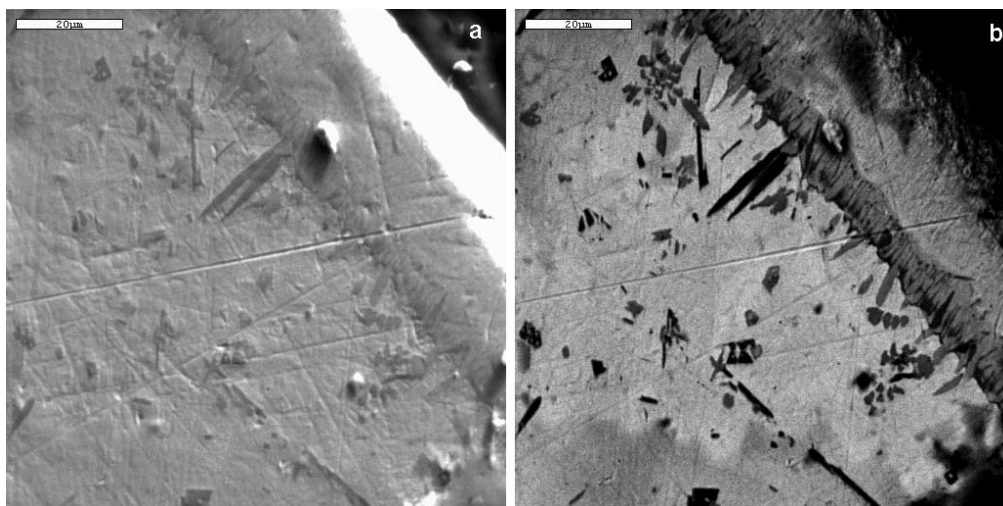


Figure 77. SE image (left) and BSE image (right) of the edge or rim area of the fuel sample. Scale bars: 20 microns.

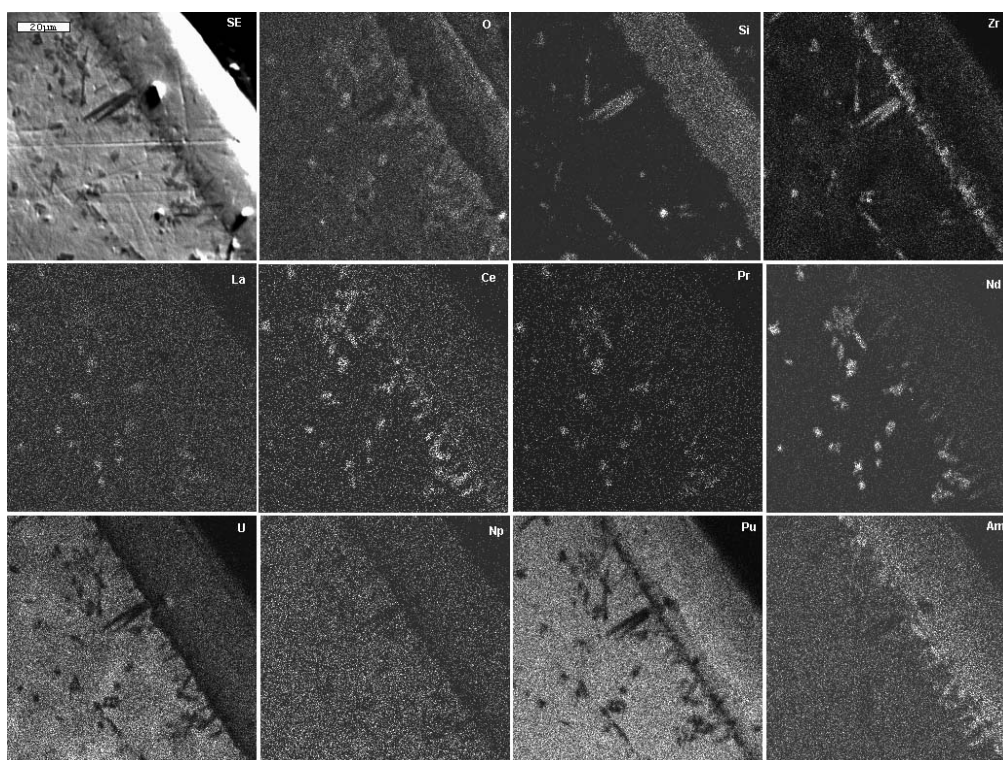


Figure 78. WDX x-ray maps (collected at 20 kV) from the area shown in Figure 77. Scale bar: 20 microns.

The x-ray maps of the inner matrix phase are similar to those from other locations in this sample. However, distributions of Si and Zr are clearly effected by the surface interaction but fortunately do not extend far into the sample.

In summary the 40.5U-30Pu-5Am-3Np-1.5RE-20Zr (A4) alloy consists of the following phases:

1. High Zr content inclusions, which are low in actinides;
 2. High RE content inclusion, which is low in U, Pu, Zr, and high Am content. These Am-rich inclusions are the smaller of the high RE inclusions;
 3. High RE content inclusions, which are low in U, Pu, Zr, and a low Am content. These low Am content inclusions are the larger of the RE inclusions;
 4. High Si rind region on the outside of the sample;
 5. A matrix, which is higher than the inclusions in U, Pu, and probably Np. BSE images show a fairly uniform patchy contrast throughout the matrix. Areas that were light in BSE images were higher in U and lower in Zr, while areas that were darker in the BSE images were higher in Zr and lower in U. Pu appeared fairly uniformly distributed throughout the matrix. Little could be concluded about the distribution of Np due to its low concentration. Boundaries between high U and high Zr content areas are always diffuse, and it is not clear whether these areas are separate phases or different compositions in a single-phase solid solution.
- 41U-30Pu-5Am-3Np-1RE-20Zr (A5)

Figure 79 shows a scanned thermal print of an SE image of the 41U-30Pu-5Am-3Np-1RE-20Zr (A5) sample. The image does not show a rind like other samples.

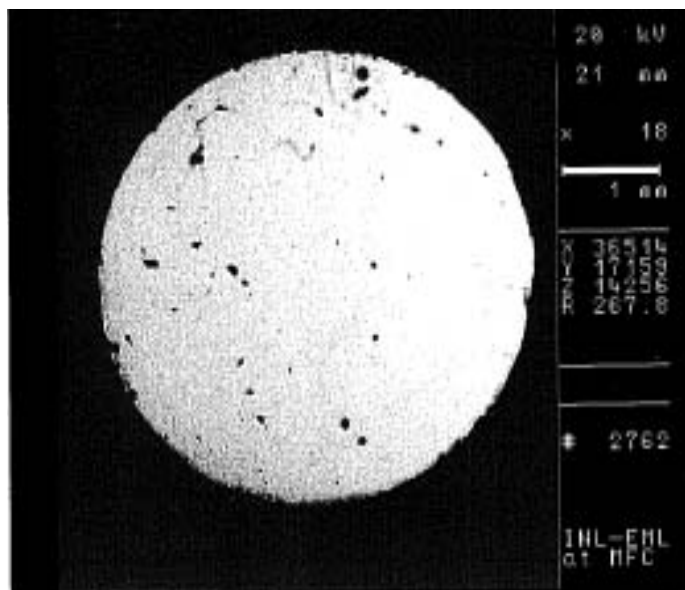


Figure 79. Scanned thermal print showing low-magnification SE image of the 41U-30Pu-5Am-3Np-1RE-20Zr (A5) sample. Scale bar: 1 mm.

Figures 80 and 81 show data obtained from an area approximately in the center of the sample. Figures 80a, 80b, and 80c are SE images, and Figures 80d, 80e, and 80f are the corresponding low contrast BSE images.

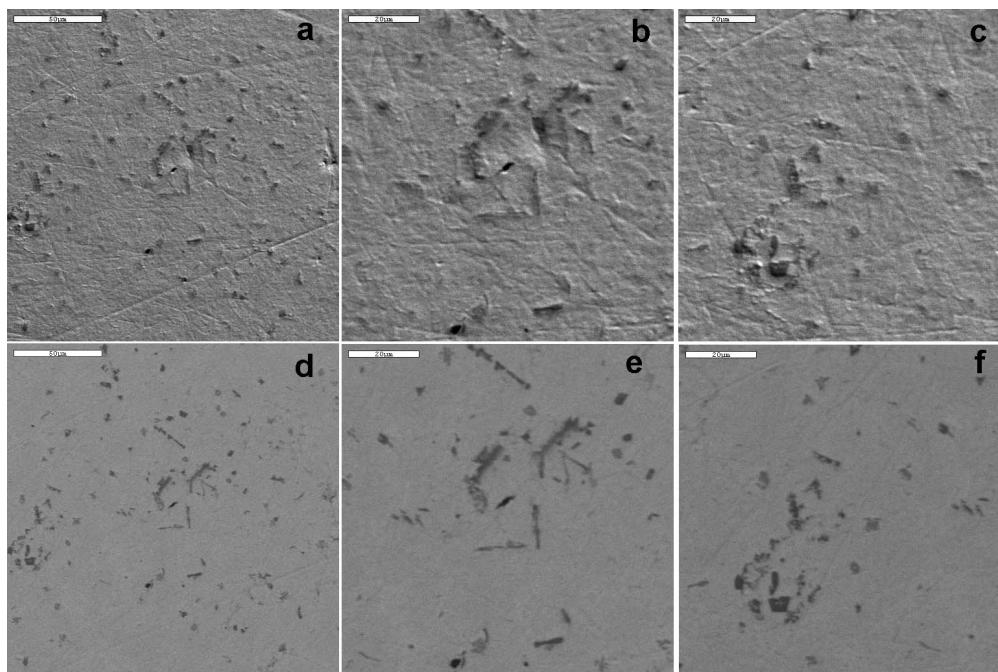


Figure 80. Sample 41U-30Pu-5Am-3Np-1RE-20Zr (A5) images. (a) SE image (b) higher magnification SE images of the central area of 'a.' Scale bar: 20 microns. (c) higher magnification SE image overlapping the left center of 'a.' Scale bar: 20 microns. (d – f) low contrast BSE images corresponding to 'a – c.'

Figure 81 contains WDX x-ray maps of approximately the area in Figures 80c and 80f. There is little Si and the distribution of Si does not appear to correspond to that of any other element. As a result the Si on the interior of this sample is assumed to be residual polishing media. Distributions of Zr, U, Np, and Pu are similar to those in previous alloys. The Am map shows fairly uniform contrast. A comparison between maps for Am and Nd suggests that there is little relationship between these elements; however, closer analysis and analogies to other samples suggest that many of the high Am content areas may correspond to small areas that are slightly higher in Nd. The association between Am and RE's is far less clear than in fuel sample 40.5U-30Pu-5Am-3Np-1.5RE-20Zr (A4).

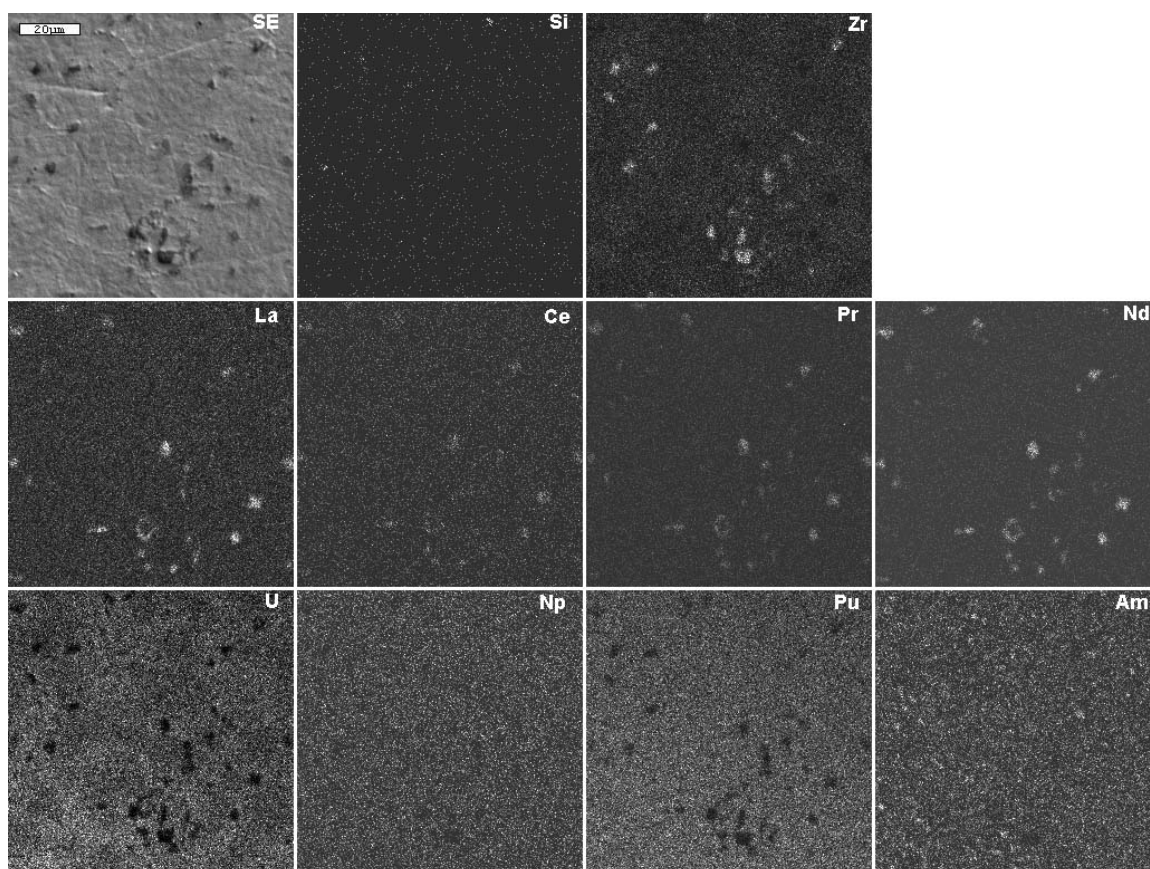


Figure 81. WDX x-ray maps (collected at 20 kV) from approximately the area shown in Figure 80f. Scale bar: 20 microns.

In summary the 41U-30Pu-5Am-3Np-1RE-20Zr (A5) alloy consists of the following phases:

1. High Zr content inclusions, which are low in actinides;
2. High RE content inclusion, which is low in U, Pu, Zr, and high Am content.

These Am-rich inclusions are the smaller of the high RE inclusions;

3. High RE content inclusions, which are low in U, Pu, Zr, and a low Am content. These low Am content inclusions are the larger of the RE inclusions;
 4. A matrix, which is higher than the inclusions in U, Pu, and probably Np. BSE images show a fairly uniform patchy contrast throughout the matrix. Areas that were light in BSE images were higher in U and lower in Zr, while areas that were darker in the BSE images were higher in Zr and lower in U. Pu appeared fairly uniformly distributed throughout the matrix. Little could be concluded about the distribution of Np because of its low concentration. Boundaries between high U and high Zr content areas are always diffuse, and it is not clear whether these areas are separate phases or different compositions in a single-phase solid solution.
- 42U-30Pu-5Am-3Np-20Zr (A6)

The 42U-30Pu-5Am-3Np-20Zr (A6) sample (AFC2-A6-82-5-SEM1) was obtained from a section of the fuel slug opposite the heel.

Figure 82 shows a low magnification of the 42U-30Pu-5Am-3Np-20Zr (A6) sample in which a degree of larger pores can be seen. Neither of these types of porosity has any discernible influence on the microstructure of the adjacent material.

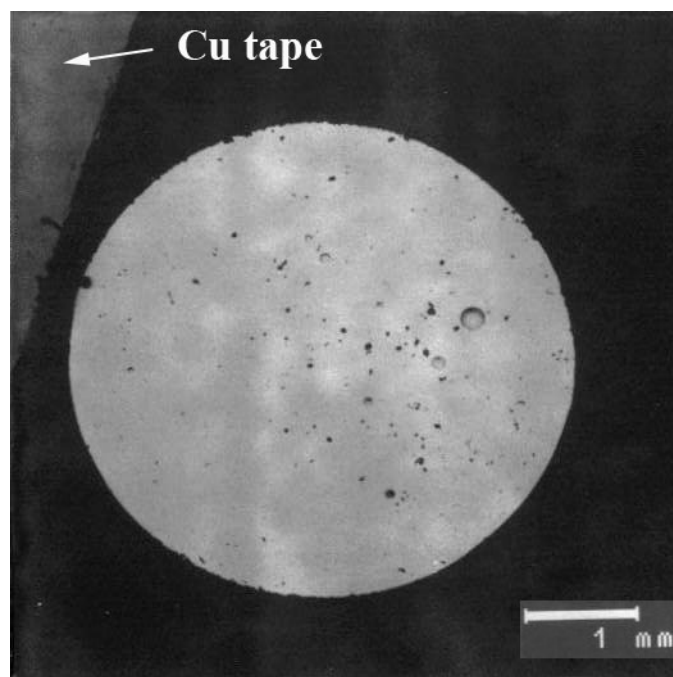


Figure 82. Low-magnification view of the 42U-30Pu-5Am-3Np-20Zr (A6) sample (AFC2-A6-82-5-SEM1).

Figure 83 shows a higher magnification SE image of the fuel around one of the larger pores. Again, the microstructure consists of two phases: a matrix phase, which appears light colored in SE images, and an inclusion phase, which appears darker (see Figure 83). The inclusions are commonly blocky or rounded in shape and up to $\sim 20\text{ }\mu\text{m}$ across. Backscattered electron images (see Figure 84) show that, in addition to the very dark inclusion phase, both light and dark contrast phases are observed in the matrix phase resulting from gradual variations in contrast and likely indicate compositional gradients within this phase.

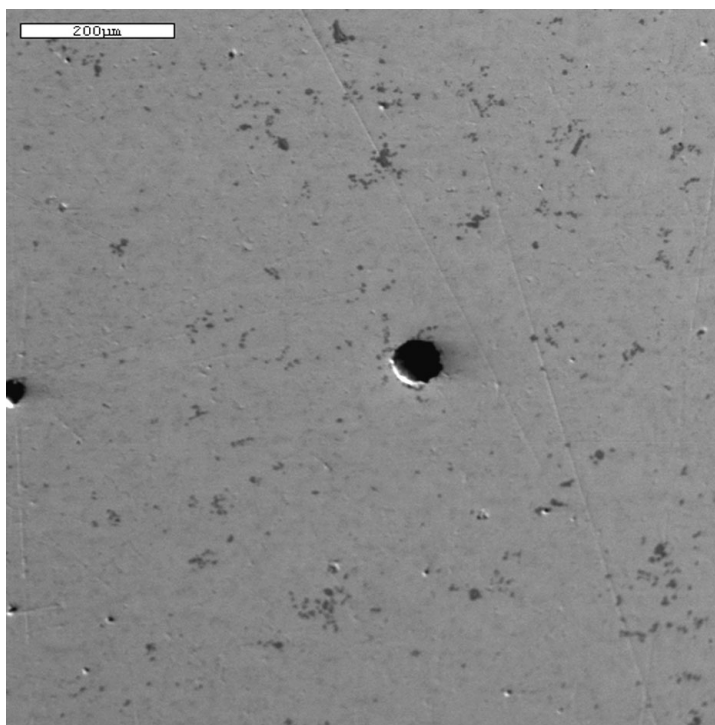


Figure 83. Secondary electron (SE) image of the ^{42}U - ^{30}Pu - ^{5}Am - ^{3}Np - ^{20}Zr (A6) sample (AFC2-A6-82-5-SEM1). Large dark areas in center and at left are internal porosity. Smaller dark areas are inclusions.

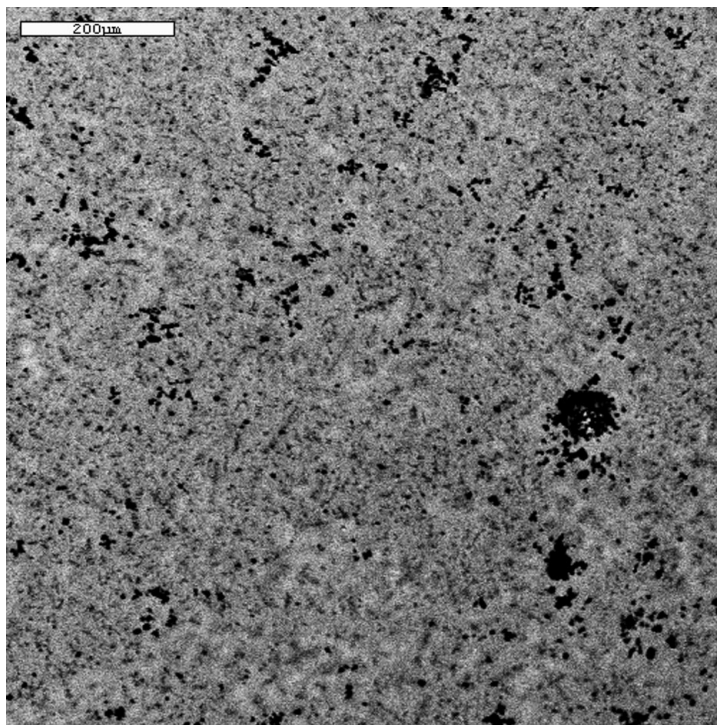


Figure 84. Backscattered electron (BSE) image of the 42U-30Pu-5Am-3Np-20Zr (A6) sample (AFC2-A6-82-5-SEM1).

Figure 85 presents x-ray maps obtained from the sample 42U-30Pu-5Am-3Np-20Zr (A6). Analysis of these maps indicates that the matrix is actinide-rich, while the inclusions are actinide-poor. Although most of the inclusions are enriched in Zr and depleted in the actinides compared to the matrix, a few inclusions (such as the very dark one in the lower center portion of the figure) are enriched in Si and C. I believe that the Si and C enrichment is a result of the sample preparation process (SiC abrasive) and, therefore, represents SiC surface (or embedded) particles, and is not intrinsic to the fuel. The x-ray maps indicate a fairly even distribution of Pu, Am, and Np throughout the matrix phase but some gradual contrast variation in uranium.

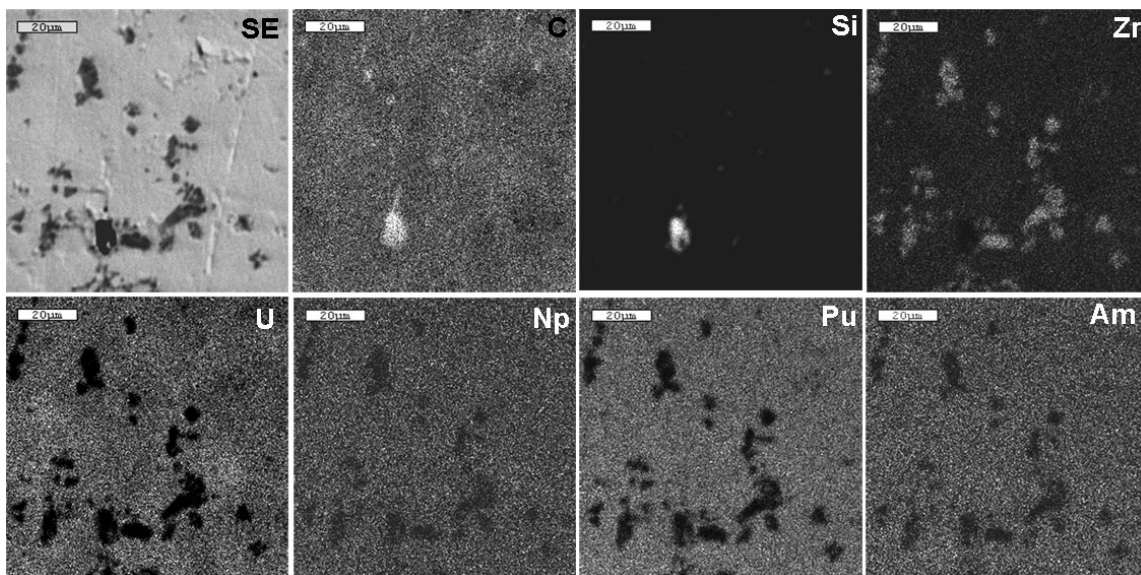


Figure 85. X-ray maps of sample 42U-30Pu-5Am-3Np-20Zr (A6) showing unusual silicon carbide inclusion and more typical zirconium-rich, actinide-poor inclusions.

In summary the 42U-30Pu-5Am-3Np-20Zr (A6) alloy consists of the following phases:

1. High Zr content inclusions, which are low in actinides;
2. A matrix, which is higher than the inclusions in the actinides.

4.2 Differential Scanning Calorimetry

Samples were cut from each rod for Differential Scanning Calorimetry (DSC) measurements to determine any phase changes in the alloy as a function of temperature (Bhadeshia date unknown).

Heating and cooling curves from room temperature to 800°C obtained from DTA type measurements are provided in Figure 86 for the 60U-20Pu-3Am-2Np-15Zr (A1) alloy. Observation of the data reveals repeatable and reproducible traces for each alloy. The first heating cycle for each alloy is slightly different than the subsequent two heats, suggested to result from an annealing effect on the as-cast samples as these alloys were not heat treated prior to measurement. This is supported by the observation that the same discrepancy between the three runs does not appear upon cooling. During all of the runs for each alloy, there are two very obvious, distinct transition zones that are reversible upon cooling. The alloys all show this similar feature, although the sharpness and intensity of each peak varies slightly depending upon the alloy stoichiometry. A very strong or sharp peak might suggest either a single phase transition or a transition through a very narrow phase field. A broad or weak peak might suggest a transition through a wide phase

field or overlap of two close, consecutive phase transitions. In all cases, the cooling curves appear to resolve the more complex phase behavior than that observed upon heating. (Burkes et al. 2010; Kennedy et al. 2007; Kennedy et al. 2008; Kennedy et al. August 2008). This characterization technique is much more effective than attempting to quench in phases for analysis as done in the past (Kruger 1966).

- 60U-20Pu-3Am-2Np-15Zr (A1)

Plots of three heating and cooling cycles between room temperature and 800°C are shown in Figure 86. The plots show that the observed transitions are reproducible, although some variation in baseline is observed, particularly at higher temperatures. A small amount of sample was lost during the three heating cycles (initial mass = 193.7 mg, final mass = 190.3 mg), amounting to about a 3.4 mg or 1.76 wt% loss from the bulk sample. The loss is most probably due to slight oxidation and powder formation through reaction with the alumina crucible liner material coupled with a small degree of Am vaporization.

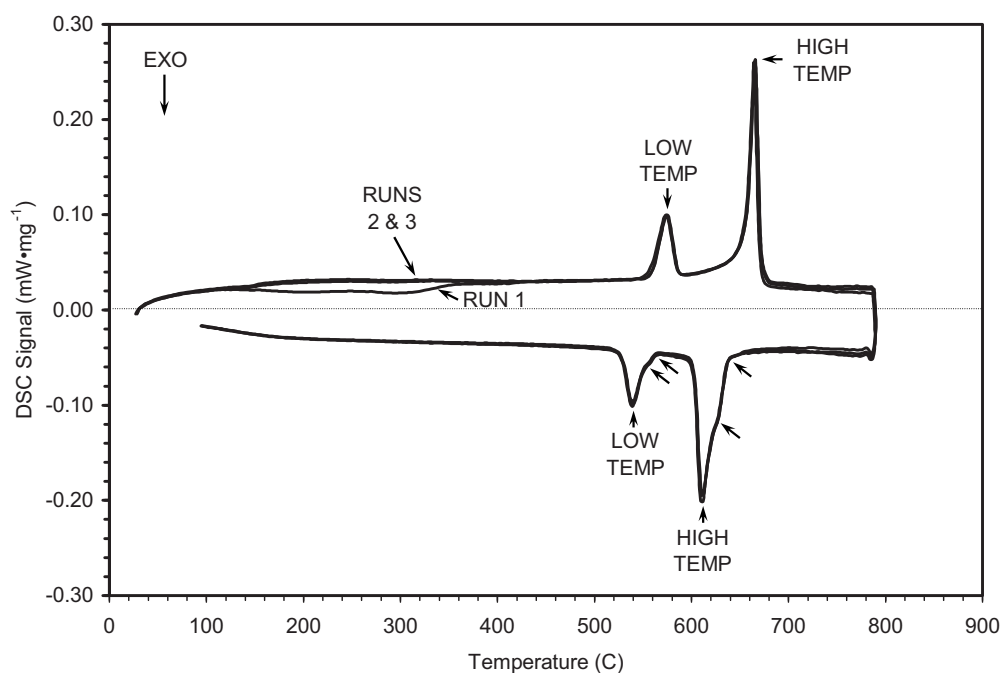


Figure 86. Heating and cooling traces obtained from the DSC/DTA measurements on the as-cast alloy 60U-20Pu-3Am-2Np-15Zr (A1).

The DTA analysis reveals two primary transitions and no indication of melting. The average temperature of the peaks of the transitions are listed in Table 10. These two temperature transitions are similar to those seen in U-19Pu-10Zr (Kim et al. 2004; Sohn et al. 2000) for the γ -phase to $\gamma + \zeta$ phase at the higher temperature and from $\gamma + \zeta$ phase to ζ phase at the

lower temperature. Similar transitions were also observed in U-15 Pu-13.5 Zr (Harbur, Anderson, and Maraman 1970). These phase transitions will be discussed in more detail later.

All other alloys were prepared and tested in a similar manner and their phase data is presented in Table 10.

Table 10. Transition temperature peaks for the all alloys.

	First Transition		Second Transition	
	Heating (°C)	Cooling (°C)	Heating (°C)	Cooling (°C)
A1	575	540	670	615
A2	580	560	665	610
A3	590	565	670	600
A4	560	535	650	605
A5	570	540	655	585
A6	565	535	660	585

4.3 Phase Discussion

The observed microstructures of all the AFC2-A fuel samples were investigated using an SEM and are fundamentally similar. All are composed of a primary matrix phase having light and dark contrast regions and dark-contrasted inclusions (in BSE images). The inclusions are enriched in Zr and depleted in actinides compared to the matrix phase. All of the actinides except uranium appear to be fairly well distributed throughout the matrix phase with variations in uranium content creating the different contrast regions. The lanthanides appear to precipitate out of the melt and form inclusions as opposed to dissolving within the fuel. This is not an entirely unexpected result since formation of fission product precipitate phases have been observed in irradiated fuel studies (Keiser 1996) and the general immiscibility of the actinides with the lanthanides (Kurata, Inoue, Sari 1994) U-Pu-Zr alloys can dissolve Am and Np but not the rare earth elements. We also showed that the rare earths can dissolve Am and Pu, thus a mixture of a U-Pu-Zr-Np phase and an Am-Pu-Re phase were formed (Kurata, Inoue, and Sari 1994).

The gradual changes in concentration in U and Zr and inverse distributions of these elements in the matrix might suggest that the matrix consists of a single phase. Careful examination of the x-ray maps suggests a strong tendency for high Zr content inclusions to be surrounded by high Zr content matrix materials and for high RE content inclusions to be surrounded by high U content matrix. The U-Pu-Zr ternary phase diagram has not been determined and published for

temperatures below 500°C. The available data indicate both complete solid solution between U, Pu, and Zr at the solidus in the bcc γ -phase and a strong tendency to separate into several distinct phases at lower temperature (O'Boyle and Dwight 1970; Mueller et al. 1991) which is consistent with the x-ray map observations mentioned above. Figure 87 shows the phase diagram is from an experimental study within the U-Pu-Zr (O'Boyle and Dwight 1970). The reduced base compositions for the AFC2-A1 (60U-20Pu-3Am-2Np-15Zr = 61U-24Pu-15Zr = $U_{0.49}Pu_{0.19}Zr_{0.32}$) and AFC2-A6 (42U-30Pu-5Am-3Np-20Zr = 43.5U-36.5Pu-20Zr = $U_{0.33}Pu_{0.27}Zr_{0.40}$) are indicated in the diagram and show that at 500°C both compositions should remain within (δ -U Zr_2 + ζ -phase) phase field. All AFC2-A fuels; 60U-20Pu-3Am-2Np-15Zr (A1), 59U-20Pu-3Am-2Np-1Ln-15Zr (A2), 58.5U-20Pu-3Am-2Np-1.5Ln-15Zr (A3), 40.5U-30Pu-5Am-3Np-1.5Ln-20Zr (A4), 41U-30Pu-5Am-3Np-1Ln-20Zr (A5), and 42U-30Pu-5Am-3Np-20Zr (A6) are anticipated to be primarily composed of those phases.

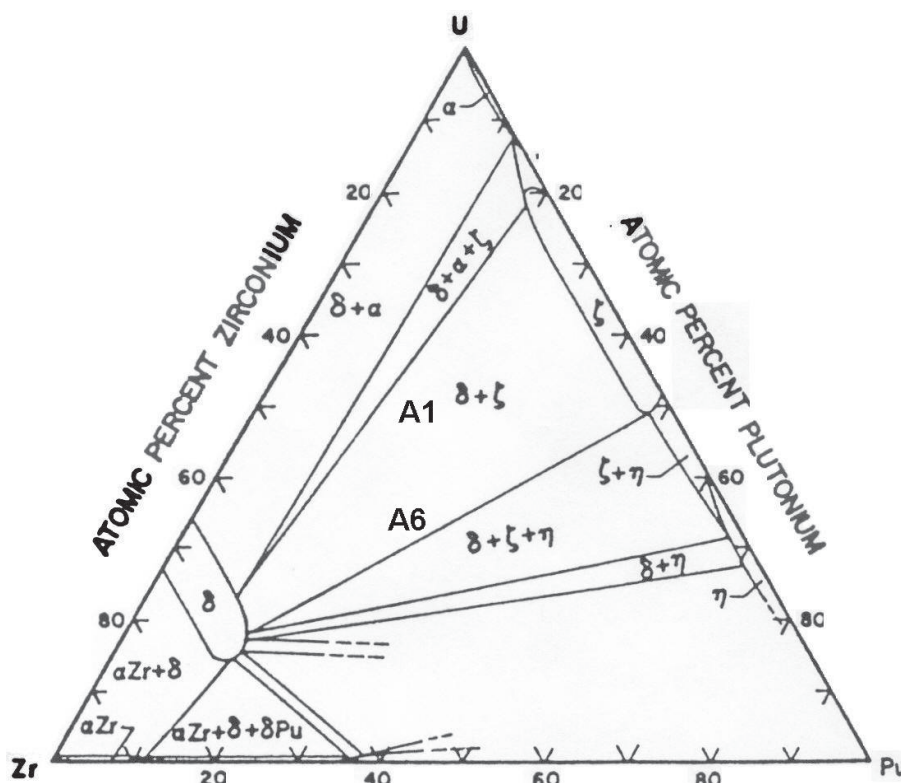


Figure 87. Experimental phase diagram of the U-Pu-Zr system (O'Boyle and Dwight 1970) at 500°C with the positions of the 60U-20Pu-3Am-2Np-15Zr (A1) and 42U-30Pu-5Am-3Np-20Zr (A6) compositions marked.

Identifying phases in a complex system based on qualitative observations of composition is difficult. Combining the observations with the assumption that all of the alloys want to maintain the two phases mentioned previously, the following solidification scenario is hypothesized:

- Precipitation of high Zr content inclusions from the melt. It is assumed that the Zr inclusions are a high-temperature phase that incorporates elements that are not part of the U-Pu-Zr ternary. But these phases do start the solidification process.
- Heterogeneous nucleation of the γ -phase around the high Zr content inclusions, and changing to lower Zr, higher U content compositions with decreasing temperature (and increasing distance from the original nucleation sites). All of the Np and Pu, and some of the Am would incorporate into this phase.
- As the REs are not anticipated to be miscible with phases in the U-Pu-Zr ternary, they would become increasingly concentrated in the remaining molten material, ultimately precipitating out as distinct phases.
- Depending on the kinetics and the possible presence of trace elements, high Am content areas associated with REs could result from one of three processes: (1) Precipitation of a high Am content phase, which becomes a nucleus for heterogeneous condensation of RE phases, (2) Heterogeneous nucleation of high Am content phases on precipitates of high RE content phases, or (3) Precipitation of Am-RE solid solution phases, possibly followed by later segregation into high Am content and high RE content phases.

This scenario can generally map the development of the observed microstructure in these as-cast fuel samples while neglecting the phase transformations following solidification of the γ -phase below the solidus-liquidus. The complexity of the developed (nonequilibrium) microstructures will require a far more detailed study to fully understand the microstructure and how it was formed (Janney and Kennedy 2010; Kennedy et al. 2003; Kennedy and Janney 2007; Kennedy et al. 2008; Marples 1960; Mardon, Pearce, and Marples 1961).

Isothermal sections of the U-Pu-Zr system are available from published literature at 773 K, 823 K, 853 K, 868 K, 913 K (O'Boyle and Dwight 1970). These diagrams indicate the position of the reduced composition for alloys 60U-20Pu-3Am-2Np-15Zr (A1) and 42U-30Pu-5Am-3Np-20Zr (A6) (i.e., the base composition alloys) (see Figure 88). The room temperature ternary phase diagram described in INL/EXT-08-14499, "AFC2-A,B Metal Fuel Characterization FY 2008 Supplemental Report." Figure 88 shows the reduced composition positions marked for alloys 60U-20Pu-3Am-2Np-15Zr (A1) and 42U-30Pu-5Am-3Np-20Zr (A6). Figure 89 was produced from experience and thermodynamics calculations (Nakamura, Ogata, and Kurata 2005; Leibowitz, Blomquist, and Pelton 1989; Kurata, Nakamura, and Ogata 2001; Kennedy et al. August 2008).

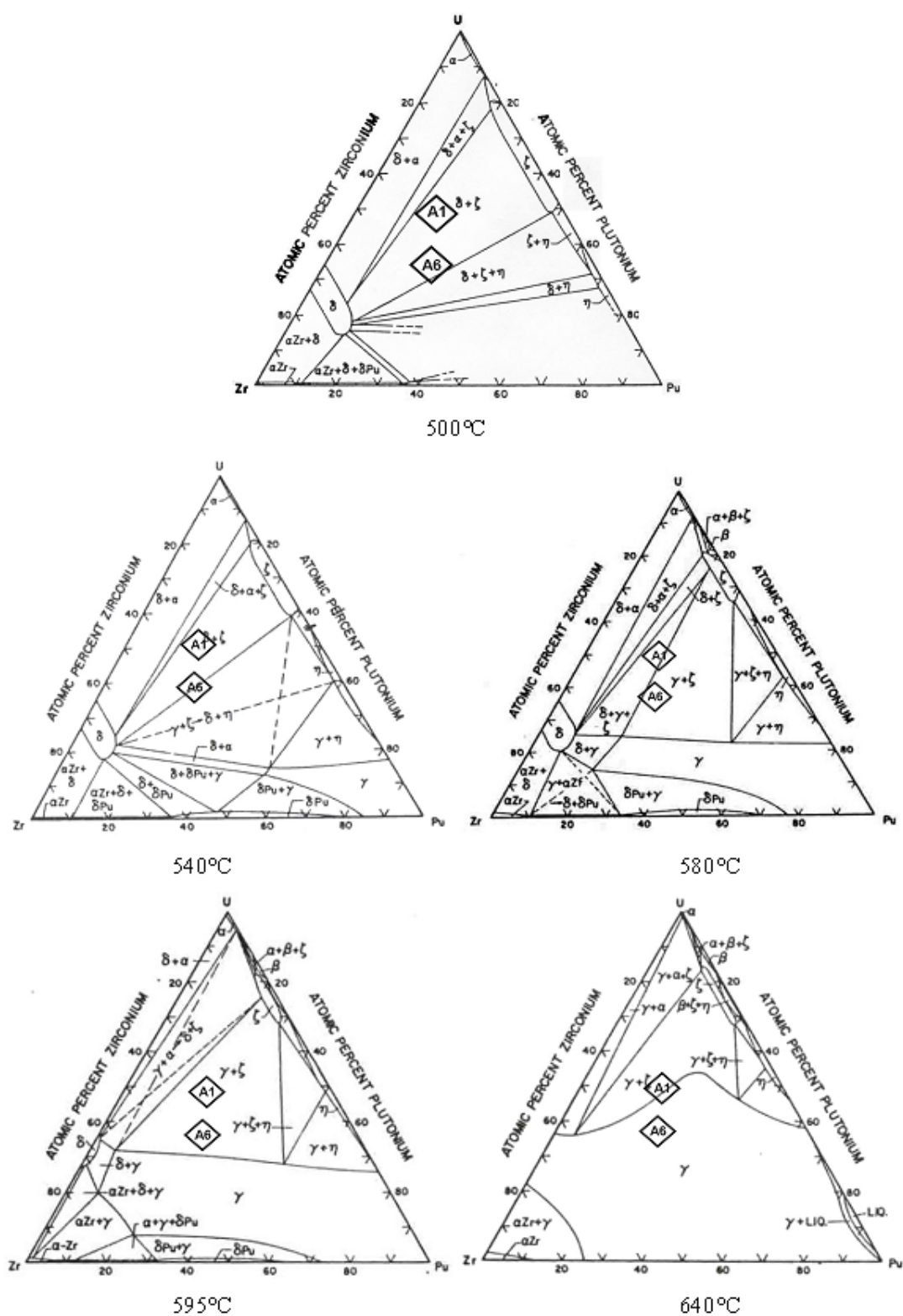


Figure 88. Ternary U-Pu-Zr phase diagrams taken at isothermal sections with reduced composition (in terms of U-Pu-Zr), for alloys 60U-20Pu-3Am-2Np-15Zr (A1) and 42U-30Pu-5Am-3Np-20Zr (A6).

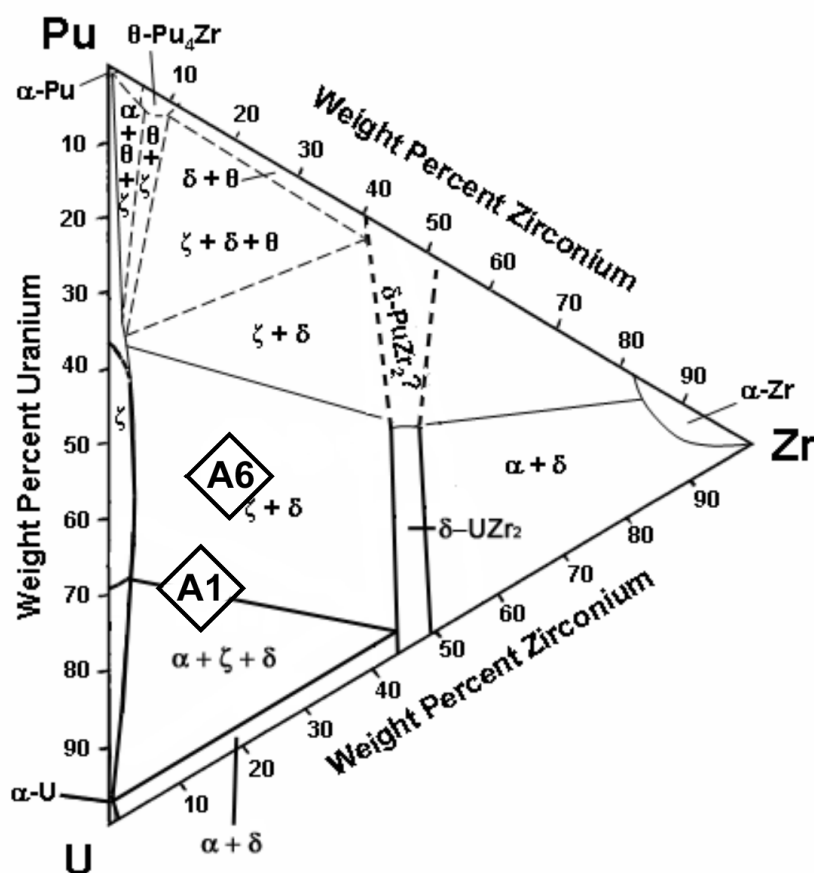


Figure 89. A room temperature U-Pu-Zr ternary phase diagram estimated from isothermal sections and the three binary phase diagrams of the elements involved (Kennedy et al. August 2003).

Evaluating the DTA traces from all the alloys revealed two primary phase transition zones, while two or more additional phase transitions (lower in intensity) are observed upon cooling. Considering only the cooling cycles, the onset of each transition could be determined and correlated with the U-Pu-Zr ternaries presented in Figures 88 and 89. These results are summarized in Table 11 for each metal alloy. This table shows how accurately our “reduced” compositions compare to the measured U-Pu-Zr system. Ultimately, indicating our additions do not change the 2 or 3 primary phases.

Table 11. Onset of experimental phase transitions determined upon cooling the samples and predicted phase transitions based on the U-Pu-Zr ternary diagrams (O'Boyle and Dwight 1970) for each metal alloy.

Transition	$\delta + \zeta \rightarrow \delta + \gamma + \zeta$	$\delta + \gamma + \zeta \rightarrow \gamma + \zeta$	$\Gamma + \zeta \rightarrow \gamma$
<i>Predicted (°C)</i>	550-580	580-595	>640
A1 (°C)	562 ± 2.3	621 ± 0.4	637 ± 0.6
A2 (°C)	567 ± 0.2	619 ± 0.4	649 ± 0.8
A3 (°C)	572 ± 0.3	602 ± 0.7	635 ± 0.1
Transition	$\delta + \zeta \rightarrow (\gamma + \zeta \rightarrow \delta + \eta)$	$(\gamma + \zeta \rightarrow \delta + \eta) \rightarrow \gamma + \zeta$	$\gamma + \zeta \rightarrow \gamma$
<i>Predicted (°C)</i>	550-580	580-595	>595
A4 (°C)	547 ± 0.2	612 ± 0.6	628 ± 1.1
A5 (°C)	547 ± 0.4	594 ± 0.5	624 ± 1.5
A6 (°C)	547 ± 0.3	595 ± 0.5	625 ± 0.4

The following discussion refers to the equilibrium ternary phase diagrams in Figures 88 and 89. For alloys based on the 60U-20Pu-3Am-2Np-15Zr (A1) composition, the first transition from $\delta + \zeta \rightarrow \delta + \gamma + \zeta$ should occur between 550°K and 580°K. The alloys should be composed of approximately 56% ζ -phase and 44% δ -phase at 500°C. This means that a significant portion of the ζ -phase has transformed to δ -phase upon heating from room temperature, which contained ~81% ζ -phase. This transition could occur rather slowly, as the $\delta + \zeta$ two-phase field is quite large. At 580°C, the $\delta + \zeta$ phase has transitioned into the narrower $\delta + \gamma + \zeta$ three-phase field and is composed of only approximately 5% δ -phase, with the remaining 95% consisting of $\gamma + \zeta$. The experimental onset values for the first transition range from 562 to 572°C and support the predicted transition. At 595°C, the $\delta + \gamma + \zeta$ phase should have transitioned into the $\gamma + \zeta$ two-phase field based on the ternary phase diagram predictions. A tie line drawn through the position of the reduced composition suggests approximately 52% γ and 48% ζ . The onset temperature observed during cooling for the three alloys ranges from 594 to 612°C, decreasing in value with increasing RE contents. The onset of transition for each alloy is close to the predicted value and, given super-heating/-cooling effects, a 25 degree difference is reasonable. At 640°C, most of the ζ phase remaining should have transformed into γ -phase (>90%). Complete transformation into the γ phase should occur above 640°C, and, in fact, this is the observed trend with the transition onset upon cooling occurring between 635 to 649°C.

For metal alloys based on the 42U-30Pu-5Am-3Np-20Zr (A6) composition, the first transition from $\delta + \zeta \rightarrow (\gamma + \zeta \rightarrow \delta + \eta)$ should occur above 550°C. The alloys are composed of approximately 44% ζ -phase and 56% δ -phase at 500°C. This means that a significant portion of the ζ -phase has transformed to δ -phase upon heating from room temperature, which contained ~62% ζ -phase. This transition could occur rather slowly, as the $\delta + \zeta$ two-phase field is quite large. Above 550°C, the $\delta + \zeta$ phase has transitioned into the very large $(\gamma + \zeta \rightarrow \delta + \eta)$ phase field. The experimental onset values for the low temperature transition are 547°C and, given slight supercooling effects, support the predicted transition. The transition becomes broader with the RE addition that suggests the transition occurs through two wide phase fields. At 580°C, the $(\gamma + \zeta \rightarrow \delta + \eta)$ phase should have transitioned into the $\gamma + \zeta$ two-phase field based on the ternary phase diagram predictions. The onset temperature obtained during cooling for the three alloys ranges from 594 to 612°C, with no apparent dependence on the RE content. Above 595°C and below 640°C, all of the ζ phase remaining should have transformed into γ -phase. The experimental transition temperatures observed range from 624 to 628°C, supporting the predicted trend (Kennedy et al. August 2008).

In closing the phase discussion, all other analysis techniques agree with the two phase transition temperatures detected using the TMA and the phase fields published for the U-Pu-Zr system match our alloys and our “reduced” alloys.

4.4 Thermal Conductivity Discussion

In an effort to make the data available in this thesis complete, thermal conductivity and the data required to calculate it are presented here. Thermal conductivity, or the unit of measure of how well a material can conduct heat, is a function of the specific heat capacity, thermal diffusivity and density, all as a function of temperature. TMA data and the starting density measurements were presented earlier. Thermal diffusivity and specific heat capacity are presented below.

4.4.1 Laser Flash Diffusivity

12.6 mm diameter samples were cast and sectioned specifically for LFD measurement (Burkes et al. 2010; Kennedy et al. 2007; Kennedy et al. 2008).

- 60U-20Pu-3Am-2Np-15Zr (A1)

One sample of approximately 12.6 mm diameter and 1 mm thickness was analyzed for thermal diffusivity. Some thermal cycling effects were exhibited over the course of the first

few measurement cycles before reproducible results were obtained. The measured diffusivity values determined using the Clark and Taylor method and a 100-point moving average are listed in Table 12 and plotted in Figure 90. The temperature dependence of this sample appears to have two regions, one from 150°C to about 650°C, and the other from 650 to 1,000°C. These values run from about 0.05 cm²/sec to 0.07 cm²/sec and 0.07 cm²/sec to 0.09 cm²/sec respectively. Equations 1 and 2 are the second order polynomial relations for the phases below and above the transition and allow for a fairly good fit of the data. The correlation Equations 1 and 2 will be used for the thermal conductivity determinations.

Table 12. Thermal diffusivity values at temperature determined for the 60U-20Pu-3Am-2Np-15Zr (A1) alloy.

Temperature °C	Diffusivity cm ² /sec	Std. Dev.
194	0.0465	0.004
243	0.0522	0.0011
293	0.052	0.0037
342	0.0572	0.0034
392	0.0598	0.0032
440	0.0627	0.0016
490	0.0639	0.0026
538	0.0661	0.0015
587	0.0684	0.0021
638	0.0705	0.0011
684	0.0775	0.0016
731	0.0818	0.0016
779	0.084	0.0012
828	0.0875	0.0009
875	0.0896	0.0025
923	0.092	0.0014
971	0.0927	0.0017

$$100-600^{\circ}\text{C} \quad \alpha = -5.048 \times 10^{-8}T^2 + 9.321 \times 10^{-5}T + 3.0847 \times 10^{-2} \quad (R^2 = 0.983) \quad (1)$$

$$600-1,000^{\circ}\text{C} \quad \alpha = -1.150 \times 10^{-7}T^2 + 2.459 \times 10^{-4}T - 3.744 \times 10^{-2} \quad (R^2 = 0.989) \quad (2)$$

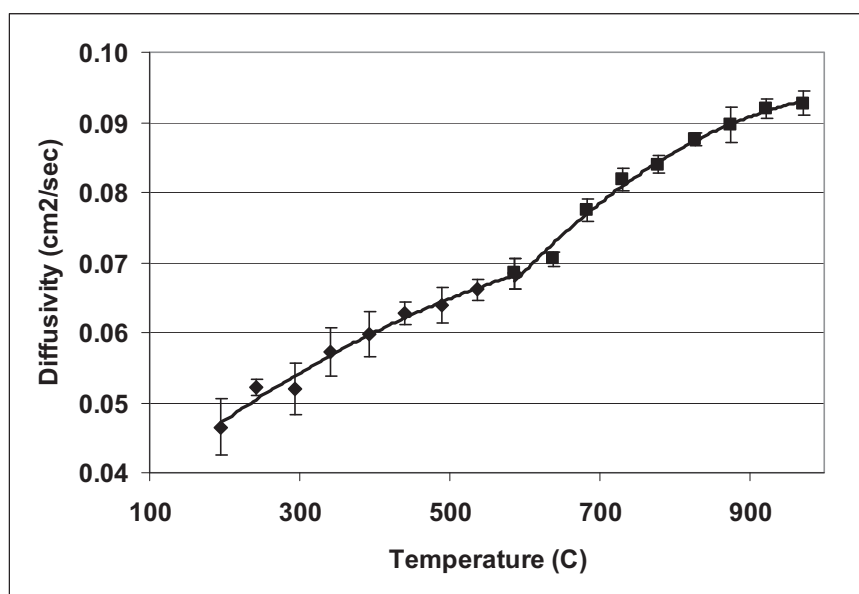


Figure 90. Thermal diffusivity plot for 60U-20Pu-3Am-2Np-15Zr (A1) alloy with correlated fits from Equations 1 and 2.

All other alloys were processed and measured in the same manner and in the interest of brevity are not presented here. The following graph (see Figure 91) shows all six alloys on the same plot. As you can see 60U-20Pu-3Am-2Np-15Zr (A1) and 42U-30Pu-5Am-3Np-20Zr (A6) do have different properties and show up distinctly different on the plot. The other alloys fall in between these two measurements.

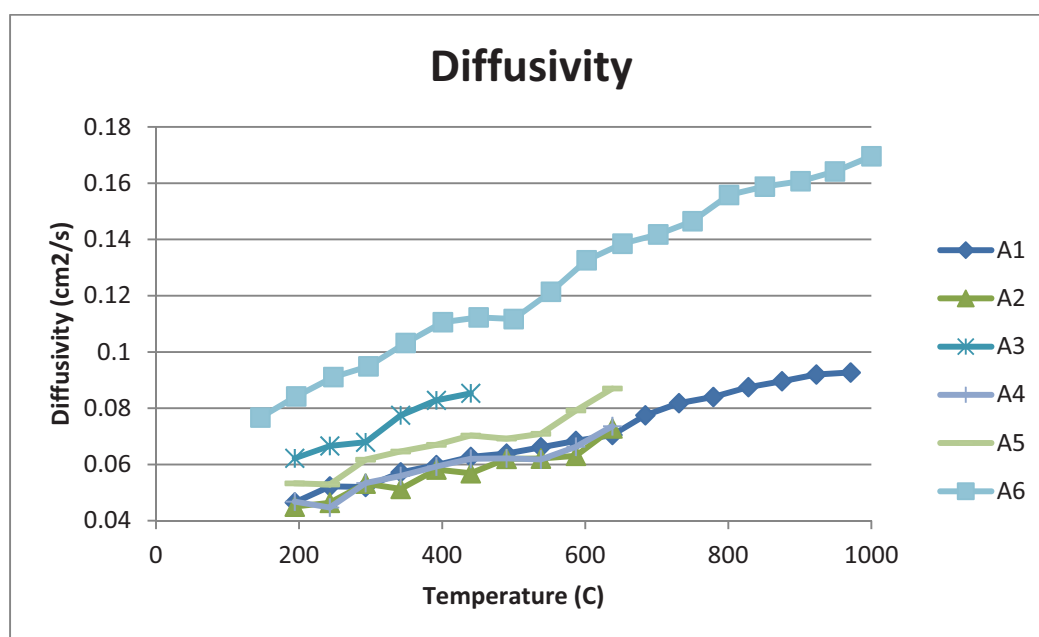


Figure 91. Thermal diffusivity plot for all alloys.

4.4.2 Specific Heat Capacity

The specific heat capacity is measured with the DSC and was not discussed earlier to focus on phase transitions. Here the specific heat capacity values are shown for all six alloys (see Figure 92) (Kennedy 2007, Kennedy 2008).

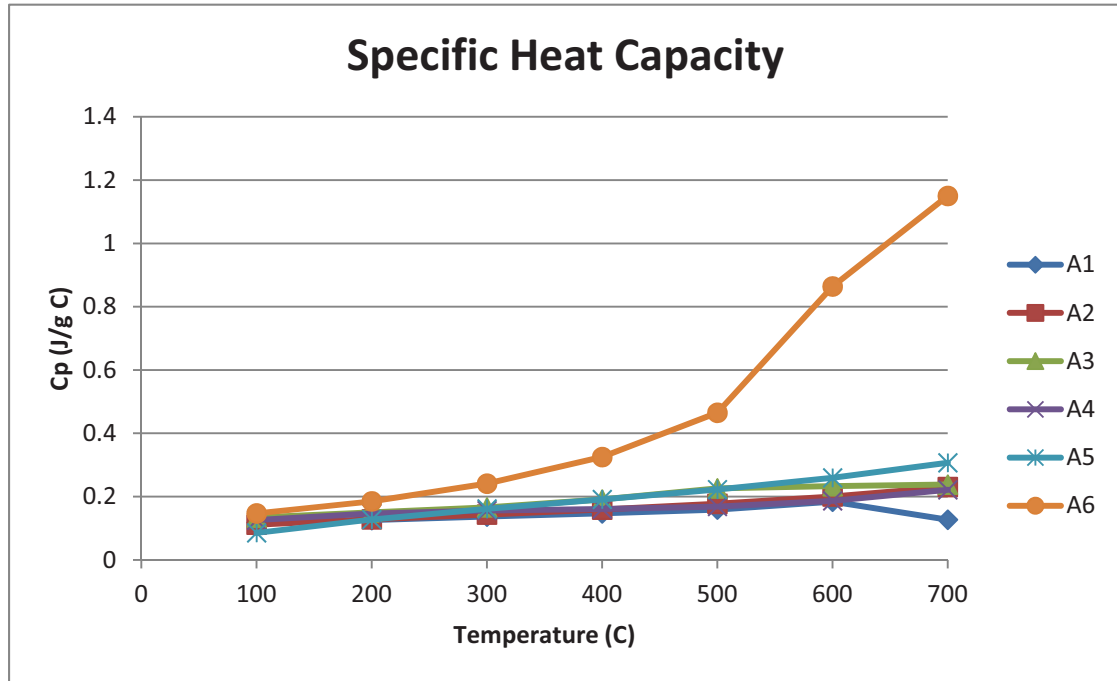


Figure 92. Specific heat capacity plot for all alloys.

4.4.3 Density

Density as a function of temperature is determined using the temperature coefficient of thermal expansion, this property is measured using the TMA. Using Figure 90 as reference, all six alloys have virtually the same linear expansion rate up to 550°C. This expansion can be represented by the following equation.

$$20^{\circ}\text{C}-550^{\circ}\text{C} \quad \% \text{ linear expansion} = 0.0015019T - 0.03003 \quad (3)$$

The density, as a function of temperature, is determined by calculating the volume expansion as a function of temperature and then divide the mass by the new volume. The alloys are expected to behave non-isotropically such that each of the 3 dimensions expands at the rate represented by the above equation. So the volume expansion as a function of the original is represented by the following equation.

$$20^{\circ}\text{C}-550^{\circ}\text{C} \quad \text{Volume expansion} = (1 + (0.000015019T - 0.000303))^3 \quad (4)$$

The density is the room temperature density divided by this equation. The density of the six alloys, up to 550°C, are shown in Table 13.

Table 13. Density as a function of temperature for all alloys.

	A1	A2	A3	A4	A5	A6
Temperature (°C)						
20	14.05	14.13	13.75	13.19	12.86	12.88
50	14.03	14.11	13.73	13.17	12.84	12.86
100	14.00	14.08	13.70	13.14	12.81	12.83
150	13.97	14.05	13.67	13.11	12.78	12.80
200	13.94	14.02	13.64	13.08	12.76	12.78
250	13.91	13.98	13.61	13.05	12.73	12.75
300	13.87	13.95	13.58	13.02	12.70	12.72
350	13.84	13.92	13.55	13.00	12.67	12.69
400	13.81	13.89	13.52	12.97	12.64	12.66
450	13.78	13.86	13.49	12.94	12.61	12.63
500	13.75	13.83	13.46	12.91	12.59	12.61
550	13.72	13.80	13.43	12.88	12.56	12.58

4.4.4 Thermal Conductivity Calculation

Thermal conductivity is determined by multiplying the diffusivity, the specific heat capacity and the density, this is all done as a function of temperature. Tables 14–19 show all four values as a function of temperature for each alloy. Values for properties at temperature that were not measured were extrapolated. In addition, the data presented here is limited to between 100 and 500°C because of data quality issues below and above these temperatures for some of the measured properties.

Table 14. 60U-20Pu-3Am-2Np-15Zr (A1) alloy properties as a function of temperature.

Temperature (°C)	Diffusivity (cm ² /s)	Average Heat Capacity, Cp (J/ g K)	Density (g/cm ³)	Thermal Conductivity (W/cm K)
100	0.0380	0.1180	13.9995	0.0628
200	0.0465	0.1260	13.9367	0.0817
300	0.0520	0.1370	13.8742	0.0988
400	0.0598	0.1470	13.8122	0.1214
500	0.0639	0.1590	13.7505	0.1397

Table 15. 59U-20Pu-3Am-2Np-1RE-15Zr (A2) alloy properties as a function of temperature.

Temperature (°C)	Diffusivity (cm ² /s)	Average Heat Capacity, Cp (J/ g K)	Density (g/cm ³)	Thermal Conductivity (W/cm K)
100	0.0400	0.1113	14.0792	0.0627
200	0.0464	0.1281	14.0100	0.0833
300	0.0513	0.1433	13.9500	0.1026
400	0.0569	0.1591	13.8900	0.1257
500	0.0621	0.1774	13.8300	0.1524

Table 16. 58.5U-20Pu-3Am-2Np-1.5RE-15Zr (A3) alloy properties as a function of temperature.

Temperature (°C)	Diffusivity (cm ² /s)	Average Heat Capacity, Cp (J/ g K)	Density (g/cm ³)	Thermal Conductivity (W/cm K)
100	0.0410	0.1340	13.7000	0.0753
200	0.0520	0.1500	13.6400	0.1064
300	0.0622	0.1660	13.5800	0.1402
400	0.0666	0.1910	13.5200	0.1720
500	0.0680	0.2260	13.4600	0.2069

Table 17. 40.5U-30Pu-5Am-3Np-1.5RE-20Zr (A4) alloy properties as a function of temperature.

Temperature (°C)	Diffusivity (cm ² /s)	Average Heat Capacity, Cp (J/ g K)	Density (g/cm ³)	Thermal Conductivity (W/cm K)
100	0.0395	0.1255	13.1400	0.0651
200	0.0447	0.1465	13.0800	0.0857
300	0.0559	0.1559	13.0200	0.1135
400	0.0620	0.1609	12.9700	0.1294
500	0.0618	0.1687	12.9100	0.1346

Table 18. 41U-30Pu-5Am-3Np-1RE-20Zr (A5) alloy properties as a function of temperature

Temperature (°C)	Diffusivity (cm ² /s)	Average Heat Capacity, Cp (J/ g K)	Density (g/cm ³)	Thermal Conductivity (W/cm K)
100	0.0490	0.0855	12.8100	0.0537
200	0.0529	0.1276	12.7600	0.0861
300	0.0646	0.1612	12.7000	0.1323
400	0.0703	0.1912	12.6400	0.1699
500	0.0709	0.2223	12.5900	0.1984

Table 19. 42U-30Pu-5Am-3Np-20Zr (A6) alloy properties as a function of temperature

Temperature (°C)	Diffusivity (cm ² /s)	Average Heat Capacity, Cp (J/ g K)	Density (g/cm ³)	Thermal Conductivity (W/cm K)
100	0.0670	0.1470	12.8300	0.1264
200	0.0842	0.1850	12.7800	0.1991
300	0.0949	0.2410	12.7200	0.2909
400	0.1106	0.3250	12.6600	0.4551
500	0.1117	0.4650	12.6100	0.6550

In Figure 93, thermal conductivity as a function of temperature is shown for all six alloys. Because of the specific heat values for 42U-30Pu-5Am-3Np-20Zr (A6) being high the thermal conductivity is also high.

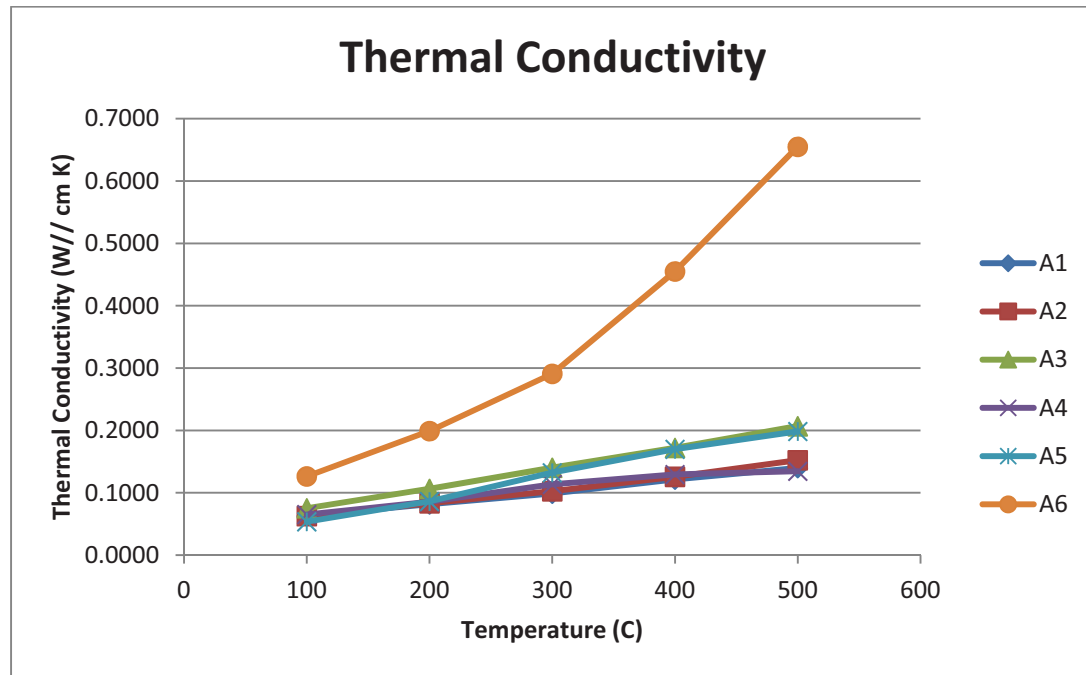


Figure 93. Thermal conductivity curves for all alloys.

5. CONCLUSION

This thesis compiles work I, and others, undertook for several years, laying out the process and documentation needed to fabricate and inspect a nuclear fuel reactor insertion experiment. It also represents the most complete source for unirradiated properties of the AFC-2 experimental fuels. It also reveals some opportunities to improve the experiment design and fabrication process, which are discussed in the following sections.

5.1 Casting Improvements

Arc melting and gravity casting are still in adequate, arc melting is the most rudimentary technique available, it has no temperature control, no real pressure control, and limited hearth material options. The temperature control is the largest short fall, because there is no temperature control we have no way to understand alloy melting temperature or melt super heat. The control of melt super heat allows a control of melt flow times and even solidification rates. I believe excessive superheat was the major contributing factor causing the high Si rind mentioned in earlier sections. A system with more precise temperature control could have still successfully used quartz a mold material without having the high Si rind issue. Because of this belief several casting options were investigated for implementation in a glove box environment.

A centrifugal caster ordered for evaluation as a next-generation research casting process has been set up (see Figure 94) and tested with Ti, Zr and a Cu/Zr alloys (see Figures 95 and 96). In addition, it has been tested with single and multiple slug molds. The caster seems to be effective in all cases and can melt and cast an alloy in less than 2 min. This technology has good promise for future implementation, depending on the length of the fuel needed and other implementation requirements.



Figure 94. Centrifugal caster.



Figure 95. Single large diameter casting in quartz mold.



Figure 96. Multiple AFC-2 representative diameter casting of titanium.

The centrifugal casting system was used to produce an Sm sample for characterization and also to produce a HfAl_2 sample for another nuclear technology program.

Another research scale casting system was considered; the commercial system appears to have good production scalability. These systems were developed for the jewelry industry and have two separate chambers: one chamber for the crucible and melting, and one chamber for the mold. In general, the atmospheres of these two chambers are independent and can be used to push molten material from the crucible side into the mold side. Some of these off-the-shelf systems are capable of casting 15 in. pins. Procurement of one of these systems was initiated, and is now available to cast uranium and non radioactive metals. Figure 97 illustrates the stand-alone vacuum casting system.



Figure 97. Stand-alone vacuum casting system.

Figure 98 shows the two-chamber concept of this system.

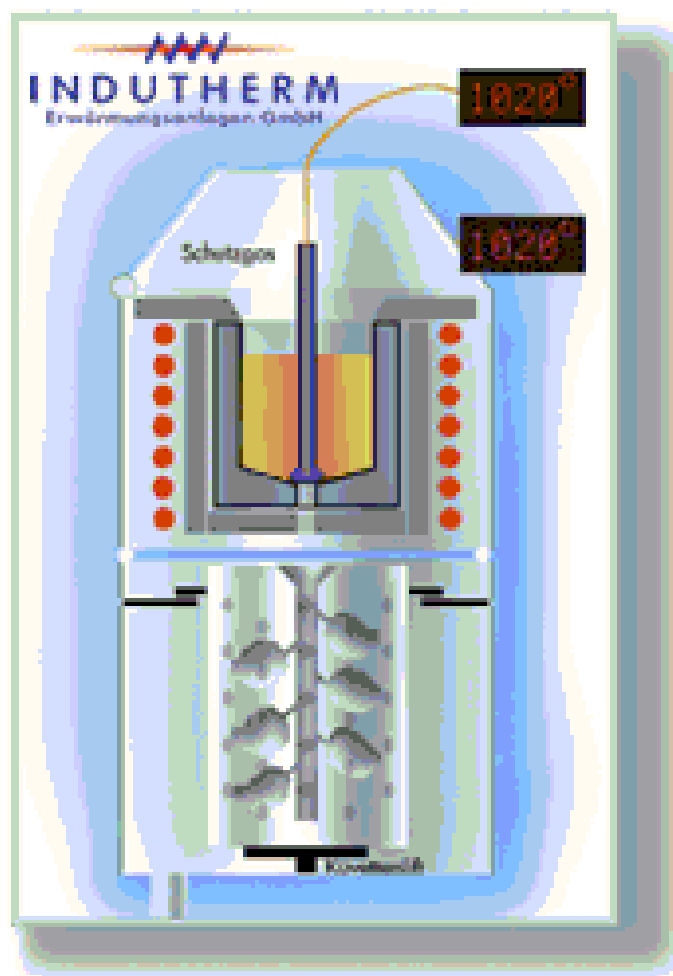


Figure 98. Section view of the two-chamber casting concept.

In the end it was decided that the commercially available casting systems were just not quite right for direct glove box implementation. A casting system was designed, built and tested for glove box installation. This system called the Bench scale Casting System (BCS) was first tested in a fume hood using Uranium and Uranium alloys. (Fielding 2008). With some minor design changes, as a result of initial testing, the system was adapted and named the Glove box Advanced Casting System (GACS). The new system is mostly installed in a Transuranic glove box and will be used for future fuel castings with TRU elements. Another advantage to this design is that it should eliminate the volatilization of Am during the melting process.

5.2 Experiment Design Improvements

The capsule design that contains 6 rodlets is flawed. The cladding failure of any given rodlet will lead to the entire experiment being invalid because the fission gas from the breached rodlet will contaminate the He in the capsule. This change in gas mixture will cause the heat conduction out of each rodlet to change. The heat conduction will actually be dropping which will cause the temperature in the individual rodlets to rise above the targeted irradiation temperature. In fact this occurred in the AFC-3A capsule. The failure of the A3 rodlet was discovered during the initial Neutron radiography of the capsule during its scheduled Post Irradiation Examination (Chichester 2011). In addition, the long length and tight tolerances of the capsule tubes made their fabrication difficult and expensive. Each capsule tube costs over \$5,000, just for the raw tube purchase. Another fabrication challenge is the building up of nubs on the ends and in the middle of the tube. These nubs, located every 90 degrees around the tube, are built up using a wire feed welding process and are then machined back to the desired diameter. The nubs, then act to center the capsule in the basket. The basket is the final component of the entire experiment to be inserted into the reactor. The problem with this process is that the heat from welding causes the tube to bend out of tolerance due to thermal expansion differences from one side of the tube to the other. As a result, after welding the tubes need to be re straightened.

After the discovery of the breached rodlet and the fabrication challenges the design of AFC experiments was changed to address each of these problems. The capsule was shorted so that each capsule contained one rodlet and the nubs were replaced by fins machined directly into the capsule end caps. The first experiments with these design changes were AFC-3A and 3B. The design of this experiment is documented in “Fabrication Report for the FY 11 Phases of the AFC-3A and 3B Irradiation Experiments” (Fielding et. al. 2011).

6. REFERENCES

- Bhadeshia, H. K. D. H, "Differential Scanning Calorimetry," University of Cambridge, Materials Science & Metallurgy, date unknown.
- Broeders, C. H. M., E. Kiefhaber, H. W. Wiese, "Burning Transuranium Isotopes in Thermal and Fast Reactors," *Nuclear Engineering and Design*, 202, 2000, pp. 157-172.
- Burkes, D. E, J. R. Kennedy, T. Hartmann, L. N. Squires, "Phase Characteristics of U-22 Pu-4Am-2Np-40Zr Metallic Alloy Containing Rare Earths," *Journal of Phase Equilibria and Diffusion*, Volume 30, April 2009.
- Burkes, D. E., J. R. Kennedy, T. A. Hyde, L. N. Squires, C. A. Papesch, A. P. Maddison, "Thermal Conductivity of U-20Pu-3Am-2Np-15Zr Metallic Alloys Containing Rare Earths," *Journal of Nuclear Materials*, July 2010.
- Burkes, D. E., J. R. Kennedy, T. Hartmann, C. A. Papesch, D. D. Keiser Jr., "Phase Characteristics of a Number of U-Pu-Am-Np-Zr Metallic Alloys for Use as Fast Reactor Fuels," *Journal of Nuclear Materials*, 396, 2010, 49-56.
- Chichester, H. J. M., D.L. Porter, B. A. Hilton, "Postirradiation Examination of AFC-1D, 1G, 1H, and 2A Experiments," Idaho National Laboratory Report INL/LTD-11-23242, September 2011.
- Crawford, D. C., C. E. Lahm, H. Tsai, R. G. Pahl, "Performance of U-Pu-Zr Fuel Cast into Zirconium Molds," *Journal of Nuclear Materials*, 204, 1993, pp. 157-164.
- Edsinger, R. E., J. L. Reilly, and J. F. Schodey, "Thermal Expansion of Platinum and Platinum-Rhodium Alloys," *Journal of Research of the National Bureau of Standard*, Vol. 91, Number 6, December 1986.
- Fielding, R., K. Marsden, B. Grover, G. Preslar, "Advanced Bench-Scale Metal Fuel Casting System Development," *Transactions of the American Nuclear Society*, v 99, pg 305-306, 2008.
- Fielding, R., P. Hansen, T.A. Hyde, J. Maupin, "Fabrication Report for the FY11 Phases of the AFC-3A and 3B Irradiation Experiments," Idaho National Laboratory Report, INL/LTD-11-23158, September 2011.

- Harbur, D. R., J. W. Anderson, W. J. Maraman, "Studies on the U-Pu-Zr Alloy System for Fast Breeder Reactor Applications," Las Alamos Scientific Laboratory Internal Document #LA-4512, August 1970.
- Hayes, S. L., "Irradiation of Metallic Fuels with Rare Earth Additions for Actinide Transmutation in the ATR," INL/EXT-06-11707, Rev. 2, December 2006.
- Hayes, S. L., "Irradiation of Nitride and Metallic Fuels for Actinide Transmutation in the Advanced Test Reactor: Final Experiment Description and Design and Data Package for AFC-1A, AFC-1B, AFC-1C and AFC-1D," Argonne National Laboratory (West), Document No. W7520-0481-ES-02, February 2003.
- Hayes, S. L., D. J. Utterbeck, "Project Description, Advanced Fuel Cycle Initiative, AFC-2A and AFC-2B Experiments," INL/EXT-07-12388, March 2007.
- Hecker, S. S., M. Stan, "Plutonium Metallic Fuels for Fast Reactors," *Journal of Nuclear Materials*, 2007.
- Hilton, B. A., "Irradiation of Nitride and Metallic Fuels for Actinide Transmutation in the Advanced Test Reactor: Final Experiment Description and Design and Data Package for ACF-1E, and AFC-1F," Argonne National Laboratory (West) Document No. W7520-0529-ES-03, November 2003.
- Hilton, B. A., "Irradiation of Nitride and Metallic Fuels for Actinide Transmutation in the Advanced Test Reactor: Final Experiment Description and Design and Data Package for ACF-1G, and AFC-1H," Argonne National Laboratory (West) Document No. W7520-0678-ES-00, August 2004.
- Hilton, B. A., D. L. Porter and S. L. Hayes, "AFC-1 Transmutation Fuels Post Irradiation Hot Cell Examination 4 to 8% Preliminary Report: Irradiation Experiments AFC-1B, AFC-1F and AFC-1E," Idaho National Laboratory Report, INL/EXT-05-00785, September 2005.
- Hofman, G. L., L. C. Walters, T. H. Bauer, "Metallic Fast Reactor Fuels," *Progress in Nuclear Energy*, Vol. 31, No. 1-2, 1997, pp. 83-110.
- Hyde, T. A., "AFC-2 Fuel Rodlet and Capsule Final Inspection Plan," PLN-2443, Idaho National Laboratory, January 2008.
- Hyde, T. A., "Specification for the AFC-2A and AFC-2B Fuel Specimen and Fuel Capsule Irradiation Experiment in the ATR," TFR-452, Idaho National Laboratory, April 2007.

- Inoue, T., "Actinide Recycling by Pyro-Process with Metal Fuel FBR for Future Nuclear Fuel Cycle System," *Progress in Nuclear Energy*, Vol. 40, No. 3-4, 2002, pp. 547-554.
- Janney, D. E., J. R. Kennedy, "As-Cast Microstructures in U-Pu-Zr Alloy Fuel Pins with 5-8 Wt.% Minor Actinides and 1-1.5 Wt% Rare-Earth Elements," *Mater Charact*, 2010.
- Keiser, Jr., D. D., "Fuel-Cladding Interaction Layers in Irradiated U-Zr and U-Pu-Zr Fuel Elements," Argonne National Laboratory Report, NT Technical Memorandum No. 240, 1996.
- Keiser, Jr., D. D., M. C. Petri, "Interdiffusion Behavior in U-Pu-Zr Fuel Versus Stainless Steel Couples," *Journal of Nuclear Materials*, 240, 1996 pp. 51-61.
- Kennedy, et al., "AFC2-A,B Metal Fuel Characterization FY 2008 Supplemental Report," INL/EXT-08-14499, August 2008.
- Kennedy, J. R., A. Maddison, D. Burkes, C. Papesch, "Thermal Analysis of AFC-2A Metallic Transmutation Fuels FY 2007 Report," Idaho National Laboratory Report EXT-07-13128, September 2007.
- Kennedy, J. R., D. D. Keiser, S. M. Frank, M. K. Meyer, "The Microstructure and Phase Characterization of Non-Fertile AFC-1 Transmutation Metallic Test Fuels," Argonne National Laboratory, NT Technical Memorandum No. 219, May 2003.
- Kennedy, J. R., D. E. Janney, "The Phase and Microstructure Characterization of AFC-2A Metallic Transmutation Fuels: FY 2007 Report," Idaho National Laboratory Report EXT-07-13027, August 2007.
- Kennedy, J. R., D. Janney, D. Burkes, T. Hartmann, A. Maddison, C. Papesch, "AFC2-A, B Metal Fuel Characterization FY2008 Supplemental Report," Idaho National Laboratory Report EXT-08-14499, August 2008.
- Kim, Y. S., G. L. Hofman, S. L. Hayes, Y. H. Sohn, "Constituent Redistribution in U-Pu-Zr Fuel During Irradiation," *Journal of Nuclear Materials*, 327, 2004, pp. 27-36.
- Kim, Y. S., G. L. Hofman, S. L. Hayes, Y. H. Sohn, "Constituent Redistribution of U-Pu-Zr Fuel During Irradiation," *Journal of Nuclear Materials*, 327, 2004, pp. 27-36.
- Kim, Y. S., S. L. Hayes, G. L. Hofman, A. M. Yacout, "Modeling of Constituent Redistribution in U-Pu-Zr Metallic Fuel," *Journal of Nuclear Materials*, 359, 2006, pp. 17-28.

- Kruger, O. L., "Phase Relations and Structures in Uranium-Plutonium-Fissium Alloys," *Journal of Nuclear Materials*, 19, 1966, pp. 29-41.
- Kurata, M., K. Nakamura, T. Ogata, "Thermodynamic Evaluation of the Quaternary U-Pu-Zr-Fe System – Assessment of Cladding Temperature Limits of Metallic Fuel in a Fast Reactor," *Journal of Nuclear Materials*, 294, 2001, pp. 123-129.
- Kurata, M., T. Inoue, C. Sari, "Redistribution Behavior of Various Constituents of U-Pu-Zr Alloy and U-Pu-Zr Alloy Containing Minor Actinides and Rare Earths in a Temperature Gradient," *Journal of Nuclear Materials*, Vol. 208, 1994, pp. 144-158.
- Lahm, C. E., J. F. Koenig, R. G. Pahl, D. L. Porter, D. C. Crawford, "Experience with Advanced Driver Fuels in EBR-II," *Journal of Nuclear Materials*, 204, 1993, pp. 119-123.
- Leibowitz, L., E. Veleckis, R. A. Blomquist, "Solidus and Liquidus Temperatures in the Uranium-Plutonium-Zirconium System," *Journal of Nuclear Materials*, 154, 1988, pp. 145-153.
- Leibowitz, L., R. A. Blomquist, A. D. Pelton, "Thermodynamics of the Uranium-Zirconium System," *Journal of Nuclear Materials*, 167, 1989, pp. 76-81.
- Mardon, P. G., J. H. Pearce, J. A. C. Marples, "Constitution Studies on the Neptunium-Plutonium Alloy System," *Journal of the Less-Common Metals*, 3, 1961, pp. 381-292.
- Marples, J. A. C., "The Plutonium-Zirconium Phase Diagram," *Journal of the Less-Common Metals*, 1960.
- Mueller, M. H., J. W. Richardson, Jr., R. V. Strain, G. L. Hofman, "Phase Analysis of Metallic Plutonium Containing Fuel Alloys Using Neutron Diffraction," Conference Document 9007149-5, December 1991.
- Nakamura, K., T. Ogata, M. Kurata, "Analysis of Metal Fuel/Cladding Metallurgical Interaction During Off-Normal Transient Events with Phase Diagram of the U-Pu-Zr-Fe System," *Journal of Physics and Chemistry of Solids*, 66, 2005, pp. 643-646.
- O'Boyle, D. R., A. E. Dwight, "Proceedings, International Conference in Pu and Other Actinides," Santa Fe, NM, Session 2, 1970, p. 720.
- Ogawa, T., "Transmutation of Minor Actinides and Innovative Fuel Cycle Concepts," *Progress in Nuclear Energy*, Volume 40, No. 3-4, 2002, pp. 539-546.

- Pahl, R. G., D. L. Porter, D. C. Crawford, L. C. Walters, "Irradiation Behavior of Metallic Fast Reactor Fuels," *Journal of Nuclear Materials* 188, 1992, pp. 3-9.
- Report to Congress on the Advanced Fuel Cycle Initiative: The Future Path for Advanced Spent Fuel Treatment and Transmutation Research, US Department of Energy Office of Nuclear Science and Technology, January 2003.
- Sari, C., C. T. Walker, M. Kurata, T. Inoue, "Interaction of U-Pu-Zr Alloys Containing Minor Actinides and Rare Earths with Stainless Steel," *Journal of Nuclear Materials*, 208, 1994, pp. 201-210.
- Sohn, Y. H., M. A. Dayananda, G. L. Hofman, R. V. Strain, S. L. Hayes, "Analysis of Constituent Redistribution in the γ (bcc) U-Pu-Zr Alloys under Gradients of Temperature and Concentrations," *Journal of Nuclear Materials*, 279, 2000, pp. 317-329.
- Trybus, C. L., J. E. Sanecki and S. P. Henslee, "Casting of Metallic Fuel Containing Minor Actinide Additions," *Journal of Nuclear Materials*, 204, 1993, pp. 50-55.
- Walters, L. C., "Thirty Years of Fuels and Materials Information from EBR-II," *Journal of Nuclear Materials*, 270, 1999, pp. 39-48.
- Ward, J. W., "Systematic Properties of Actinide Metals," *Journal of Less-Common Metals*, 121, 1986, pp. 1-13.